FLORIDA INTERNATIONAL UNIVERSITY

Miami, Florida

LANTHANIDE INTERACTIONS WITH LIGANDS AND BIOMOLECULES:

SPECTROSCOPIC AND EXTRACTION STUDIES

A dissertation submitted in partial fulfillment of

the requirements for the degree of

DOCTOR OF PHILOSOPHY

in

CHEMISTRY

by

Setareh Sakhdari

2021

To: Dean Michael R. Heithaus
        College of Arts, Sciences, and Education

This dissertation, written by Setareh Sakhdari and entitled Lanthanide Interactions with Ligands and Biomolecules: Spectroscopic and Extraction Studies, having been approved in respect to style and intellectual content, is referred to you for judgment.

We have read this dissertation and recommend that it be approved.

_____
Jaroslava Miksovska

_____
Raphael G. Raptis

_____
Prem P. Chapagain

_____
Francisco A. Fernandez-Lima

_____
Konstantinos Kavallieratos, Major Professor

Date of Defense: June 24, 2021

The dissertation of Setareh Sakhdari is approved.

_____
Dean Michael R. Heithaus
College of Arts, Sciences and Education

_____
Andrés G. Gil
Vice President of Research and Economic Development
and Dean of the University Graduate School

Florida International University, 2021

ACKNOWLEDGMENTS

ABSTRACT OF THE DISSERTATION

LANTHANIDE INTERACTIONS WITH LIGANDS AND BIOMOLECULES:

SPECTROSCOPIC AND EXTRACTION STUDIES

by

Setareh Sakhdari

Florida International University, 2021

Miami, Florida

Professor Konstantinos Kavallieratos, Major Professor

Lanthanides (Ln), also known as rare earth metals, have been utilized for industrial and biological purposes and are commonly encountered in the 3+ oxidation state as Ln^{3+}. The presence of Ln in spent nuclear fuel introduces problems during the transmutation and partitioning of actinides (An) due to the Ln high neutron cross-sections. Therefore, designing ligands for Ln^{3+} complexation, can be helpful for their separation from An^{3+} in nuclear technology. Also, the biomimetic roles of Ln^{3+} could be suitable for studying the biological macromolecules, such as the Ca^{2+}-binding EF-hand proteins that are otherwise inaccessible for detailed structural analysis. In this study, we report a bis(quinoline)-dipicolinamide ligand ($DQPDH_2$), as well as ortho- nitrobenzyl cage ligands (DM-nitrophen and H_2-cage) that bind and/or separate Ln^{3+}. We studied DREAM, a Ca^{2+} EF-hand protein, to analyze its interaction with Ln^{3+}.

UV- Vis absorption and fluorescence spectroscopy, circular dichroism, extraction, isothermal titration calorimetry (ITC) and photophysical spectroscopy were used for studying the interaction of Ln^{3+} and ligands/proteins. Our results indicate that $DQPDH_2$ showed high binding affinity to Ln^{3+} with 1-1 complexation ratio, as confirmed by spectroscopic and solvent extraction studies. The X-ray crystal structure of the Nd^{3+}-$DQPDH_2$ complex indicated a 1-1 binding pattern, which is consistent with our spectroscopic studies. DM-nitrophen, showed high binding affinity to Ln^{3+} by absorption spectroscopy and ITC. Photoacoustic calorimetry has been performed on DM-nitrophen and Tb^{3+}DM-nitrophen photodissociation and the resulting kinetic and thermodynamic data indicated successful release of Tb^{3+} upon photocleavage of DM-nitrophen. H_2-cage showed modest binding affinity with Ln^{3+} by UV-Vis absorption spectroscopy, yet it was also shown to be an effective Ln^{3+} extractant. Fluorescence spectroscopy studies of Ca^{2+} binding proteins with Ln^{3+} showed efficient energy transfer from the protein to central Ln^{3+} and possible conformational changes upon Ln^{3+} binding to protein by observing a decrease in tryptophan emission and an increase in emission of hydrophobic probe and DREAM complex.

In summary, our results demonstrated that dipicolinamide-derived ligands can be used for complexation and separation of Ln^{3+}. Furthermore, *o*-nitrobenzyl cages and Ln^{3+}DREAM interaction studies can be used as probes for studying the function of Ca^{2+}-binding EF-hand proteins in future.

TABLE OF CONTENTS

CHAPTER   PAGE

LIST OF TABLES

LIST OF FIGURES

ABBREVIATIONS AND ACRONYMS

1,8-ANS	1-Anilinonaphthalene-8-sulfonic acid
DM-nitrophen	1-(2-Nitro-4,5-dimethoxyphenyl)-1,2-Diaminoethane-N,N,N',N'- Tetraacetic acid
Cyclen	1,4,7,10-tetraazacyclododecane
DNBS	2,4-dinitrobenzenesulfonyl
HEPES	2-[4-(2-hydroxyethyl) piperazine-1-yl] ethane sulfonic acid
BTP	2,6-bis (1,2,4-triazin-3-yl)-pyridine
SO_3-ph-BTP	2,6-bis (5,6-di(sulfophenyl)-1,2,4-triazin-3-yl) pyridine
CyMe4-BTP	2,6-bis (5,5,,8,8-tetramethyl-5,6,7,8-tetrahydrobenzo [1,2,4] triazine-3-yl) pyridine
DOTA	2,2',2'',2'''-(1,4,7,10-Tetraazacyclododecane-1,4,7,10--tetrayl) Tetraacetic acid
MOPS	3-(morpholino) propane sulfonic acid
BTBP	6,6'-bis(1,2,4-triazin-3-yl)-2,2'-bipyridine
CH_3CN	Acetonitrile
CD	Circular dichroism
CH_2Cl_2	Dichloromethane
Et_2O	Diethylether
DTPA	Diethylenetriamine pentaacetate

DMBA	Dimethylbenzylamine
DQPDH$_2$	N^2,N^6-di(quinoline-8-yl) pyridine-2,6-dicarboxamide
DREAM	Downstream Regulatory Antagonist Modulator
DR	Dynamic range
EDTA	Ethylenediaminetetraacetic acid
EGTA	(Ethylene glycol-bis (β-aminoethylether)-N,N,N',N'-tetraacetic acid
FRET	Förster resonance energy transfer
ITC	Isothermal titration calorimetry
LOD	Limit of detection
LLLs	Luminescent lanthanide labels
MRI	Magnetic resonance imaging
NCS	Neuronal calcium sensor
NMR	Nuclear magnetic resonance
OLED	Organic light-emitting diode
PAC	Photoacoustic calorimetry
Phe	Phenylalanine
H$_2$cage	Pyridine2-carboxylic acid {1-(2-nitro-phenyl)-2-[(pyridine-2-ylmethyl)-carbamoyl]-ethyl}-amide
QD	Quantum dots

TALSPEAK	Trivalent Actinide Lanthanide Separation with Phosphorous-Reagent Extraction from Aqueous Komplexes
TODGA	N,N,N',N'-tetraoctyl diglycolamide
TRIS	Tris (hydroxymethyl) aminomethane
Trp	Tryptophan
Tyr	Tyrosine
UV-Vis	Ultraviolet-visible

Chapter 1

Introduction: Ln^{3+} complexation and caging

1.1. Ln^{3+} caging and its biological importance

Lanthanides (Ln), commonly found in the 3+ oxidation state as Ln^{3+}, have multitude of applications in biological studies, such as analysis of properties of biomacromolecules including proteins and DNA.[1-3] The spectroscopic and magnetic properties of Ln^{3+} make them suitable as substitutes for studying the Ca^{2+}- and Mg^{2+}-binding proteins. Ln^{3+} have been employed as Ca^{2+} biomimetics due to their ability to mimic functional properties of Ca^{2+} in biological systems and have been used to study the function of Ca^{2+}-binding EF-hand proteins such as calmodulin, calbindin and the downstream regulatory element antagonist modulator, DREAM.[4,5] It has been shown that calmodulin (CaM) has higher affinity for Ln^{3+} over Ca^{2+} and that conformational changes in Ln^{3+}-bound CaM are not significantly different from those in Ca^{2+}-bound CaM.[3] Ln^{3+} binding also inhibits the function of cadherin-mediated cell adhesion by replacing Ca^{2+} in Ca^{2+}-binding sites.[6] DREAM, is a member of neuronal calcium sensor family that has been implicated in Alzheimer's disease. This multifunctional protein interacts with numerous intracellular targets, such as calmodulin, DNA and Ca^{2+}-related drugs. It has been shown that DREAM binds Tb^{3+} with an affinity that is superior to that for Ca^{2+}, and Ln^{3+} association to DREAM triggers conformational changes that are analogous to those induced by Ca^{2+}.[5] Ln^{3+} binding to DREAM facilitates fluorescence emission and NMR studies which allow insight to mechanisms of signal transduction and biological activity of this protein.[5] Niedźwiecka et al. (2012) employed modified peptides containing polyaminocarboxylates to coordinate Tb^{3+}. Their complex incorporates a tryptophan residue for sensitization of Tb^{3+} complex to investigate various protein structures, functions, and dynamics.[1] (Fig. 1.1).
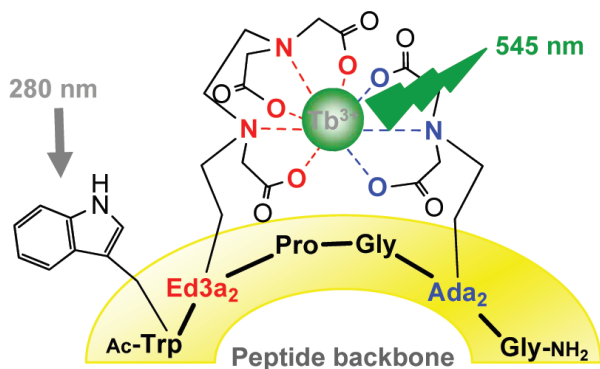
Figure 1.1. A Ln^{3+}-binding peptide incorporating non-natural chelating amino acids[1]

1.2. Ln^{3+} as sensing agents

Ln^{3+} cations have been widely used for sensing, particularly in biological studies.[7-9] Luminescent lanthanide labels (LLLs) have been used as acceptors in studies employing Förster resonance energy transfer (FRET).[7] In FRET, there is a distance-dependent energy transfer between an excited state of a donor fluorophore and a ground state of an acceptor fluorophore, a characteristic that is suitable in biosensing applications. Geißler et al. (2014) have used combinations of LLLs and quantum dots (QDs) for immunoassays and cellular imaging.[7] This field provides opportunities for reduced autofluorescence background by time-gating of long-lived LLL luminescence, which is valuable for cell and tissue imaging (Fig. 1.2).[7]
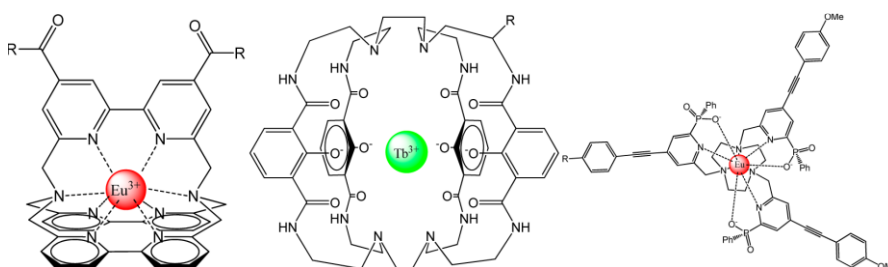
Figure 1.2. Examples of luminescent lanthanide labels (LLL)[7]

MRI studies or NIR optical detection of neurotransmitters using Gd^{3+}, Yb^{3+}, and Nd^{3+} complexes have been reported by Oukhatar et al. (2019). The authors used a macrocyclic ligand consisting of benzophenone chromophore and a monoazacrown ether.[8] Cellular delivery of Ln^{3+} lumiphores for live-cell imaging has been reported using Ln^{3+}-carrying peptides.[9]

1.3. Ln^{3+} complexes

As Ln^{3+} can be used as An^{3+} surrogates[10] and have biomimetic functions,[5] several ligands have been designed to complex Ln^{3+}.[11-15] Ln^{3+} can be used as sensors due to the delayed luminescence of Ln^{3+} cations arising from 4f-4f electronic transitions. These emissions are interesting because of the presence of long-lived excited states (from μs to ms), long emission wavelengths spanning the visible and NIR ranges, and line-like emission bands (10-30 nm bandwidth) under ambient conditions. As the direct excitation of Ln^{3+} is forbidden due to 4f-4f electron transitions, coordinating ligands have been designed for efficient sensitization of Ln^{3+}.[11] Among the Ln^{3+} series, Eu^{3+} and Tb^{3+} emit strongly in the visible range (500-700 nm), making them suitable for developing luminescence sensors using chromophoric units (also known as "antennas"), that are typically incorporated into these complexes. For efficient sensitized emission, the triplet energy state of the ligand should be in certain distance with the excited energy levels of Ln^{3+}.[11-13] Figure 1.3 depicts an example of a ligand acting as a cyclen-based chromophore, transferring energy to central Ln^{3+}.[12]
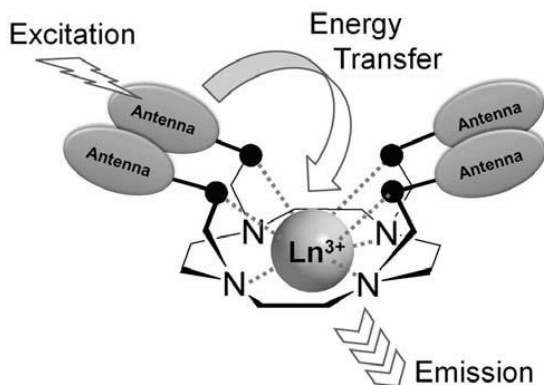
Figure 1.3. A cyclen-based Ln^{3+} complex and its mechanism of luminescence[11]

1.3.1. Carboxylate-based Ln^{3+} complexes

Ln^{3+} are highly oxophilic hard Lewis acids preferring complexation to hard donors, such as oxygen. Carboxylate-rich ligands are suitable for binding to Ln^{3+} as they increase the solubility and stability of Ln^{3+} complexes due to the chelate effect.[14,15] Among carboxylate-rich ligands, aliphatic carboxylic acids may not be applicable for sensitization, due to their lack of conjugated π bonds, as Ln^{3+} require an efficient sensitizer to become luminescent. On the other hand, aromatic carboxylate-rich ligands are efficient sensitizers, as the aromatic moiety of the ligand can transfer energy to the central Ln^{3+}.[14,15] Hernandez-Fuentes et al. (2020) have employed benzoic acid/benzoate as ligand to complex Eu^{3+}. The aromatic ring in this structure forms a conjugated bond when binding to Eu^{3+}, resulting in efficient energy transfer to Eu^{3+} (Fig. 1.4).[16] Comparison of the IR spectra of the ligand and the two complexes showed a red-shift in the stretch band of COO^- indicating binding to Ln^{3+}. Other carboxylate-based Ln^{3+} complexes have been reported that were used for polymer studies.[15]
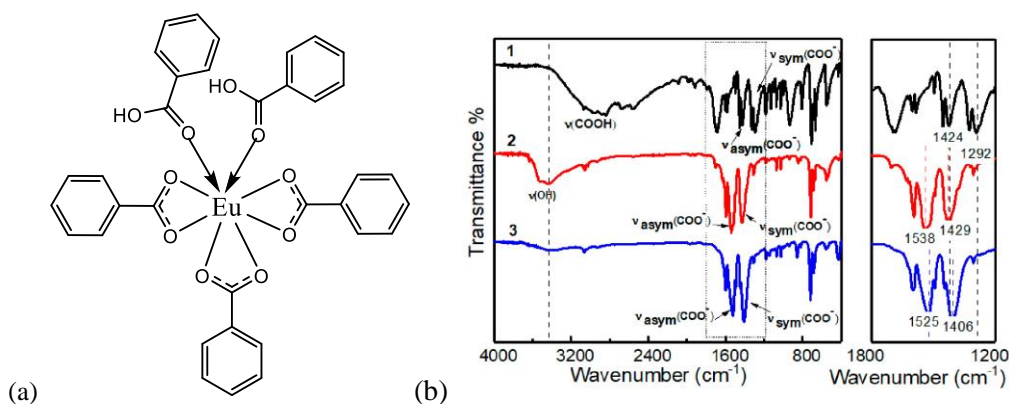
Figure 1.4. (a) Corresponding Ln^{3+} complex of benzoic acid-based ligand. (b) FT-IR spectra of: benzoic acid (1); $[Eu(OOCC_6H_5)_3.(H_2O)_3]$ (2); $[Eu(OOCC_6H_5)_3.(HOOCC_6H_5)_2]$ (3)[16]

Dai et al. (2013) have reported a carboxylate-based ligand containing a pyridine groups for detection of biothiols in biological media. The 2,4-dinitrobenzenesulfonyl moiety (DNBS) of the ligand is separated upon reacting with biothiols, leading to change in the fluorescence of the Eu^{3+} or Tb^{3+} complexes (Fig. 1.5).[17]
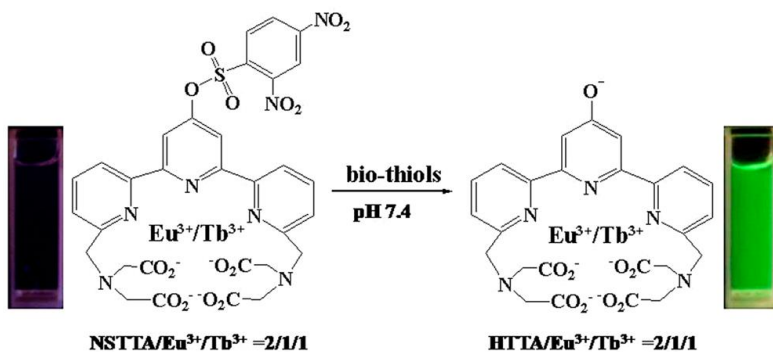
Figure 1.5. Fluorescence detection of biothiols: The NSTTA/Eu^{3+} and Tb^{3+} complexes convert to HTTA/Eu^{3+}/Tb^{3+} complexes.[17]

Hanaoke et al. (2004) have demonstrated Zn^{2+} detection by carboxylate-rich Ln^{3+} complexes incorporating a quinoline-containing ethylenediamine ligand that binds to Ln^{3+}

(Fig. 1.6). Zn^{2+} is detected by the increase in luminescence, as well as a change in the absorption spectra.[18]
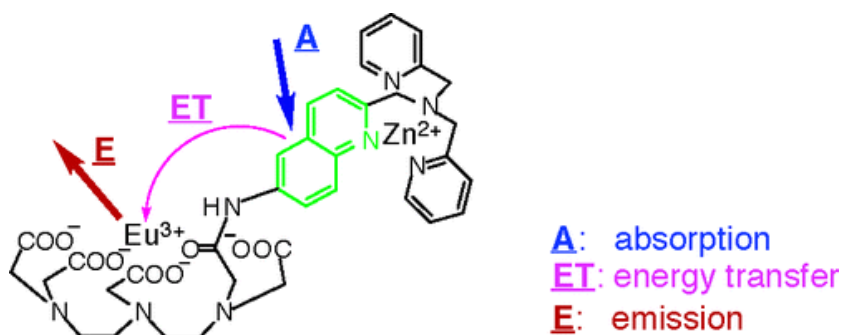
Figure 1.6. Eu^{3+} complex for Zn^{2+} detection. The presence of Zn^{2+} causes the nitrogen-containing aromatic ligands to arrange in a way that energy is transferred from quinoline moiety to Eu^{3+}-bound ligand resulting in enhanced emission of Eu^{3+}.[18]

1.3.2. Ln^{3+} complexes with mixed oxygen and nitrogen containing ligands

The presence of nitrogen in Ln^{3+} complexes with aromatic ligands helps for sensitization of the Ln^{3+} in addition to its chelating function, as both nitrogen and oxygen can coordinate to central Ln^{3+}.[15] A prominent mixed oxygen- and nitrogen- containing ligand for Ln^{3+} complexation is 2,2′,2″,2‴-(1,4,7,10-Tetraazacyclododecane-1,4,7,10-tetrayl)tetraacetic acid (DOTA), which consists of a cyclen framework with additional carboxylate arms attached to the nitrogen atoms. Examples of DOTA-based Ln^{3+} complexes are the Gd^{3+} complexes which are used for the development of contrast agents for MRI,[19] and Eu^{3+}/Tb^{3+} complexes used for detection of anions, such as fluoride.[20-22] As Ln^{3+} are hard Lewis acids, they form bonds with a large electrostatic component.

Surender et al. (2016) have reported a Eu^{3+}-cyclen complex as pH sensor, where the phenanthroline moiety acts as a sensitizer for Eu^{3+} (Fig. 1.7).[22]

(a)   (b)
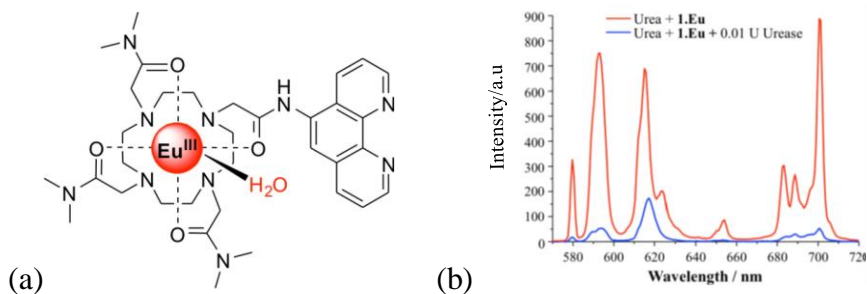
Figure 1.7. (a) Structural formula of Eu^{3+}-cyclen complex as pH sensor. (b) The emission spectra of Eu^{3+} complex in the presence of urea and urease.[22]

Que et al. (2006) have reported a DOTA-based Gd^{3+} complex that incorporates aromatic dianionic carboxylate arms for Cu^{2+} detection. As the carboxylate groups bind to Cu^{2+}, water becomes available for the central Gd^{3+} metal, leading to quenching of Gd^{3+} emission (Fig. 1.8).[19]
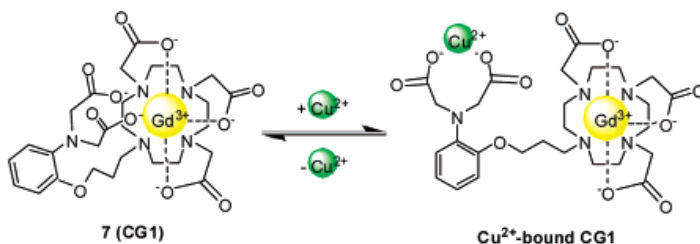
Figure 1.8. Complex of Copper-Gad-1(CG1) in the presence and absence of Cu^{2+}.[19]

Tb^{3+}-DOTA complexes have also been used for detection of enzymes and other species through pH measurements. Specifically, a benzoate moiety binding to central Tb^{3+} when it is in its deprotonated form indicates basic pH (Fig. 1.9).[12] The presence of an enzyme like glycosidase has been detected when the enzyme cleaves the bond between the sugar and

7

the phenolic-based antenna leading to an increase in the Tb^{3+} emission (Fig. 1.10).[23] The presence of various anions, such as acetate and phosphate as environmental pollutants in agricultural areas, has been detected with DOTA-based Tb^{3+} complexes using diaryl-urea moiety (Fig. 1.11).[20]
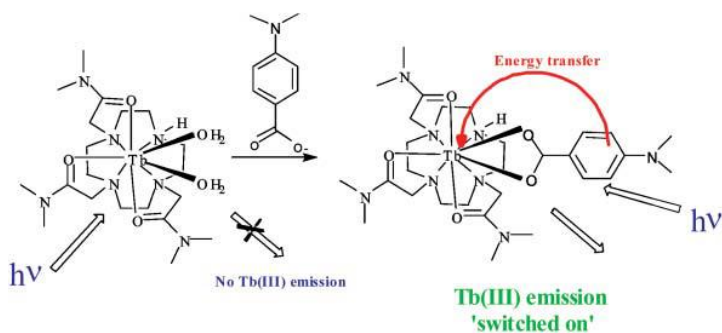
Figure 1.9. Detecting benzoate with a Tb^{3+}-DOTA complex.[20]
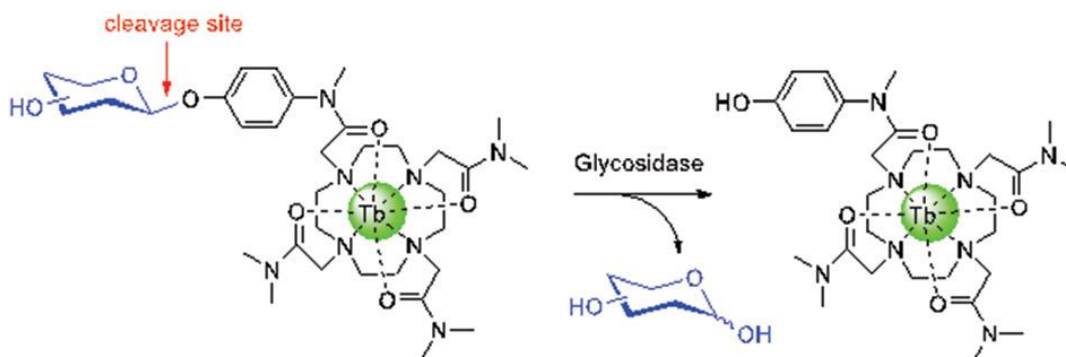
Figure 1.10. Left: The structure of the glycosylated Tb^{3+} cyclen complex. Right: The resulting cyclen complex bearing the phenol-based antenna, which is formed upon enzymatic hydrolysis of the glycosidic bond.[23]

(a)   (b)
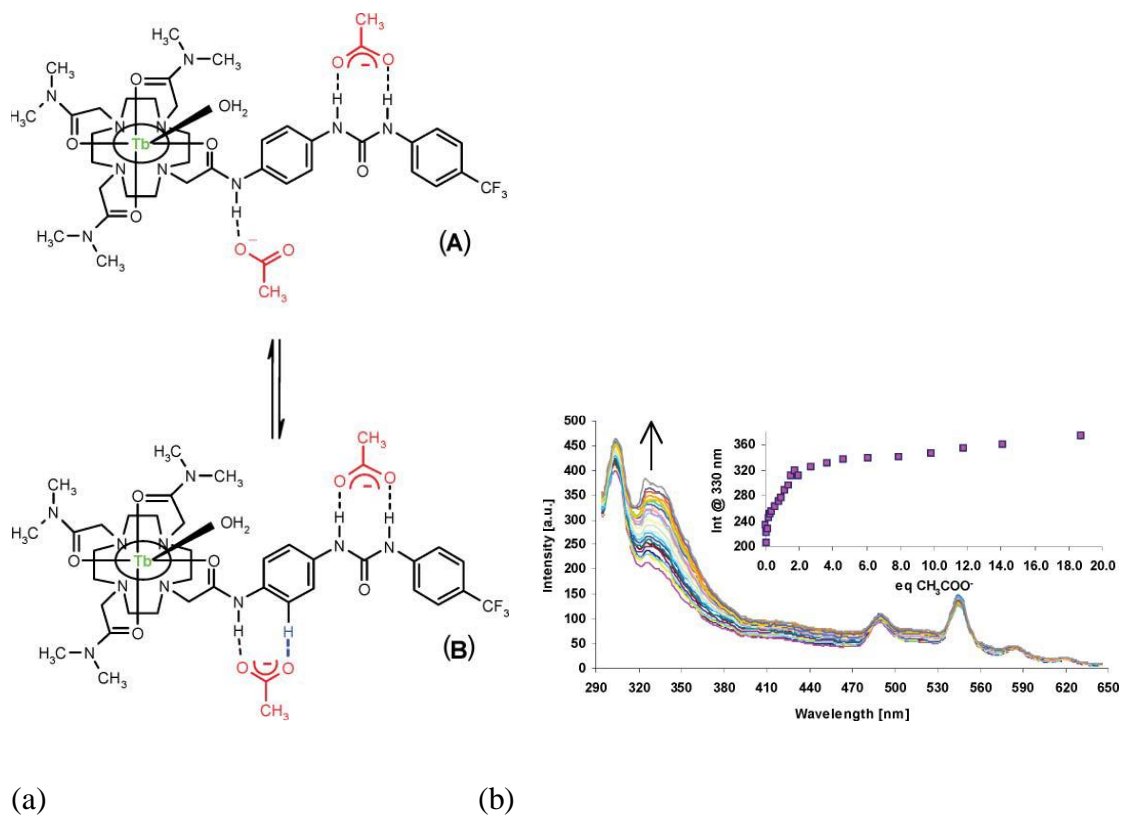
Figure 1.11. (a) Proposed hydrogen bonding interaction between the Tb[3+]-cyclen diaryl-urea complex and CH$_3$COO[-]. (b) Changes in fluorescence emission intensity of Tb[3+] complex upon addition of CH$_3$COO[-].[20]

Sahoo et al. (2020) employed an aminomethylpiperidine functionalized 1,10-phenanthroline-based nitrogen-rich hexadentate heterocyclic ligand for making luminescent Eu^{3+} and Tb[3+] complexes. Their luminescence change in the presence of various anions makes them applicable for anion detection in biological systems.[24]

Hirayama et al. (2009) have reported a Tb[3+]-cyclen-di(2-picolyl) amine complex as a tag for generating fluorescent proteins for Zn^{2+} sensing, in which Zn^{2+} interacts with the oligoaspartate residue. Excitation of tryptophan in the presence of Tb[3+] results in energy transfer from tryptophan to Tb[3+], leading to increase in the fluorescence (Fig. 1.12).[25] A DOTA-based Gd^{3+} complex has also been reported for Zn^{2+} detection.[26]
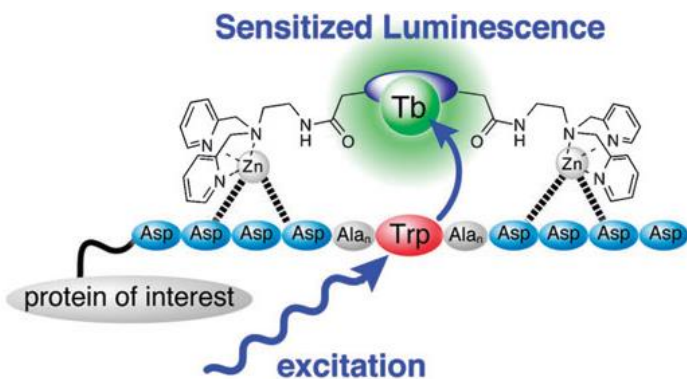
Figure 1.12. Sensitized Tb^{3+}-luminescence in a Tb^{3+}-Zn^{2+} peptide.[25]

1.3.3. Ln^{3+} complexes with amide ligands

As Ln^{3+} prefer high coordination numbers, tripodal amide ligands can provide a high coordination environment for Ln^{3+}. A ligand of this type was designed by Aroussi et al. and resulted to a supramolecular cage with high flexibility and organization. In this supramolecular cage the absorption spectroscopy measurements upon ligand titration with Eu^{3+} show a red-shift, as it would be expected by Eu^{3+} complexation due to n→π* and π→π* transitions of the pyridinedicarbonyl units (Fig. 1.13).[27]
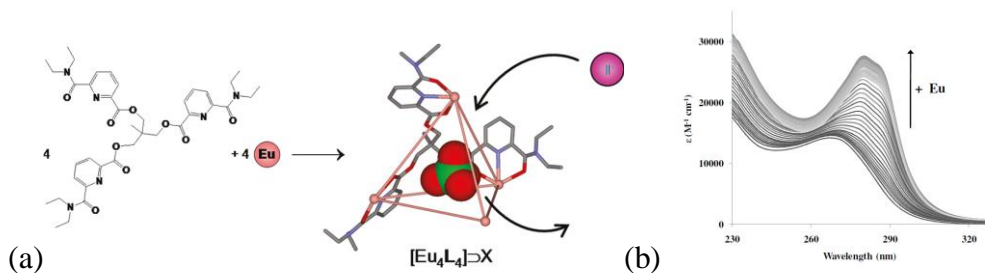
Figure 1.13. (a) Supramolecular assembly formed by reaction of a tripodal ligand with Eu^{3+}. (b) UV-Vis titration of the tripodal ligand with Eu^{3+}.[27]

Petoud et al. (2003) reported a 2-hydroxyisophthalamide-derivative ligand for complexation of Eu^{3+}, Tb^{3+}, Sm^{3+} and Dy^{3+}. Figure 1.14 shows the ligand in addition to the emission of its corresponding Ln^{3+} complex. [28]

(a)

(b)

(c)
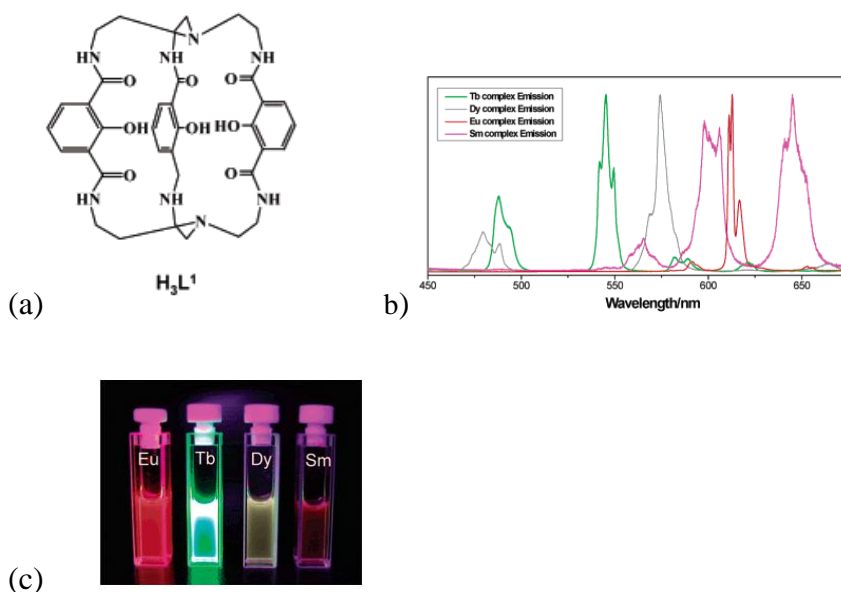
Figure 1.14. (a) Ligand structure containing 2-hydroxyisophthalamide moiety. (b) The emission spectra of each Ln^{3+} complex with two molecules of H_3L^1. (c) Picture of the emission of aqueous solutions of $[Ln(H_2L^1)_2]^+$ [28]

Quinoline-based ligands can form luminescent Ln^{3+} complexes that can also be used in optical devices. Shavaleev et al. (2008) synthesized a benzothiazole-substituted 8-hydroxyquinoline ligand for Ln^{3+} for applications in biochemical analysis and optical telecommunication devices (Fig. 1.15).[29]
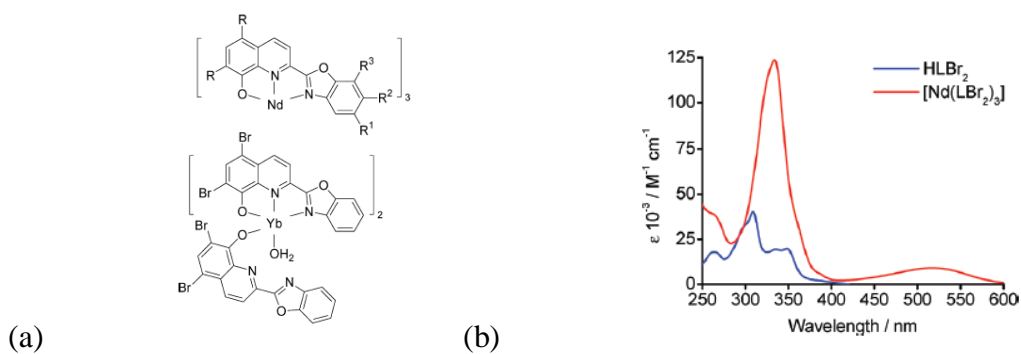
Figure 1.15. (a) Structure of Ln^{3+} complexes. (b) Absorption spectra of the ligand and its Nd^{3+} complex.[29]

Xu et al. (2019) have reported phenanthroline-based phosphonate ligands for separation of An^{3+} and Ln^{3+}. Specifically, they reported that the Am-N bond has higher covalent character and is shorter than the Eu-N bond while the Am-O bond is longer than the Eu-O bond, indicating that Eu^{3+} has higher affinity to oxygen than Am^{3+} and that the phenanthroline moiety enhances Am^{3+} extraction. The absorption spectra of the Am^{3+} and Eu^{3+} complexes are red-shifted compared to the free ligand (Fig. 1.16).[30]
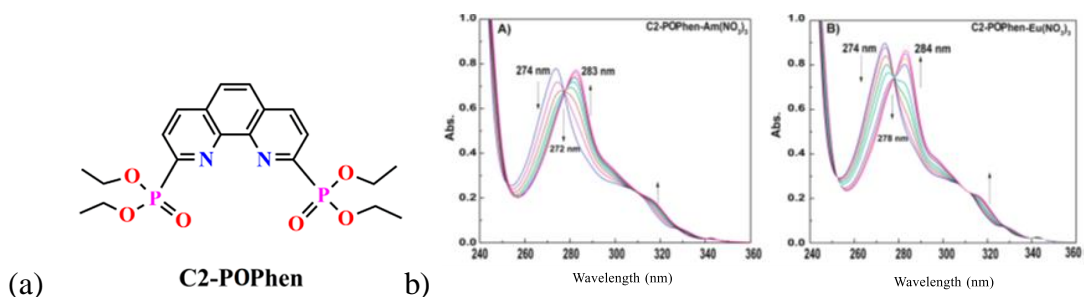
Figure 1.16. (a) The tetraethyl(1,10-phenanthroline-2,9-diyl)phosphonate (C2-POPhen). (b) Spectroscopic titrations of C2-POPhen with $Am(NO_3)_3$ and $Eu(NO_3)_3$.[30]

Paulenova et al. (2008) have also shown separation of Ln^{3+} and An^{3+} with dipicolinamide ligands (ditolyldiamides) by varying the concentration of HNO_3. Figure 1.17 shows the

structures of these dipicolinamide ligands.[31] They were also able to plot the distribution

ratio (D) for extraction of each Ln^{3+} for the three ligands as the function of ionic radius of

Ln^{3+}.

(a)

(b)
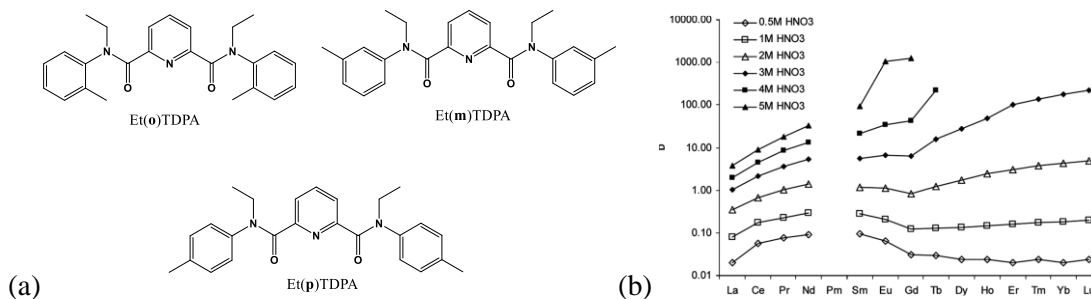
Figure 1.17. (a) Structures of diamide derivatives of dipicolinic acid. (b) Extraction of Ln^{3+} from nitric acid. Solvent: 0.2 M Et(**o**)TDPA in fluorinated diluent phenyltrifluoromethylsulfone (FS-13)[31]

Nitrogen-containing heterocyclic ligands for An^{3+}/Ln^{3+} separation have been reported by

Geist et al. (2012) and Gorden et al. (2013) (Fig. 1.18).[32,33] Geist et al. (2012) showed that

by adding sulfonated groups to the bis-triazinyl pyridine frameworks (SO₃-Ph-BTP), the

resulting hydrophilic ligands can selectively hold back An^{3+} in the aqueous phase, while

Ln^{3+} are extracted in the organic phase containing the organic extractant N,N,N′,N′-

Tetraoctyldiglycolamide (TODGA).
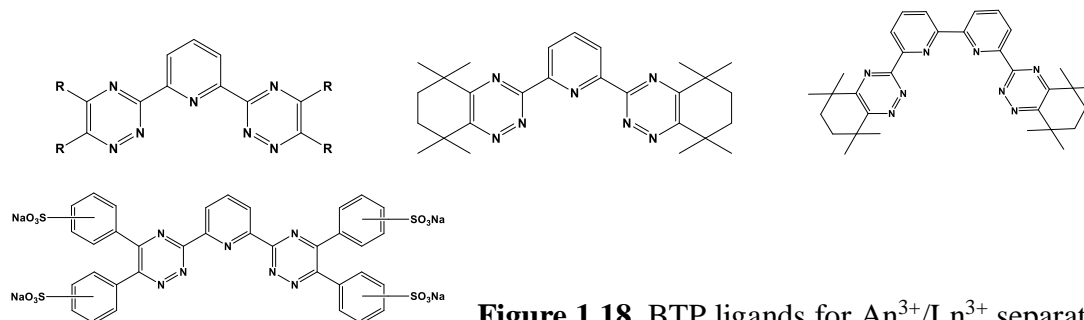
Figure 1.18. BTP ligands for An^{3+}/Ln^{3+} separation.[32]

Lehman-Andino et al. (2019) synthesized dipicolinamide and dithiopicolinamide ligands for Ln^{3+} and An^{3+} complexation. Figure 1.19 shows the structure of the Nd^{3+} complex of a dipicolinamide ligand, and its UV-Vis spectral changes upon titration with Nd^{3+}, indicating a red-shift with an absorption increase at 300 nm.[10]

(a)   (b)
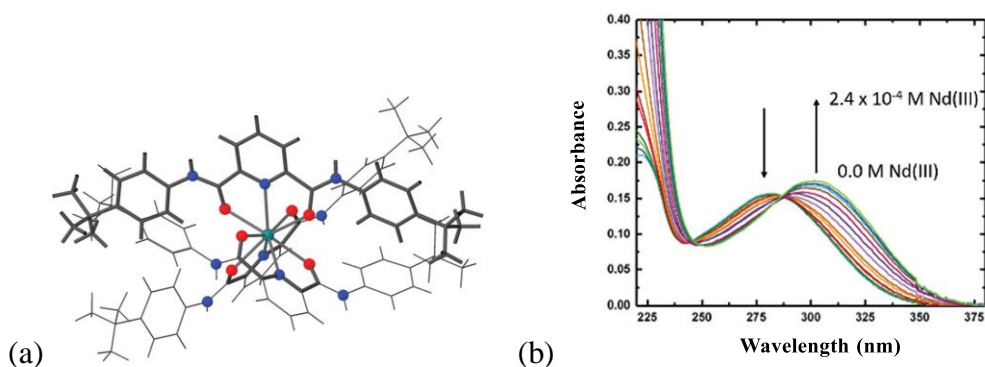
Figure 1.19. (a) Structure of N^2,N^6-bis(4-(tert-butyl)phenyl)-pyridine-2,6-dicarboxamide complex with Nd^{3+} (b) UV-Visible spectra for titration of the same ligand with $Nd(NO_3)_3.6H_2O$.[10]

1.4. Ln^{3+} interactions with EF-hand proteins

Previous studies have indicated high affinity of EF-hand proteins, such as calmodulin $(CaM)^3$ and DREAM, to Ln^{3+}.[5] Drobot et al. (2019) demonstrated high binding affinity of CaM with Eu^{3+} by monitoring the increase in Eu^{3+} emission because of energy transfer from tyrosine to Eu^{3+} (Fig. 1.20). Gonzalez et al. (2016) also showed that Tb^{3+} binding to CaM and DREAM results in an increase of Tb^{3+} emission. It was also confirmed that increasing the concentration of Tb^{3+} quenches the tryptophan emission in DREAM (Fig. 1.21).[5]

(a)   (b)
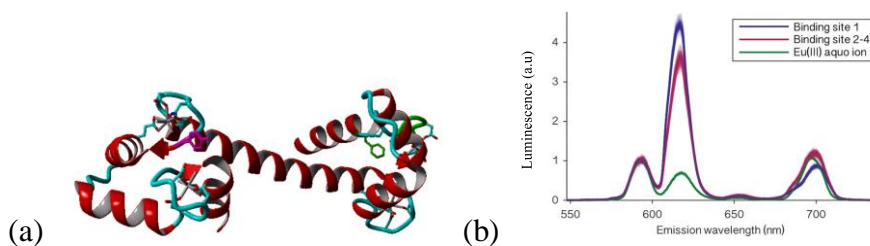
Figure 1.20. (a) Structure of CaM. (b) Emission spectra of Eu^{3+} interaction with CaM.[3]
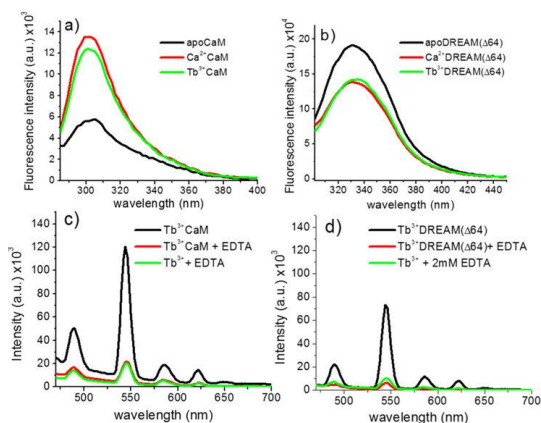
Figure 1.21. (a) Addition of Ca^{2+} and Tb^{3+} to CaM. (b) Addition of Ca^{2+} and Tb^{3+} to DREAM ($\Delta64$) (excited at 280 ± 4 nm). (c) Addition of CaM to Tb^{3+}. (d) Addition of DREAM to Tb^{3+}. Tb^{3+}EDTA complex is shown as the reference.[5]

1.5. Photolabile cage compounds

The term "Cage compound" typically refers to molecules which bind and trap different species and release them upon an illumination. The trapped species vary in size and the photo-release of the caged molecule can occur on different timescales, ranging from nanosecond to milliseconds. The advantage of using cages is that they can be used as photolabile probes to study intracellular pathways. In addition, the extent of photolysis of these molecules can be controlled by varying the light intensity and the area of the light spot. Ortho-nitrobenzyl cages are a family of compounds that are commonly used for

15

binding and releasing of ions, such as Ca^{2+} and Mg^{2+}, as well as larger molecules, such as adenosine triphosphate and glutamate. Some examples of *o*-nitrobenzyl cages that are used for Ca^{2+} caging are DM-nitrophen, nitr-5 and nitrophenyl-EGTA. (Fig. 1.22). [35]
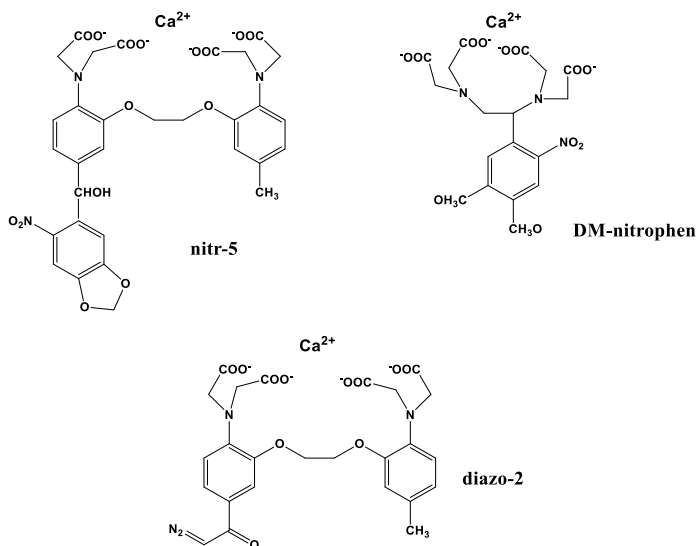
Figure 1.22. Structures of Ca^{2+} cages (nitr-5 and DM-nitrophen) and a photoactivatable Ca^{2+} scavenger (diazo-2).[35]

These cages typically absorb light between 320-360 nm with different quantum yields and may bear additional functional groups, such as phosphates, carboxylates, hydroxyl groups, amines, and amides.[34] The strong binding of Ca^{2+} to Ca^{2+} cages is evident from the dissociation constants. For example, K_d for Ca^{2+} binding to unphotolysed DM-nitrophen is 5 nM, to photolyzed nitr-5 is 145 nM, and to EGTA is 80 nM.[36] The photolysis pathway for nitrobenzyl compounds is shown in Figure 1.23.[37]
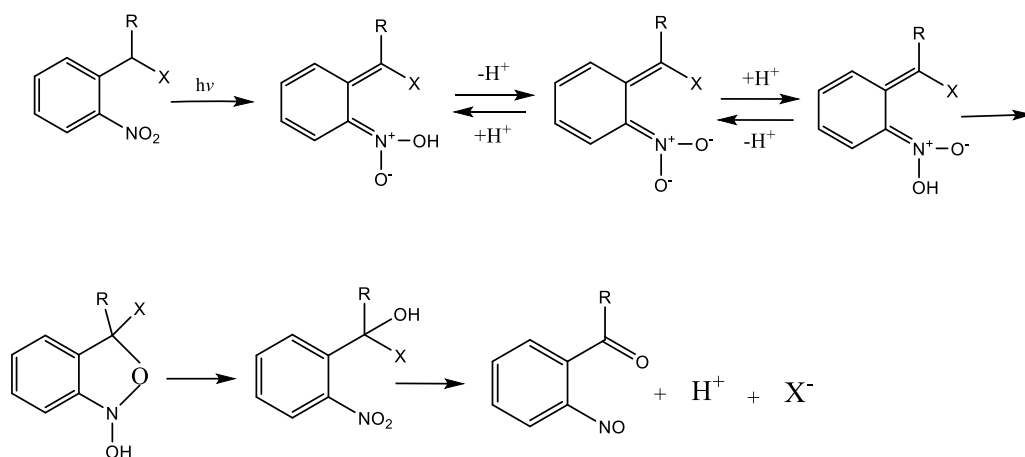
Figure 1.23. The proposed photolysis of *o*-nitrobenzyl cage.[37]

The decay rate of *aci*-nitro intermediate that is produced after the intramolecular rearrangement of bonds, highly depends on the size of the caged species, and varies from nanoseconds to milliseconds. It was proposed that the *aci*-nitro intermediate decay is the rate-determining step for the caged molecule release.[37]

The overall scheme for the photolysis of Ca^{2+}DM-nitrophen and the absorption spectra are shown in Figure 1.24. Addition of Ca^{2+} causes a decrease in the absorption of DM-nitrophen, which could be the result of conformational differences in Ca^{2+}DM-nitrophen complex from the unbound DM-nitrophen.[38]
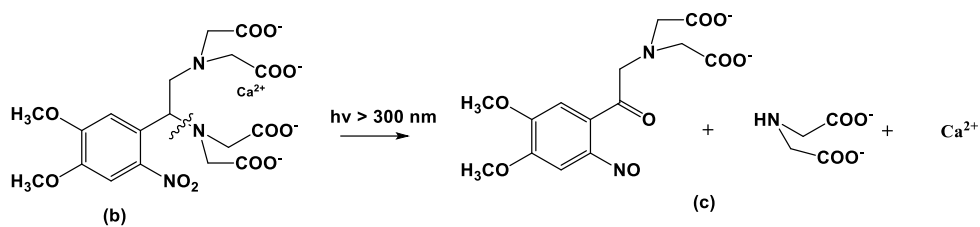
(I)
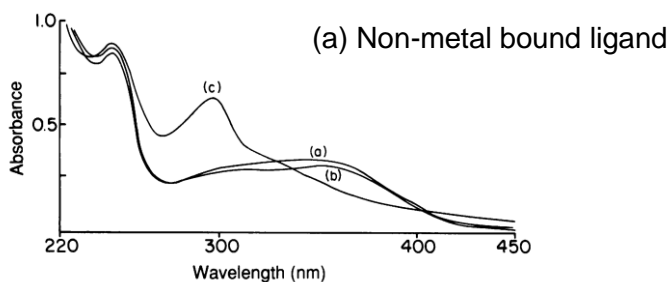
(II)

Figure 1.24. (I) The photolysis of Ca^{2+}DM-nitrophen. (II) (a) The absorption spectra of DM-nitrophen; (b) The absorption of DM-nitrophen after addition of $CaCl_2$; (c) The absorption of DM-nitrophen after it has been photolyzed for 60s.[38]

H_2cage is another ortho-nitrobenzyl cage that has been previously used for caging Cu^{2+}.

Figure 1.25 shows the structure of H_2cage, Cu^{2+} complexation, and the photolysis of Cu^{2+}-cage.[39]
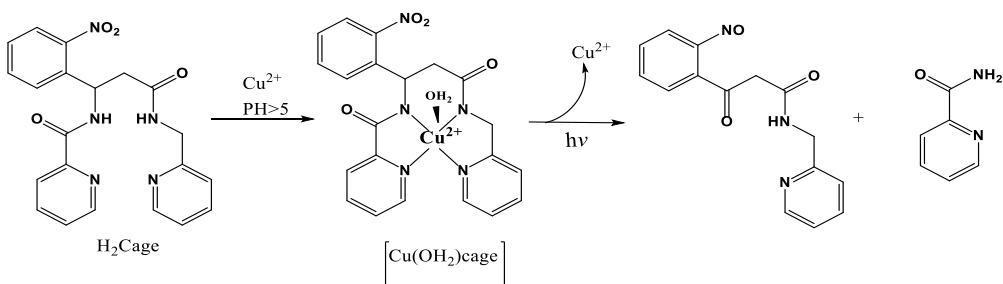
Figure 1.25. The structure of H_2cage, its Cu^{2+} complex, and Cu^{2+} release upon photon trigger.[39]

18

1.6. Isothermal titration calorimetry

Isothermal titration calorimetry (ITC) is a quantitative analytical method for studying binding interactions and providing information about enthalpy, entropy, free energy, and binding constants. For a reversible biomolecular reaction,

$$S + L \leftrightharpoons S.L$$
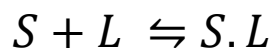
the thermodynamic parameters for substrate (S) binding to the ligand (L), forming the substrate- ligand complex (S.L) can be expressed using Eq. 1 and Eq. 2.

The Gibbs free energy (ΔG) under equilibrium conditions can be calculated using standard Gibbs free energy ($\Delta G°$) and the concentration of reactants and products according to Eq. 1.

$$\Delta G = \Delta G° + RT\ln \left[\frac{[L.S]}{[L][S]} \right] \qquad \text{Eq. 1}$$

Under equilibrium conditions, $\Delta G = 0$; therefore:

$$\Delta G° = -RT\ln \left[\frac{[L.S]}{[L][S]} \right] = -RT\ln K_a = RT\ln K_d \qquad \text{Eq. 2}$$

R → Perfect gas constant

T →Absolute temperature

K_a → Equilibrium association constant

K_d → Equilibrium dissociation constant

1.6.1. ITC instrumentation set-up

ITC consists of two cells: reference and sample. The reference cell is filled with the buffer while the sample cell is filled with ligand that is titrated with the substrate. The instrument works using a heat compensation system which applies power (microcalories per second) to balance the temperature difference between the reference and sample cells.[40] Each peak

appearing on the ITC system represents the heat after each injection of substrate. As more ligand binding sites get saturated, there will be less heat absorbed or released, making the subsequent peaks smaller in size. The heat resulting from the injection of the substrate comes from the binding interaction between the substrate and the ligand. Exothermic reactions lead to a decreased applied power while the endothermic reactions cause an increased feedback. (Fig. 1.26). From ITC peaks, a titration curve is obtained from which the dissociation constant K_d and stoichiometry can be determined using non-linear regression analysis.

The K_d range in an ITC experiment is typically between 10 nM and 1 μM ($K_a \sim 10^8$ to 10^9 M^{-1}) while the enthalpy range is between -20 to +5 kcal/mol. Enthalpy represents the strength of the interaction between the ligand and the substrate while the entropy represents conformational changes due to ligand:substrate interactions in solution.[41] In most cases, the interaction between the ligand and the substrate is entropically driven with either favorable or unfavorable enthalpy changes. The improved reliability, sensitivity and accuracy of ITC instrumentation can have a prominent role in molecular and drug design.[41]
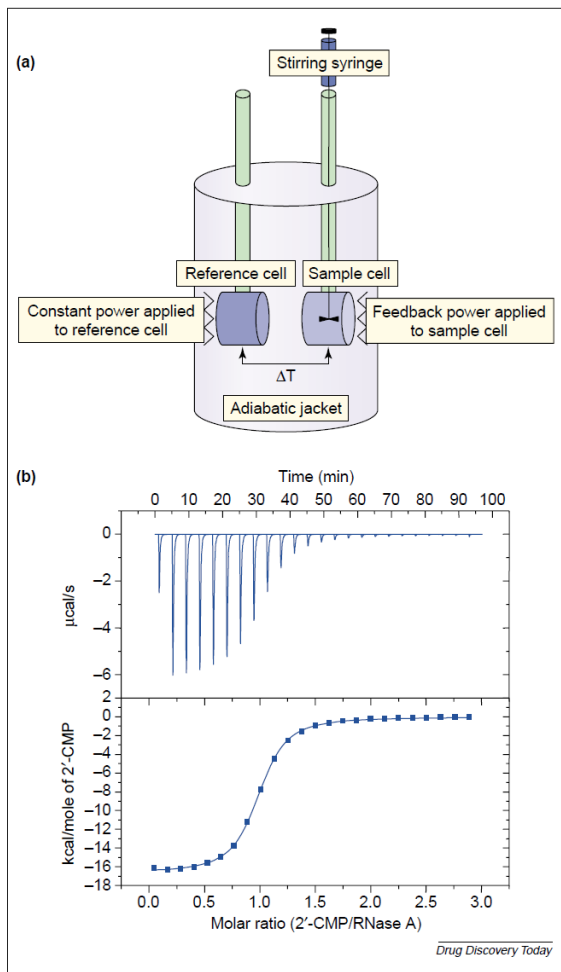
Figure 1.26. (a) A cartoon picture of ITC instrumentation setup. Constant power is applied to the reference cell with variable power to the sample cell leading to a small temperature difference between two cells. Exothermic reactions cause a decrease while the endothermic reactions cause an increase in the feedback power. (b) Example of an ITC experimental data. Top panel shows the power applied to the sample cell by the instrument to minimize the temperature difference between the two cells. Bottom panel shows the integrated peak areas as a function of molar ratio of substrate and ligand. Fitting experimental data integrated to give a fit from an appropriate model provides reaction thermodynamic parameters such as ΔH, ΔS, K_d, and stoichiometry.[40]

1.6.2. Use of displacement method for thermodynamic calculations by ITC

The displacement method in ITC is used when the substrate has such a high affinity for the ligand that a titration curve cannot be obtained (Fig. 1.27). To overcome this problem, a competition experiment is designed where a high-affinity substrate is titrated to the ligand

which is already bound to another substrate with weaker affinity. This experiment is defined as a displacement experiment.[41]
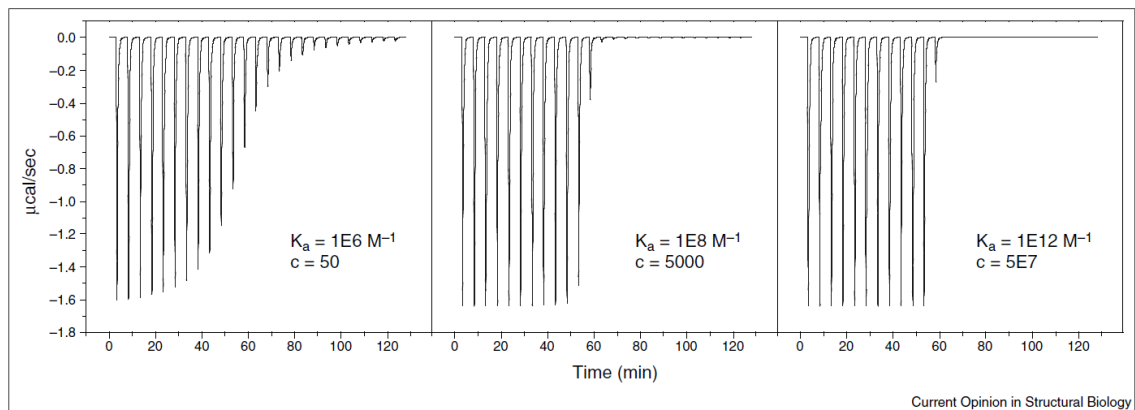
Figure 1.27. Illustration of the effect of increasing binding affinity on the ability of ITC to measure the binding constant. The ITC experiments were simulated using the binding affinity and the quantity $c = K_a[\text{protein}]$ are shown in the panels. For c values less than 1000, the affinity constant and enthalpy change can be readily determined. For c > 1000, only the binding enthalpy can be measured and only a lower limit for binding affinity is obtained.[41]

1.7. Optical spectroscopy

Optical spectroscopy techniques study interactions of a material with electromagnetic radiation to determine the structural and physical properties of matter. In optical spectroscopy, matter typically absorbs electromagnetic radiation that promotes a molecule to a higher energy configuration defined as the excited state. From the excited state, the molecule returns to ground state by releasing energy as either radiation (radiative decay) or heat (nonradiative decay). Additional processes, such as quenching and energy transfer may also be involved in the de-excitation. Two types of optical spectroscopy are discussed here: Absorption and emission (fluorescence) spectroscopy.[43]

1.7.1. Absorption spectroscopy

In absorption spectroscopy, the molecule absorbs light which converts it from ground state (S_0) to excited state (S_1). The energy of the absorbed light overcomes the electrostatic attraction between the electrons and the nuclei (Fig. 1.28).
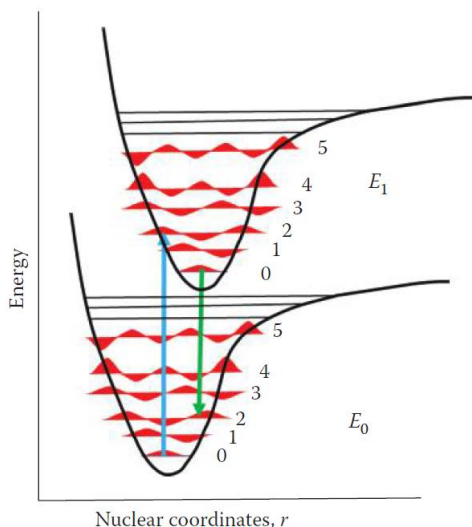
Figure 1.28. Morse diagram illustrating two electronic energy levels (*E*0 and *E*1), and some associated vibrational levels (0–5), as a function of interatomic distance. Absorption (blue) and emission (green) transitions are also depicted.[44]

Biological chromophores typically contain aromatic groups, such as proteins that contain tryptophan and tryrosine which show absorption in UV range (~280 nm) due to π-π* transitions. In addition, the absorbance of the peptide bond at 220 nm is due to n-π* electronic transition.

1.7.2. Fluorescence spectroscopy

Fluorescence is the emission of light from a substance that returns from its excited state to its ground state. The fluorescence lifetime is the average time between excitation and the return to ground state. Fluorophores containing planar, aromatic molecules typically show sub-nanosecond lifetimes.[43] The emission properties of a fluorophore are characterized by emission and excitation spectra, fluorescence quantum yield, and fluorescence lifetime.

Fluorescence quenching refers to a decrease in the emission intensity and can occur through two mechanisms: Collisional (sometimes called dynamic) and static quenching. In collisional quenching the excited state fluorophore encounters the quencher which affects its lifetime. The molecules are not chemically altered in this process.

The collisional quenching can be expressed by using Eq. 3.[43]

$$\frac{F_0}{F} = 1 + K_{SV}[Q] = 1 + k_q\tau_0[Q]$$
Eq. 3

where K_{SV} is the Stern-Volmer quenching constant, k_q is the biomolecular quenching constant,

τ_0 is the fluorophore lifetime and [Q] is the quencher concentration.

The Stern-Volmer quenching constant, K_{SV}, indicates the sensitivity of the fluorophore to the quencher. Typical quenchers in collisional quenching are oxygen-containing molecules, halogens, and amines. Quenching by halogens and heavy atoms occur due to spin-orbit coupling and intersystem crossing to the triplet state (Fig. 1.29).
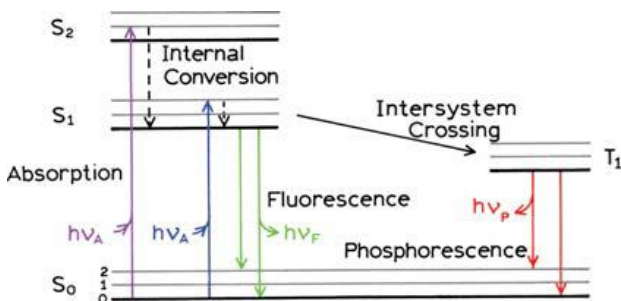
Figure 1.29. Jablonski diagram indicating intersystem crossing to the triplet state.[43]

Static quenching occurs when the fluorophore in the ground state forms a nonfluorescent complex with the quencher. This process does not rely on diffusion or molecular collision and is characterized by a decrease in the fluorescence emission, while the lifetime is not affected by the fluorophore.

In general, fluorescence measurements can be classified into two major types: Steady-state and time-resolved measurements. In a steady-state measurement, illumination and the observation of the emission occurs simultaneously. This measurement is the most common as many fluorophores exhibit lifetime of ns timescales. The second type is time-resolved measurements used for measuring intensity or anisotropy decays.

Ln^{3+} are uniquely fluorescent metals that show emission in aqueous solutions and decay times of 0.5 to 3 ms. Ln^{3+} exhibit line spectra and cannot be directly excited due to their low absorption so the presence of chelating organic ligands is employed to efficiently excite Ln^{3+} resulting in observable emission spectra. (Fig. 1.30).[43]
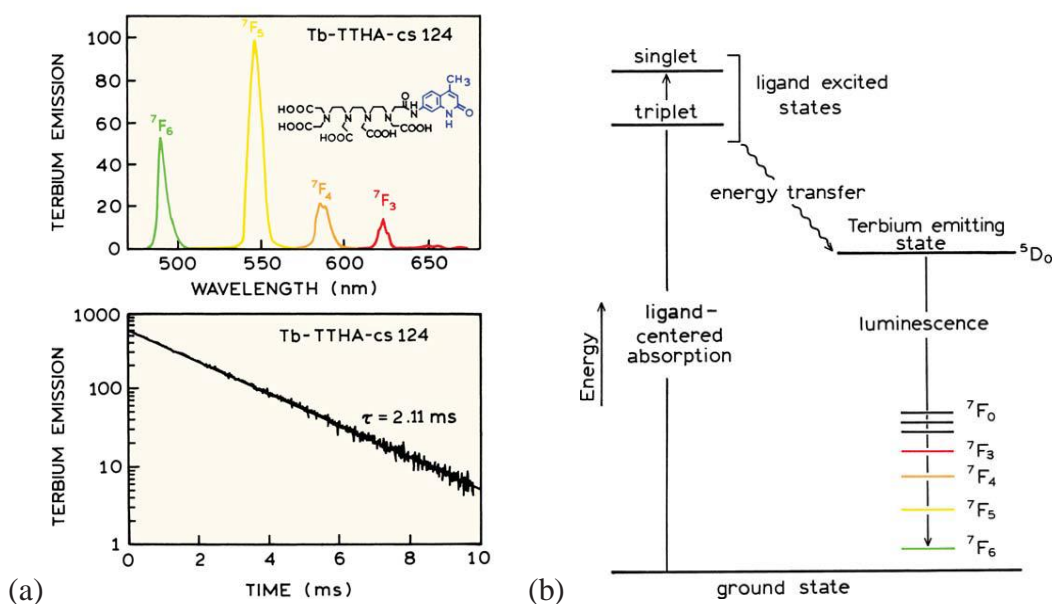
Figure 1.30. (a) Emission spectrum and intensity decay of Tb^{3+}. (b) Jablonski diagram for excitation of Tb^{3+} by energy transfer.[43]

1.8. Measuring binding constants using UV-Vis and fluorescence spectroscopy

For a simple 1:1 equilibrium system, the ligand L complexing with the substrate S forms a S:L complex according to scheme 1.1:[45]

25
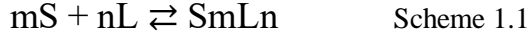
$mS + nL \rightleftarrows SmLn$ Scheme 1.1

The binding constant for substrate-ligand interaction as shown in Scheme 1.1 can be written as shown in Eq. 4:

$$K_a = K_{mn} = \frac{[S_mL_n]}{[S]^m[L]^n}$$ Eq. 4

The 1:1 binding isotherm can be derived from equilibrium constant to give Eq. 5:

$$f_{11} = \frac{K_a[S]}{1 + K_a[S]}$$ Eq. 5

where f_{11} is the fraction of the complexed receptor:

Ultimately f_{11} can be measured from equation 6 using the total concentrations of $[S_t]$ and $[L_t]$.

$$f_{11} = \frac{[L_t] + [S_t] + K_a^{-1} - \left(\left(\sqrt{([L_t] + [S_t] + K_a^{-1})^2 - (4[S_t][L_t])} \right) \right)}{2[L_t]}$$ Eq. 6

Determining binding affinity from UV-Vis and fluorescence spectra changes can be achieved from Eqs. 7 and 8.

$$\Delta A = \frac{[L_t] + [S_t] + K_a^{-1} - \left(\left(\sqrt{([L_t] + [S_t] + K_a^{-1})^2 - (4[S_t][L_t])} \right) \right)}{2[L_t]} \times \Delta A_{max}$$ Eq. 7

Where ΔA is the absorption change as the function of substrate concentration and ΔA_{max} is the maximum absorption change upon which the addition of substrate does not change the absorbance.

$$\Delta I = \frac{[L_t] + [S_t] + K_a^{-1} - \left(\left(\sqrt{([L_t] + [S_t] + K_a^{-1})^2 - (4[S_t][L_t])} \right) \right)}{2[L_t]} \times \Delta I_{max} \qquad \text{Eq. 8}$$

Where ΔI is the fluorescence change as the function of substrate concentration and ΔI_{max} is the maximum fluorescence change upon which the addition of substrate does not change the fluorescence.

1.9. Photoacoustic calorimetry (PAC)

Photoacoustic calorimetry (PAC) is a spectroscopic technique that allows for determination of thermodynamic parameters (reaction volume and enthalpy change) associated with the photo-triggered process. Unlike traditional optical techniques, such as absorption and fluorescence spectroscopy, in PAC measurements the heat is released upon photoexcitation. The release of the heat into the solvent leads to an increase in the temperature and concomitant volume expansion. Increase in the volume is associated with a photoacoustic wave that is readily detected by a photoacoustic detector. Based on the amplitude and time profile of the acoustic signal of the sample and reference compound, the reaction enthalpy and volume change can be determined.[46,47,48] Figure 1.31 shows a photoacoustic process and the instrumentation of a photoacoustic calorimetry system.
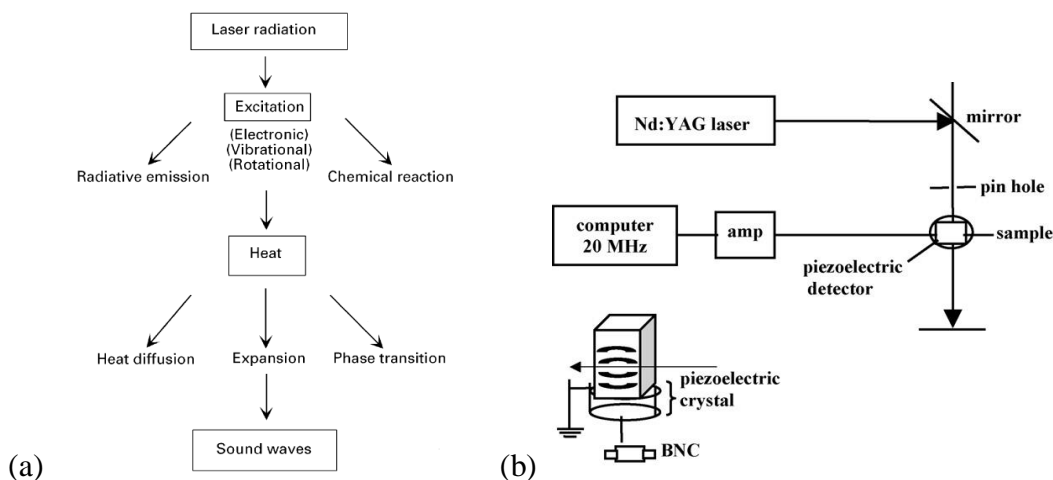
Figure 1.31. (a) Processes occurring during PA signal generation. The absorbed photon energy is partly transformed to heat and acoustic energy. (b) A diagram of photoacoustic calorimetry.[50-51]

This technique has the capacity of addressing the challenge of establishing the energetics of intervening and reacting species in chemical and biochemical reactions. For molecular complexes of lifetime less than 1 s, it has traditionally been very difficult to obtain direct thermochemical data. However, with the development of time-resolved photoacoustic calorimetry, it is now possible to obtain enthalpy changes associated with species having lifetime as short as 15 ns, provided that the reaction of interest can be initiated by the absorption of light.

The amplitude of the sample acoustic signal can be expressed according to Eq. 9. [48]

$$S = KE_a (\Delta V_{th} + \Delta V_{con}) \qquad \text{Eq. 9}$$

where S is amplitude of the acoustic signal for the sample, K is instrument response parameter, E_a is number of Einsteins absorbed, ΔV_{th} is solution volume changes due to thermal expansion,

ΔV_{con} is physical changes in the partial molar volume between the products and reactants and include the change in Van der Waals volume and/or solvation changes subsequent to photoexcitation.

The change in the solution volume resulting from the heat deposition can be expressed using Eq. 10.

$$\Delta V_{th} = \left(\frac{\beta}{C_p \rho}\right) Q \qquad \qquad \text{Eq. 10}$$

Where β is the thermoexpansion constant related to the solvent, C_p is the specific heat of the solvent and ρ is the density of the solvent. The contribution from ΔV_{th} and ΔV_{con} to the total signal, S, can be distinguished from performing similar experiments at different temperatures as the heat expansion is strongly dependent on temperature for water.

A calibration compound, in which $\Delta V_{con} = 0$, can be used to eliminate the instrument response parameter and the amplitude of acoustic signal for the calibration compound can be described as $R = \left(\frac{\beta}{C_p \rho}\right) E_a E_{h\vartheta}$, where E_a is the activation energy and $E_{h\vartheta}$ is the energy of the laser.

We can get the ratio of the sample to reference signal according to Eq. 11.

$$\left(\frac{S}{R}\right) E_{h\vartheta} = \phi E_{h\vartheta} = \left(Q + \left(\frac{C_p \rho}{\beta}\right) \Delta V_{con}\right) \qquad \text{Eq. 11}$$

$\left(\frac{S}{R}\right)$ can be defined as ϕ. Therefore, a plot of ϕE_{hv} versus $\frac{C_p \rho}{\beta}$ will give a straight line with a slope equal to ΔV_{con}. Also, the intercept will give Q, which is the heat released to the solvent that can be used to calculate the enthalpy. If the photochemistry of the compound does not occur 100%; in other words, all reactants do not convert to products, a correction value should be considered for determining ΔV_{con} and ΔH which equals the

quantum yield of the photodissociation of the compound. Eqs. 12 and 13 demonstrate the

corrected ΔH and ΔV$_{con}$ values.

$$\Delta H = \frac{E_{hv} - Q}{\varphi} \qquad\qquad \text{Eq. 12}$$

$$\Delta V_{con} = \frac{\Delta V}{\varphi} \qquad\qquad \text{Eq. 13}$$

References

1. Niedźwiecka, A.; Cisnetti, F.; Lebrun, C. and Delangle, P. Femtomolar Ln(III) Affinity in Peptide-based Ligands Containing Unnatural Chelating Amino Acids. *Inorg. Chem.* **2012**, *51*, 5458-5464.

2. Ye, Y.; Lee, H-W.; Yang, W.; Shealy, S. and Yang, J. J. Probing Site-Specific Calmodulin Calcium and Lanthanide Affinity by Grafting. *J. Am. Chem. Soc.* **2005**, *127*, 3743-3750.

3. Drobot, B.; Schmidt, M.; Mochizuki, Y.; Abe, T.; Okuwaki, K.; Brulfert, F.; Falke, S.; Samsonov, S. A.; Komeiji, Y.; Betzel, C.; Stumpf, T.; Raff, J. and Tsuchima, S. Cm^{3+}/Eu^{3+} induced structural, mechanistic and functional implications for calmodulin. *Phys. Chem. Chem. Phys.* **2019**, *21*, 21213-21220.

4. Hungerford, G.; Hussain, F.; Patzke, G. R. and Green, M. The photophysics of europium and terbium polyoxometalates and their intraction with serum albumin: a time-resolved luminescence study. *Phys. Chem. Chem. Phys.* **2010**, *12*, 7266-7275.

5. Gonzalez, W. G.; Ramos, V.; Diaz, M.; Garabedian, A.; Molano-Arevalo, J. C.; Fernandez-Lima, F. and Miksovska, J. Characterization of the Photophysical, Thermodynamics, and Structural Properties of the Terbium(III)-DREAM Complex. *Biochemistry*, **2016**, *55*, 1873-1886.

6. Brayshaw, L. L.; Smith, R. C. G.; Badaoui, M.; Irvig, J. A. and Price, S. R. Lanthanides compete with calcium for binding to cadherins and inhibit cadherin-mediated cell adhesion. *Metallomics*, **2019**, *11*, 914-924.

7. Geißler, D.; Linden, S.; Liermann, K.; Wegner, K. D.; Charbonniere, L. J. and Hilderbrandt, N. Lanthanides and Quantum Dots as Förster Resonance Energy Transfer Agents for Diagnostics and Cellular Imaging. *Inorg. Chem.* **2014**, *53*, 1824-1838.

8. Oukhatar, F.; Eliseeva, S. V.; Bonnet, C. S.; Placidi, M.; Logothetis, N. K.; Petoud, S.; Angelovski, G. and Toth, E. Toward MRI and Optical Detection of Zwitterionic Neurotransmitters: Near-Infrared Luminescence and Magnetic Properties of Macrocylic Lanthanide(III) Complexes Appended with a Crown Ether and a Benzophenone Chromophore. *Inorg. Chem.* **2019**, *58*, 13619-13630.

9. Rajendran, M.; Yapici, E. and Miller, L. W. Lanthanide-Based Imaging of Protein-Protein Interactions in Live Cells. *Inorg. Chem.* **2014**, *53*, 1839-1853.

10. Lehman-Andino, I.; Su, J.; Papathanasiou, K. E.; Eaton, T. M.; Jian, J.; Dan, D.; Albrecht-Schmitt, T. E.; Dares, C. J.; Batista, E. R.; Yang, P.; Gibson, J. K. and Kavallieratos, K. Soft-donor dipicolinamide derivatives for selective actinide(III)/ lanthanide(III) separation: the role of S- vs. O-donor sites. *Chem. Commun.* **2019**, *55*. 2441-2444.

11. Lima, L. M. P and Tripier, R. Cyclen-Based Lanthanide Complexes as Luminescent Anion Receptors. *Curr. Inorg. Chem.* **2011**, *1*, 36-60.

12. Gunnlaugsson, T. and Leonard, J. P. Responsive lanthanide luminescent cyclen complexes: from switching/sensing to supramolecular architectures. *Chem. Commun.* **2005**, 3114-3131.

13. Richardson, F. S. Terbium (III) and Europium (III) Ions as Luminescent Probes and Stains for Biomolecular Systems. *Chem. Rev.* **1982**, *82*, 541-552.

14. Gao, B.; Zhang, L. and Zhang, D. Effects of structures of bidentate Schiff base type bonded-ligands derived from benzaldehyde on the photoluminescence performance of polymer-rare earth complexes. *Phys. Chem. Chem. Phys.* **2018**, *20*, 4373-4385.

15. Gao, B.; Chen, L. and Chen, T. Effect of electron-donating substituent groups on aromatic ring on photoluminescence properties of complexes of benzoic acid-functionalized polysulfone with Eu(III) ions. *Phys. Chem. Chem. Phys.* **2015**, *17*, 25322-25332.

16. Hernández-Fuentes, C.; Ruiz-Guerrero, R.; de Jesus Morales-Ramirez, A.; Molina-Maldonado, P. and Medina-Velazquez, D. Y. New Mononuclear Complex of Europium (III) and Benzoic Acid: From Synthesis and Crystal Structure Solution to Luminescence Emission. *Crystals*, **2020**, *10*, 674-689.

17. Dai, Z.; Tian, L.; Ye, Z.; Song, B.; Zhang, R. and Yuan, J. A. Lanthanide Complex-Based Ratiometric Luminescence Probe for Time-Gated Luminescence Detection of Intracellular Thiols. *Anal. Chem.* **2013**, *85*, 11658-11664.

18. Hanaoka, K.; Kikuchi, K.; Kojima, H.; Urano, Y. and Nagano, T. Development of a Zinc Ion-Selective Luminescent Lanthanide Chemosensor for Biological Applications. *J. Am. Chem. Soc.* **2004**, *126*, 12470-12476.

19. Que, E. L. and Chang, C. L. A. Smart Magnetic Resonance Contrast Agent for Selective Copper Sensing. *J. Am. Chem. Soc*. **2006**, *128*, 15942-15943.

20. Gomes dos Santos, C. M. and Gunnlaugsson, T. The recognition of anions using delayed lanthanide luminescence: The use of Tb(III) based urea functionalized cyclen complexes. *Dalton Trans*. **2009**, 4712-4721.

21. Lima, L. M. P.; Lecointre, A.; Morfin, J-F.; de Blas, A.; Visvikis, D.; Charbonniere, L. J.; Platas-Iglesias, C. and Tripier, R. Positively Charged Lanthanide Complexes with Cyclen-Based Ligands: Synthesis, Solid-State and Solution Structure and Fluoride Interaction. *Inorg. Chem.* **2011**, *50*, 12508-12521.

22. Surender, E. M.; Bradberry, S. J.; Bright, S. A.; McCoy, C. P.; Williams, D. C. and Gunnlaugsson, T. Luminescent Lanthanide Cyclen-Based Enzymatic Assay Capable of Diagnosing the Onset of Catherer-Associated Urinary Tract Infections Both in Solution and within Polymeric Hydrogels. *J. Am. Chem. Soc*. **2017**, *139*, 381-388.

23. Burke, H. M.; Gunnlaugsson, T. and Scanlan, E. M. Glyzosylated lanthanides cyclen complexes as luminescent probes for monitoring glycosidase enzyme activity. *Org. Biomol. Chem.* **2016**, *14*, 9133-9145.

24. Sahoo, J.; Jaiswar, S.; Jena, H. S. and Subramanian, P. S. Sensing of Phosphate and ATP by Lanthanide Complexes in Aqueous medium and Its Application on Living Cells. *ChemistrySelect*, **2020**, *5*, 12878-12884.

25. Hirayama, T.; Taki, M.; Kodan, A.; Kato, H. and Yamamoto, Y. Selective labeling of tag-fused protein by tryptophan-sensitized luminescence of a terbium complex. *Chem. Commun*. **2009**, 3196-3198.

26. Luo, J.; Li, W-S.; Xu, P.; Zhang, L-Y. and Chen, Z-N. Zn^{2+} Responsive Bimodal Magnetic Resonance Imaging and Fluorescent Imaging Probe Based on a Gadolinium (III) Complex. *Inorg. Chem.* **2012**, *51*, 9508-9516.

27. Aroussi, B. E.; Guenee, L.; Pal, P. and Hamacek, J. Lanthanide-Mediated Supramolecular Cages and Host-Guest Interactions. *Inorg. Chem.* **2011**, *50*, 8588-8597.

28. Petoud, S.; Cohen, S. M.; Bünzli, J-C. G. and Raymon, K. N. Stable Lanthanide Luminescence Agents Highly Emissive in Aqueous Solution: Multidentate 2-Hydroxyisophthalamide Complexes of Sm^{3+}, Eu^{3+}, Tb^{3+}, Dy^{3+}. *J. Am. Chem. Soc*. **2003**, *125*, 13324-13325.

29. Shavaleev, N. M.; Scopelliti, R.; Gumy, F. and Bunzli, J-C. Modulating the Near-Infrared Luminescence of Neodymium and Ytterbium Complexes with Tridentate Ligands Based on Benzoxazole-Substituted 8-Hydroxyquinolines. *Inorg. Chem*. **2009**, *48*, 2908-2918.

30. Xu, L.; Pu, N.; Li, Y.; Wei, P.; Sun, T.; Xiao, C.; Chen, J. and Xu, C. Selective Separation and Complexation of Trivalent Actinide and Lanthanide by a Tetradentate Soft-Hard Donor Ligand: Solvent Extraction, Spectroscopy and DFT Calculations. *Inorg. Chem.* **2019**, *58*, 4420-4430.

31. Paulenova, A.; Alyapyshev, M. Y.; Babain, V. A.; Herbst, R.S. and Law, J. D. Extraction of Lanthanides with Diamides of Dipicolinic Acid from Nitric Acid Solution. I, *Separation Science and Technology*., **2008**, *43*, 2606-2618.

32. Geist, A.; Mullich, V.; Magnusson, D.; Kaden, P.; Modolo, G.; Wilden A. and Zevaco, T. Actinide (III)/Lanthanide(III) Separation via Selective Aqueous Complexation of Actinide(III) using a Hydrophilic 2,6-Bis(1,2,4-Triazin-3-YL)-Pyridine in Nitric Acids. *Solvent Extr. Ion Exch*. **2012**, *30*, 433-444.

33. Gorden, A. E. V.; DeVore,(II), M. A. and Maynard, B. A. Coordination Chemistry with f-Element Complexes for an Improved Understanding of Factors That Contribute to Extraction Selectivity. *Inorg. Chem.* **2013**, *52*, 3445-3458.

34. Adams, S. R. and Tsien, R. Y. Controlling Cell Chemistry with Caged Compounds. *Annu. Rev. Physiol.* **1993**, *55*, 755-784.

35. Gurney, A. M. *Flash photolysis of caged compounds*. Chapter 15, Department of pharmacology, United Medical & Dental Schools, St Thomas's Hospital, Lambeth Palace Road, London, UK. **1993**.

36. Faas, G. C.; Karacs, K.; Vergara, J. L. and Mody, I. Kinetic properties and DM-nitrophen Binding to Calcium and Magnesium. *Biophysical Journal.* **2005**, *88*, 4421-4433.

37. Dhulipala, G.; Rubio, M.; Michael, K. and Miksovska, J. Thermodynamic profile for urea photo-release from a N-(2-nitrobenzyl) caged urea compound. *Photochem. Photobiol. Sci.* **2009**, *8*, 1157-1163.

38. Kaplan, J. H. and Ellis-Davies, G. C. R. Photolabile chelators for the rapid photorelease of divalent cations. *Proc. Natl. Acad. Sci.* **1988**, *85*, 6571-6575.

39. Ciesienski, K. L.; Haas, K, L.; Dickens, M. G.; Tesema, Y. T. and Franz, K. J. A Photolabile Ligand for Light-Activated Release of Caged Copper. *J. Am. Chem. Soc.* **2008**, *130*, 12246-12247.

40. Holdgate, G. and Ward, W. H. J. Measurements of binding thermodynamics in drug discovery. *Drug Discovery Today*, **2005**, *10*, 1543-1549.

41. Leavitt, S. and Freire, E. Direct measurement of protein binding energetics by isothermal titration calorimetry. *Curr. Opin. Struct. Biol.* **2001**, *11*, 560-566.

42. Klostermeier, D. and Rudolph, M. G. *Biophysical Chemistry*; Taylor and Francis Group.,2017.

43. Lacowicz, J. R. *Principles of Fluorescence Spectroscopy*; Third edition, Springer, 2006.

44. Jameson, D. M. *Introduction to Fluorescence;* RC Press, Taylor & Francis Group.

45. Avlani, V. A.; Mcloughlin, D. J.; Sexton, P. M. and Christopoulos, S. A. The Impact of Orthosteric Radioligand Depletion on the Quantification of Allosteric Modulator Interaction. *J. Pharmacol. Exp. Ther.* **2008**, *325*, 927-934.

46. Peters, K. S. and Snyder, G. J. Time-Resolved Photoacoustic Calorimetry: Probing the Energetics and Dynamics of Fast Chemical and Biochemical Reactions. *Science.* **1988**, *241*, 1053-1057.

47. Miklos, A.; Schafer, S. and Hess, P. Photoacoustic Spectroscopy, Theory. *Encyclopedia of Spectroscopy and Spectrometry (Second Edition)*, **1999**, *3*, 2151-2158.

48. Larsen, R. W. and Miksovska, J. Time-resolved thermodynamics of ligand binding to heme proteins. *Coord. Chem. Rev.* **2007**, *251*, 1101-1127.

<center>**Chapter 2**</center>

<center>**Ln^{3+} coordination, extraction, and sensing by a bis-quinoline dipicolinamide derivative**</center>

Setareh Sakhdari, Indranil Chakraborty, Xinrui Zhang, Jaroslava Miksovska, and Konstantinos Kavallieratos*

*Corresponding author

2.1. Abstract

The coordination, sensing and extraction of Ln^{3+} by the bis-quinoline dipicolinamide ligand $DQPDH_2$ has been studied using UV-Vis, fluorescence, X-ray crystallography, FT-IR, and distribution experiments for Sm^{3+} and Eu^{3+} in CH_2Cl_2-Et_2O/NaOH (pH = 11.0). The X-ray structure of the Nd^{3+}-$DQPDH_2$ complex shows 1:1 Nd^{3+}:ligand complexation with an O-N-O coordination pattern to the ligand, which is typical for dipicolinamides, and additional coordination to NO_3^- counteranions and H_2O giving a 10-coordinate Nd^{3+} environment, overall. UV-Vis titration experiments using 3.0×10^{-5} M of $DQPDH_2$ and 1.0×10^{-2} M of Ln^{3+} in 1:4 CH_2Cl_2:CH_3CN at constant $DQPDH_2$ concentration showed a red shift in the absorption spectra from 324 nm to 340 nm upon Ln^{3+} addition. The 1:1 Ln^{3+}-$DQPDH_2$ association constants determined by non-linear regression analysis of UV-Vis titration data to the 1:1 binding isotherm were found to be $K_{11} = 2300 \pm 214$ M^{-1} for Eu^{3+}, $K_{11} = 1300 \pm 90$ M^{-1} for Nd^{3+}, $K_{11} = 2500 \pm 78$ M^{-1} for Dy^{3+}, $K_{11} = 2300 \pm 233$ M^{-1} for Yb^{3+}, and $K_{11} = 1300 \pm 58$ M^{-1} for Tb^{3+}. Addition of 2.0×10^{-2} M^{-1} of Ln^{3+} in 1:4 CH_2Cl_2:CH_3CN to 5.0×10^{-5} M of $DQPDH_2$ at constant $DQPDH_2$ concentration also showed fluorescence quenching of the $DQPDH_2$ emission at 405 nm. The binding constants

obtained from the fluorescence titration experiments for 1:1 $Ln^{3+}DQPDH_2$ complexation by similar analysis were $K_{11} = 1200 \pm 64$ M^{-1} for Eu^{3+}, $K_{11} = 2500 \pm 420$ M^{-1} for Nd^{3+}, $K_{11} = 1600 \pm 343$ M^{-1} for Dy^{3+}, $K_{11} = 3400 \pm 473$ M^{-1} for Yb^{3+}, and $K_{11} = 1500 \pm 170$ M^{-1} for Tb^{3+}. The Ln^{3+} -$DQPDH_2$ complexes were isolated by reaction of $DQPDH_2$ and Ln^{3+} nitrate salts and the resulting powders were analyzed by FT-IR and microanalysis, consistently providing complexes with 1:1 Ln^{3+}-$DQPDH_2$ stoichiometry. Shifts to lower frequency from ligand to the metal complexes were observed for the carbonyl stretching bands in the FT-IR spectra. Distribution experiments in 1:1 95%CH_2Cl_2:5%Et_2O/NaOH (pH = 11.0) solutions showed up to 72.5% of Eu^{3+} and 58.4% of Sm^{3+} extracted by $DQPDH_2$ into the organic phases. Slope analysis experiments performed in 95:5 CH_2Cl_2:Diethylether showed a slope of 0.87 in the $logD_{Eu}{}^{3+}$ *vs.* log[$DQPDH_2$] plot, which is strongly indicative of 1:1 metal complexation in consistency with all other reported experiments. These results with the bisquinoline dipicolinamide derivative are consistent with prior results in our group for Ln^{3+} sensing and complexation with other dipicolinamide ligands, and confirm the preference of these ligands to bind Ln^{3+}at 1:1 stoichiometric ratio in the presence of strongly coordinating counteranions, such as $NO_3{}^-$.

2.2. Introduction

Lanthanides (Ln) have many industrial, environmental, and biological applications, with several ligands designed to bind and separate Ln^{3+} in their most common trivalent state.[1-8] Lanthanides have seen widespread application in biological chemistry and magnetic resonance imaging (MRI), with examples including the use of Ce^{4+} for DNA hydrolysis,[9] and the use of Gd^{3+} due to its unique magnetic properties.[10] The sharp emission bands and long-lived nature of f-f luminescence in Ln^{3+} has led to the development of probes for

bioimaging and bioassay applications.[11] The use of Ln^{3+} complexes with their f-electrons provides a valuable alternative to transition metal complexes as fluorescent and phosphorescent materials, because they can address shortcomings, such as short luminescence lifetimes and small Stokes shifts. Ln^{3+} complexes, typically show large Stokes shifts upon excitation into the ligand states, with long excited state lifetimes and high quantum yields. As Ln^{3+} do not efficiently absorb light for bright emission due to forbidden 4f-4f transitions, using ligands that sensitize Ln^{3+} could be advantageous.[12] These ligands could function as antennas by absorbing UV-Vis light and transfer to metals which results in near-infrared (NIR) emission. Pyridine-, diketone-, DTPA- and hydroxyquinoline-based Ln^{3+} complexes have been reported for their favorable emission properties in the visible or near-IR that can be used for sensing and detection applications.[13,14-17] Ln^{3+} have a preference for high coordination numbers (typically 8 to 12), emit in long wavelengths, and have relatively long-lived excited states in solution (µs to sub-µs range for Yb^{3+} and Nd^{3+} - ms to sub-ms range for Eu^{3+}, Tb^{3+}, and Sm^{3+})[1]

Ln^{3+} separation by synthetic ligands has been a long-standing problem due to long-term radiotoxicity of minor An^{3+} in spent nuclear fuel, and the necessity of Ln^{3+} removal for effective transmutation of An^{3+} into less hazardous shorter-lived nuclides.[18] The partitioning of Ln^{3+} and An^{3+} via solvent extraction is a challenging hydrometallurgical separation due to the similarity of An^{3+} and Ln^{3+}.[18,19,20] Both Ln^{3+} and An^{3+} prefer hard oxygen donor sites, however introduction of softer N-donor ligands can introduce significant separation between Ln^{3+} and An^{3+}, as An^{3+} are less hard than Ln^{3+} with stronger covalent character due to the presence of 5f orbitals instead of 4f ones.[21,22,23a] Bipyridine, triazine, dipicolinamide and other dipicolinic acid derivatives have well-studied Ln^{3+}

complexation properties and have shown effective separation of An^{3+} from Ln^{3+} from aqueous nitric acid solutions into organic solvents.[18,19,20,24] Paulenova et al. (2008) found that dipicolinamide derivatives extract Ln^{3+} with an increase in distribution ratio for later lanthanides as a result of increased nitric acid concentration.[20a] Alyapyshev et al. (2014) employed 2,2'-dipyridyl-2,6-dicarboxylic acid diamide derivatives for An^{3+} complexation and An^{3+}/Ln^{3+} separation by extraction with increasing number of pyridine rings in the ligand structure enhancing An^{3+}/Ln^{3+} separation.[20b] Geist et al. (2012) have reported triazinyl pyridine-based ligands for selective extraction of An^{3+}/Ln^{3+}.[20c] Govor et al. in our group (2020) showed that in *o*-phenylenediamide-derived disulfonamides, Sm^{3+} is extracted from highly alkaline solutions (pH = 13.0-13.5) with theory indicating analogous potential for An^{3+} extraction.[25] Our group recently reported an experimental and theoretical comparison of oxo- vs thio- dipicolinamide analogs, showing that the thioamide derivative of the dipicolinamide ligand can selectively extract An^{3+} over Ln^{3+} and a 1:1 complexation ratio of dipicolinamide to Ln^{3+} in solution when highly coordinating anions (such as NO_3^-) are present, while a 3:1 ratio is preferred for the less coordinating iodide.[24] Kelley et al. (2017) found that in actinide-dipicolinate complexes, an increase in stability constant is observed as a result of significant increase in the energy degeneracy of the An^{3+} 5f orbitals with the dipicolinate molecular orbitals for heavier An^{3+}. The increase in energy degeneracy resulting in orbital mixing, is the main cause of covalent bonding in heavier An^{3+} rather than spatial orbital overlap.[23b] In addition, Xu et al. (2019) found that in phenanthroline-type ligands, the Am^{3+}-N bond has more covalent character than the Eu^{3+}-N bond.[26] Ren et al. (2020) found that in diglycolamide-type ligands, the introduction of ethyl or isopropyl groups on the nitrogen atoms will lead to an increase in the separation

of Eu^{3+} over Am^{3+}.[27] Le Borgne et al. (2003) found dipicolinamide derivatives with substituted tertiary amide side arms at the 2- and 6- positions of the central pyridine rings offer a variety of Ln^{3+} complexation with tridentate binding units with a decrease in the affinity of the tridentate cavity for Ln^{3+} as a result of increased steric congestion on the amide side arms.[23a] Ln^{3+} complexation with dipicolinamide derivatives containing the fluorescent quinoline moiety has not yet been studied, and the quinoline fluorophore has only seen very limited use in Ln^{3+} chemistry. Quinoline complexes of transition metals, such as Ir^{3+}, Pt^{2+}, and Ru^{2+}, typically absorb UV-Vis light at the 280 nm - 400 nm range with emissions at 596 - 634 nm.[28,29] Majee et al. have recently reported the use of the $DQPDH_2$ ligand, which combines quinoline with the dipicolinamide framework for Ni^{2+} and Cu^{2+} complexation.[30] Shavaleev et al. (2009) have reported an 8-hydroxyquinoline ligand that forms stable complexes with Nd^{3+} and Yb^{3+}. These ligands absorb between 250 nm and 400 nm with a maximum emission between 508 nm and 527 nm.[12] Imbert et al. (2004) synthesized Nd^{3+} and Yb^{3+} hydroxyquinoline-containing tetrapodal complexes as luminescent probes for immunoassays[15] while Magennis et al. (2002) utilized Er^{3+} tris(8-hydroxyquinoline) complexes for developing organic light emitting diodes (OLED).[16]

Herein, we combine the versatile quinoline fluorophore with the dipicolinamide ligand framework in the bis-quinoline dipicolinamide derivative $DQPDH_2$ for effective Ln^{3+} complexation, extraction, and sensing. We have demonstrated Ln^{3+} coordination by UV-Vis absorption, fluorescence spectroscopy, and FT-IR, with notable changes in spectroscopic properties. The formation of 1-1 complexes, which agrees with prior studies with other dipicolinamides (when NO_3^- is present) was confirmed both in solution (by non-linear regression analysis of UV-Vis and fluorescence binding data in CH_3CN) and in the

solid state by isolation and characterization of the isolated Dy^{3+}, Nd^{3+}, Yb^{3+}, Eu^{3+}, and Tb^{3+} complexes as well as the X-ray crystal structure of Nd^{3+}-DQPDH$_2$ complex. Eu^{3+} and Sm^{3+} extraction as high as 72.5% and 58.4% from alkaline solutions into 95:5 CH$_2$Cl$_2$:Diethylether was achieved with extraction slope analysis being consistent with 1-1 complexation in solution.

2.3. Results and discussions

2.3.1. Synthesis

Five Ln^{3+}-DQPDH$_2$ complexes were synthesized using solutions of DQPDH$_2$ in dichloromethane and Dy(NO$_3$)$_3$.5H$_2$O, Yb(NO$_3$)$_3$.5H$_2$O, Eu(NO$_3$)$_3$.6H$_2$O, Nd(NO$_3$)$_3$.6H$_2$O and Tb(NO$_3$)$_3$.6H$_2$O in acetonitrile. The reaction conditions for isolating these complexes are shown in Scheme 2.1. The resulting yellow solids of Ln^{3+}-DQPDH$_2$ complexes were insoluble in methanol, acetone, and chlorinated solvents and NMR spectra in DMSO-d$_6$ showed decomposition of the complexes, as the spectra obtained were identical with the spectra of DQPDH$_2$ in DMSO. The formulation of all isolated complexes confirming 1:1 DQPDH$_2$/Ln^{3+} stoichiometry was derived by elemental analysis and was found consistent with 1:1 complexation as Ln^{3+}(DQPDH$_2$)(NO$_3$)$_3$, typically also containing additional water and solvent molecules, presumably due to the need of Ln^{3+} to satisfy a large coordination sphere and the preference of oxygen over nitrogen for Ln^{3+}-binding.

2.3.2 X-ray structural characterization

The crystal structure of the ligand shows a complete molecule of the ligand within an asymmetric unit (Fig. 2.1(a)). The structure of Nd^{3+} complex (an Am^{3+} surrogate)[31] with DQPDH$_2$ shows 1-1 complexation with a formula of [Nd(DQPDH$_2$)](NO$_3$)$_3$.H$_2$O and Nd^{3+}

in the center residing in a ten-coordinated environment with one ligand attached as an O-N-O tridentate chelate, three bidentate NO_3^- and one coordinated water molecule. The average Nd-N and Nd-O bond distances are 2.627(4) Å and 2.53(6) Å respectively (Fig. 2.1(b)). Prior studies with dipicolinamides have shown that such complexation patterns through coordination of both properly-oriented amide O- and the pyridine N- sites to Ln^{3+} with additional first-sphere coordination to nitrate oxygens are preferred, when highly coordinating nitrate counteranions are present, while additional dipicolinamide ligands may participate in coordination, in the presence of less coordinating anions, such as iodides.[24] The two five-membered rings formed upon coordination of the tridentate ligand with the Nd center are satisfactorily planar, with mean deviations of 0.023(3) Å (for the plane constituted by Nd1, N1, C1, C16 and O2 atoms) and 0.011(3) Å (for the plane constituted by Nd1, N1, C5, C6 and O1 atoms). The chelate rings are almost coplanar with the two quinoline rings (dihedral angles between the five membered chelate rings and the quinoline rings are < 1 deg). Careful examination of the extended structure revealed two intramolecular and one intermolecular non-classical hydrogen bonding interactions (namely, C8-H8---O1, with H8---O1, 2.17 (10) Å and C8---O1, 2.791(8) Å; O15-H15B---N4, with H15---N4, 2.00 Å and O15---N4, 2.821(11) Å; O3-H3B---O10, with H3B---O10, 1.90 (5) Å and O3---O10, 2.585(13) Å (Fig. 2.2a-b). Examination of the extended structure revealed moderate offset π-π stacking interactions (Fig 2.2b), with centroid to centroid distances of 3.787 and 3.947 Å.
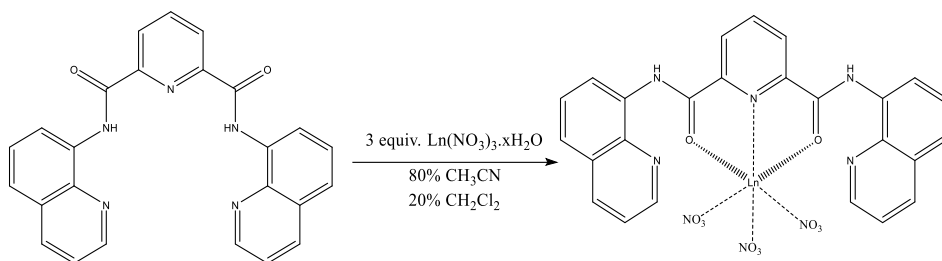
Scheme 2.1. Reaction conditions for formation of Ln^{3+}-DQPDH$_2$ complexes. Nitrates are presumably coordinating through their oxygen sites.

(a)

(b)

(c)

(d)
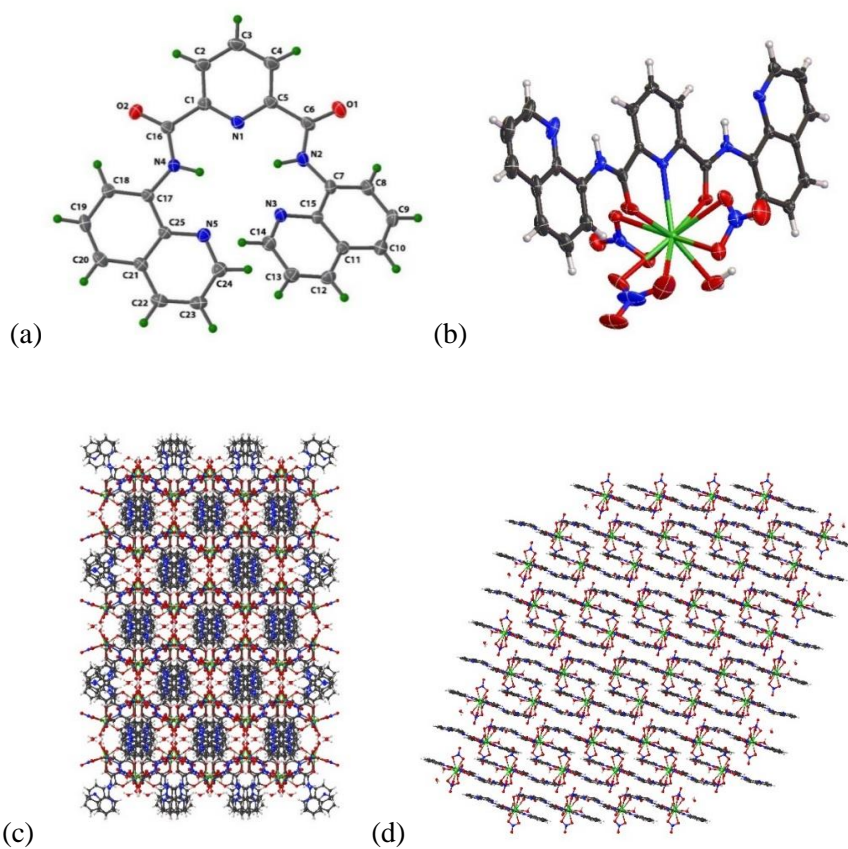
Figure 2.1. (a) Structure of DQPDH$_2$ (b) Molecular structure of [Nd(DQPDH$_2$)](NO$_3$)$_3$.H$_2$O. The thermal ellipsoids are shown at 50% probability level and water of crystallization is omitted for the sake of clarity. (c) and (d) The packing structure of [Nd(DQPDH$_2$)](NO$_3$)$_3$.H$_2$O

(a)   (b)
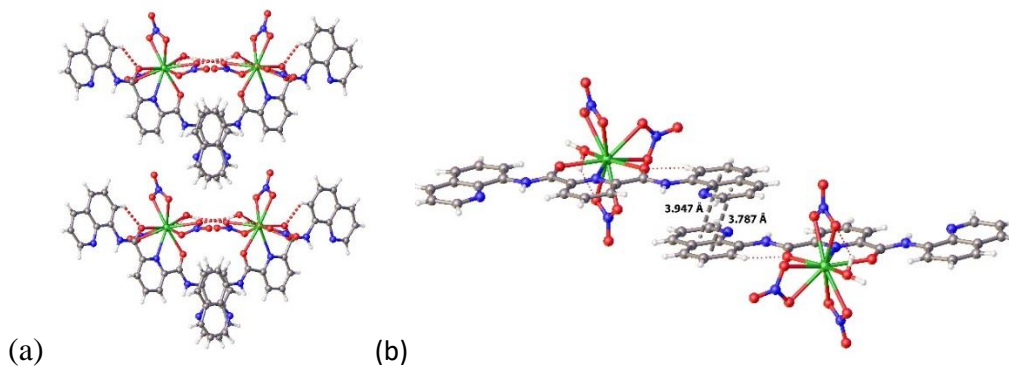
Figure 2.2. (a) Inter- and intramolecular H-bonding. (b) π-π stacking interactions between aromatic rings

2.3.3. UV-Vis titrations

Initial binding experiments were carried out by UV-Vis titrations: In the UV-Vis spectra (Figs. 2.3 and 2.4), DQPDH$_2$ shows maximum absorption at λ_{max} = 324 nm. Upon addition of several Ln^{3+} salts in 1:4 CH$_2$Cl$_2$/CH$_3$CN under constant ligand concentration the UV-Vis spectra show a red shift of the low energy transition from a λ_{max} of 324 nm to 340 nm for Eu^{3+}, Nd^{3+}, Dy^{3+} and Tb^{3+} additions and a transition from λ_{max} of 324 nm to 345 nm for Yb^{3+} addition in consistency with prior work with complexation of Ln^{3+} with dipicolinamides that shows a red shift of the low energy transition from λ_{max} of 282 nm to 300 nm.[24] Fitting of the titration curves for $\Delta A_{340\ nm}$ with increasing [Ln^{3+}] to the 1:1 binding isotherm provided the binding constants.[32]
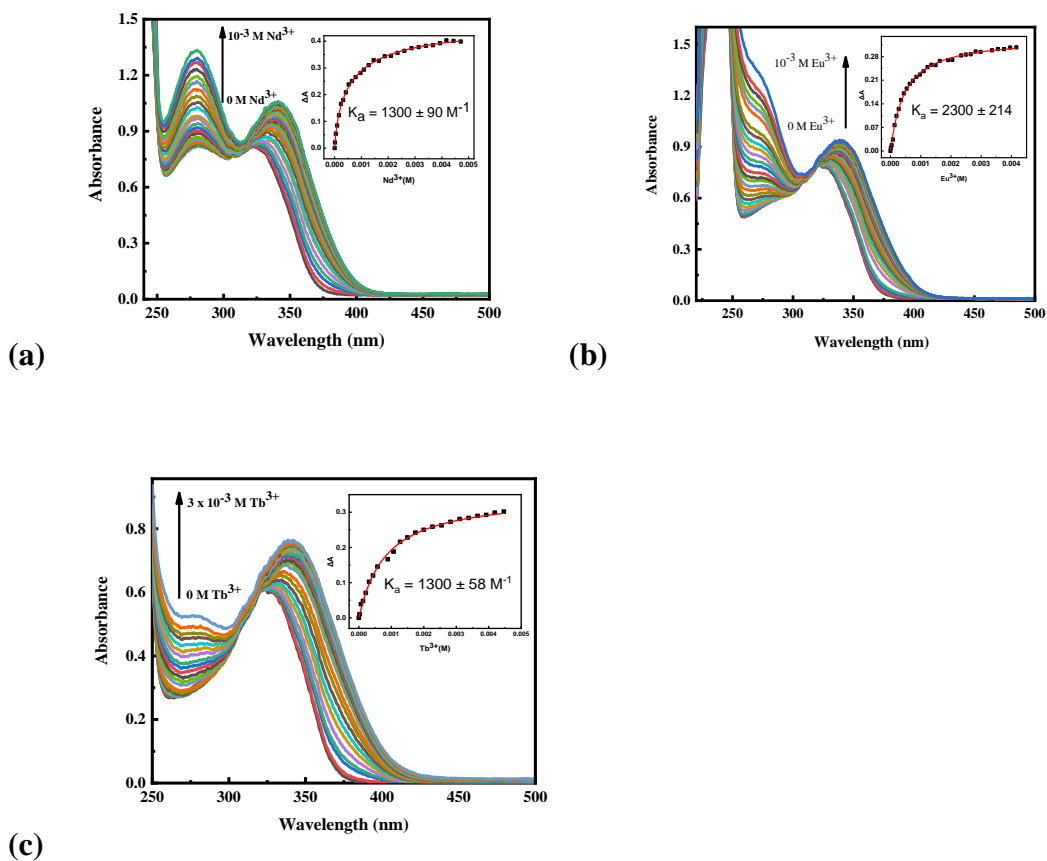
Figure 2.3. UV-Visible titration of DQPDH$_2$ in 1:4 CH$_2$Cl$_2$:CH$_3$CN (3.0 x 10^{-5} M) with Nd(NO$_3$)$_3$.6H$_2$O (1.0 x 10^{-2} M) (a), Eu(NO$_3$)$_3$.6H$_2$O (1.0 x 10^{-2} M) (b) and Tb(NO$_3$)$_3$.6H$_2$O (1.0 x 10^{-2} M) (c). The insets show the titration curve and fitting on the 1:1 binding isotherm. Binding constants were measured at λ = 340 nm.

45
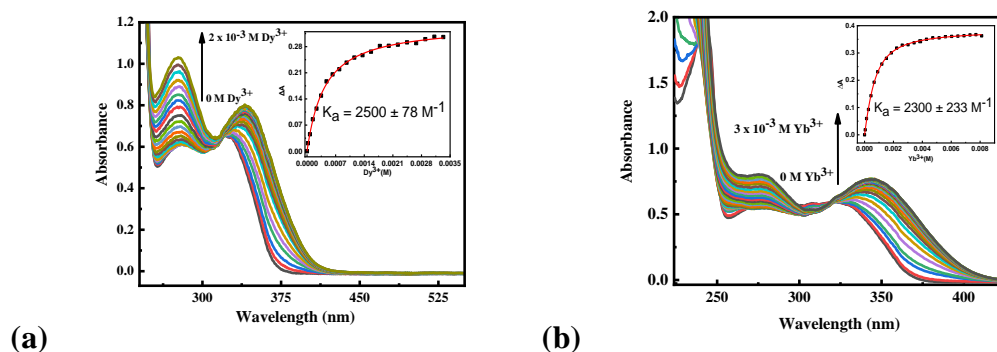
Figure 2.4. UV-Visible titration of DQPDH$_2$ (3.0 x 10^{-5} M) in 1:4 CH$_2$Cl$_2$:CH$_3$CN with Dy(NO$_3$)$_3$.5H$_2$O (1.0 x 10^{-2} M) (a) Yb(NO$_3$)$_3$.5H$_2$O (1.0 x 10^{-2} M) (b). The insets show the titration curve and fitting on the 1:1 binding isotherm. Binding constants for Dy^{3+} titration was measured at $\lambda = 340$ nm and for Yb^{3+} was measured at $\lambda = 345$ nm.

The red-shift of the absorption spectra is as a result of π-π* transitions[33-36] and the higher red-shift for Yb^{3+} could be as the result of its smaller ionic size compared to the other studied Ln^{3+}. The increase and the red shift of the absorption spectra when Ln^{3+} is added to the ligand is comparable with results from previous studies of dipicolinamide complexation with various Ln^{3+}.[24] The limit of detection (LOD) and the dynamic range (DR) for Ln^{3+} were calculated: For Eu^{3+} detection these are: LOD$_{Eu}$$^{3+}$ = 2.3 ($\pm$ 1.0) $\times$ 10^{-5} M and 8.5 $\times$ 10^{-4} M; for Nd^{3+} detection these are 1.00 ($\pm$ 0.05) $\times$ 10^{-5} M and 1.7 $\times$ 10^{-4} M; for Dy^{3+} detection these are 3.9 ($\pm$ 2.3) $\times$ 10^{-5} M and 6.0 $\times$ 10^{-4} M; for Yb^{3+} detection these are 6.3 ($\pm$ 0.2) $\times$ 10^{-5} M and 9.1 $\times$ 10^{-4} M, and for Tb^{3+} detection these are 6.0 ($\pm$ 0.03) $\times$ 10^{-5} M and 3.0 $\times$ 10^{-4} M.[37]

2.3.4. Fluorescence titrations

Fluorescence spectra of DQPDH$_2$ titration with Ln^{3+} (λ_{exc} = 270 nm) resulted in gradual quenching of the DQPDH$_2$ emission at λ = 405 nm and a slight red shift at the maximum

to 430 nm after addition of Eu^{3+}, Dy^{3+}, or Yb^{3+}, 411 nm after addition of Nd^{3+} and 415 nm after addition of Tb^{3+} (Figs. 2.5 and 2.6), which is also consistent with prior work with dipicolinamides that shows a quenching at $\lambda_{max} = 338$ upon addition of Ln^{3+}. Excitation at $\lambda_{exc} = 324$ nm did not produce an observable emission at 405 nm, thus a $\lambda_{exc} = 270$ nm was chosen, instead.

(a)

(b)

(c)

Figure 2.5. Fluorescence titration of $DQPDH_2$ (5.0 x 10^{-5} M) in 1:4 CH_2Cl_2:CH_3CN with $Nd(NO_3)_3.6H_2O$ (2.0 x 10^{-2} M) (a), $Eu(NO_3)_3.6H_2O$ (2.0 x 10^{-2} M) (b) and $Tb(NO_3)_3.6H_2O$ (2.0 x 10^{-2} M) (c). All spectra exhibit fluorescence quenching with slight red shift. The insets show the titration curve calculated based on the 1:1 binding isotherm. $\lambda_{exc} = 270$ nm and ΔE was measured at $\lambda = 405$ nm.

Figure 2.6. Fluorescence titration of DQPDH$_2$ (5.0 x 10^{-5} M) in 1:4 CH$_2$Cl$_2$:CH$_3$CN with Dy(NO$_3$)$_3$.5H$_2$O (2.0 x 10^{-2} M) (a) and Yb(NO$_3$)$_3$.5H$_2$O (2.0 x 10^{-2} M) (b). λ_{exc} = 270 nm and ΔE was measured at λ = 405 nm.

The higher red-shift of fluorescence quenching for Dy^{3+} and Yb^{3+} could be because of their smaller sizes compared to Tb^{3+} and Nd^{3+}. The red-shift for Eu^{3+} could be as the result of efficient energy transfer to the central metal. The observed fluorescence quenching is in agreement with previous studies by Cisse et al. (2017) and Verma et al. (2015), in which fluorescence quenching was observed after Ln^{3+} addition into solutions of carboxylic acid-type and diphenylamine-type ligands.[38,39]

Analysis of UV-Vis and fluorescence binding curves via non-linear regression and fitting to the 1-1 binding isotherm (Table 2.1) shows the values obtained for the K$_{11}$ binding constant of Ln^{3+} complexation to DQPDH$_2$ by UV-Vis and by fluorescence titrations. Values determined by UV-Vis and fluorescence spectra are within the same order of magnitude and show generally little variation along the Ln series.

Table 2.1. Binding constants for Ln^{3+}-DQPDH$_2$ with 1:1 complexation (1:4 CH$_2$Cl$_2$:CH$_3$CN) determined by UV-Vis/fluorescence

	Nd^{3+}	Eu^{3+}	Tb^{3+}	Dy^{3+}	Yb^{3+}
$K_{11(\text{UV-Vis})}(M^{-1})$	1300 ± 90	2300 ± 214	1300 ± 58	2500 ± 78	2300 ± 233
$K_{11(\text{Fluorescence})}(M^{-1})$	2500 ± 420	1200 ± 64	1500 ± 170	1600 ± 343	3400 ± 473

2.3.5. FT-IR spectra

Figure 2.7 shows the FT-IR spectra of the DQPDH$_2$ *vs.* several of its isolated Ln^{3+} complexes. DQPDH$_2$ has an intense band at 1678 cm^{-1} which is assigned to the C=O stretch of the carbonyl group. FT-IR spectra of the complexes show many similarities to each other, with the $\nu_{C=O}$ shifting to lower energy for Ln^{3+}-DQPDH$_2$ complexes (by 47-52 cm^{-1}), which is consistent with previous studies by Tang et al. (2006) with 1,3,4-oxadiazole amide-based ligands (25-40 cm^{-1}) and Świderski et al. (2016) with 2-pyridinecarboxylic acid ligand.[40,41] The band at 1524 cm^{-1} is assigned to $\nu_{C=N}$ of the ligand, and becomes weaker in intensity and slightly blue-shifted upon complexation, presumably because of higher contribution to binding by the $^+$N=C-O$^-$ resonance form vs. the N-C=O one. This is a characteristic shift in amide groups when coordinating through oxygen.[8,42] The intense band at around 1270-1290 cm^{-1} for the lanthanide complexes is due to N-O stretches of nitrate, indicating NO$_3^-$ presence in the metal complexes, in consistency with the microanalysis data and the X-ray structure for the Nd^{3+} complex.

Figure 2.7. FT-IR spectra of DQPDH$_2$ (a), Yb^{3+}-DQPDH$_2$ (b), Dy^{3+}-DQPDH$_2$ (c), Tb^{3+}-DQPDH$_2$ (d), Nd^{3+}-DQPDH$_2$ (e) and Eu^{3+}-DQPDH$_2$ (f).

2.3.6. Distribution experiments and determination of extraction stoichiometry

Extraction of Ln^{3+} from alkaline NaOH solutions (pH 11.0) into 95:5 CH$_2$Cl$_2$:Diethylether by DQPDH$_2$ was investigated after contact and equilibration, separation of the phases, and spectrophotometric analysis of the aqueous phases for quantification of Eu^{3+} and Sm^{3+} before and after contact with the ligand by the Arsenazo-III spectrophotometric method.[25] Two solutions of each for Ln^{3+}, Eu^{3+}, and Sm^{3+} were extracted with variation of ligand concentrations (1.0 mM – 4.0 mM). The concentration of Ln^{3+} was 0.04 mM and 95:5 CH$_2$Cl$_2$:Diethylether was used as the solvent. After 20 hours of extraction and 5 minutes separation, the aqueous phases were separated and analyzed by UV spectroscopy. Extraction efficiency was plotted in Figure 2.8. Up to 72.5% of Eu^{3+} and 58.4% of Sm^{3+} was extracted into the organic phase by the DQPDH$_2$ at pH 11.0. To determine the stoichiometry of the Eu^{3+} complex that is formed during extraction, slope analysis

50

experiments were carried out using solutions of increasing concentrations of DQPDH$_2$

ligand (1.0 mM to 4.0 mM mM) in 95:5 CH$_2$Cl$_2$:Diethylether. The presumed extraction

mechanism of two-phase equilibrium can be described as the following formula (3):

$$Eu^{3+}+3NO_3^-+nL \rightleftharpoons Eu(NO_3)_3(DQPDH_2)_n \qquad (3)$$

Where n is the coordination number of DQPDH$_2$, the corresponding extraction

equilibrium constant, K_{ex}, can be defined as:

$$K_{ex}=\frac{[Eu^{3+}(NO_3^-)_3(L)_n]}{[Eu^{3+}]_{aq}[NO_3^-]^3[L]^n} \qquad (4)$$

The distribution ratio of Eu^{3+} , D, can be represented as:

$$D= \frac{[Eu^{3+}]_{org}}{[Eu^{3+}]_{aq}} = \frac{[Eu(NO_3)_3(L)_n]}{[Eu^{3+}]aq} \qquad (5)$$

By substituting Equation (4) into Equation (5), and transforming Equation (5) into the log

form, Equation (6) and (6') are obtained:

$$logD = logK_{ex}+ nlog[L] + 3\log[NO_3] \qquad (6)$$

$$\log D = nlog[L] + C \qquad (6`)$$

Where C is the constant. Based on above analysis, keeping the pH value constant, the slope

of log-log plot regarding $D_{Eu}{}^{3+}$ vs. initial [DQPDH$_2$] present the number of extractant

molecules coordinated to Eu^{3+} ion in the organic phase. As shown in Figure 2.9, plotting

log $D_{Eu}{}^{3+}$ vs. log[DQPDH$_2$] for the DQPDH$_2$: Eu^{3+} ratio range between 20 - 100 eq. gave

a straight line with a slope of 0.87, which shows the presence of a species in the organic

phase that corresponds to a Eu^{3+}:DQPDH$_2$ ratio of almost 1:1, which is in accordance with

the species revealed by the UV-Vis and fluorescence titration experiments, and consistent with the stoichiometry of the isolated complexes. The extraction efficiency of Sm^{3+} is lower than for Eu^{3+}, which can be explained by some precipitation that was observed during the Sm^{3+} extraction experiment. The extraction efficiency for both these metals was found to be optimal at pH 11.0, as there is increasing precipitation when solutions of higher alkalinity are used. This observation is consistent with a prior study in our group using sulfonamide ligands for extraction of Ln^{3+} from alkaline solutions.[25]

(a)

(b)

Figure 2.8. (a) Extraction of Eu^{3+} (0.04 mM) by $DQPDH_2$ in 95% CH_2Cl_2:5% Et_2O from NaOH (pH = 11.0). (b) Extraction of Sm^{3+} by $DQPDH_2$ in 95% CH_2Cl_2:5% Et_2O from NaOH (pH = 11.0).

Figure 2.9. Slope analysis for Eu^{3+} extraction by $DQPDH_2$. Plot of $logD_{Eu}{}^{3+}$vs. log $[DQPDH_2]$ revealing a 1:1 Eu^{3+}: $DQPDH_2$ ratio.

2.4 Conclusions

$DQPDH_2$ forms 1:1 complexes with Ln^{3+} both in solution and in the solid state, as confirmed by spectroscopic and extraction experiments, microanalysis of the isolated complexes, and the X-ray structure of the Nd^{3+}-$DQPDH_2$ complex. The 1:1 formulation is consistent with previous studies with other dipicolinamide analogs in the presence of nitrate counteranions. The 1:1 complexation to dipicolinamide with coordination of oxophilic Ln^{3+} to nitrates to satisfy its coordination sphere is favored under these conditions. However, when nitrates are replaced by weakly coordinating counteranions such as iodides, formation of complexes with higher dipicolinamide to Ln^{3+} ratios was observed.[24] The UV-Vis absorption spectra of $DQPDH_2$ titration with Ln^{3+} indicate a shift to higher wavelength and the fluorescence titration of $DQPDH_2$ with Ln^{3+} leads to emission quenching consistent with previous dipicolinamide ligands reaction with Ln^{3+}.[24] No clear trend of increasing binding constant with decreasing Ln^{3+} radius was observed due to Ln^{3+} size contraction.[43,44] Slope analysis of the extraction results, titration curves of UV-Vis,

53

and fluorescence titrations, gave 1:1 metal: ligand stoichiometry with binding constants in the 10^{-3} M^{-1} range. The band for C=O at 1678 cm^{-1} for the ligand moved to lower wavenumbers with a decrease in intensity for all lanthanide complexes (~1630 cm^{-1}) while the band at 1524 cm^{-1} for C=N stretch moved to higher wavenumbers indicating the participation of the carbonyl oxygen and the pyridine nitrogen in binding to lanthanides which is in accordance with the results of elemental analysis. In conclusion, our investigation of binding of Ln^{3+} to $DQPDH_2$ indicates the capacity of bis (quinoline) dipicolinamide analogs with unique fluorescence properties for Ln^{3+} detection and separation from alkaline solutions, which could be useful for future Ln^{3+} detection and separation applications.

2.5. Experimental section

2.5.1. Materials and methods:

All chemicals were purchased from Fisher Scientific and were used as received without further purification unless stated otherwise. $Ln(NO_3)_3.6H_2O$ and $Ln(NO_3)_3.5H_2O$ salts were acquired from Fisher Scientific (> 99.9% purity). Spectroscopic grade high-purity (> 99.8%) solvents, including dichloromethane and acetonitrile were used for spectroscopic and extraction studies. UV-Vis spectra were recorded on a Shimadzu UV-2101 PC scanning spectrophotometer and fluorescence spectra were recorded on Cary Eclipse fluorescence spectrophotometer. FT-IR spectra were recorded on a Cary 600 series FT-IR spectrometer in the 400-4000 cm^{-1} region. ^{1}H- and ^{13}C-NMR spectra were recorded on a 400 MHz Bruker NMR spectrometer and were referenced using the residual solvent resonances. All chemical shifts, δ, are reported in ppm. N^2, N^6-di(quinoline-8-yl)pyridine-2,6-dicarboxamide ($DQPDH_2$) was synthesized as reported previously and was found

spectroscopically identical to the reported compound.[30a] Elemental analysis was obtained by Atlantic Microlab Inc.

2.5.2. Synthesis

Dy^{3+}-DQPDH$_2$ complex, [(Dy^{3+}-DQPDH$_2$)(NO$_3$)$_3$]: A solution of DQPDH$_2$ in dichloromethane (0.20 g; 0.5 mmol) was mixed with a solution of Dy(NO$_3$)$_3$.5H$_2$O in acetonitrile (0.70 g; 1.5 mmol). The resulting yellow precipitate was washed sequentially with acetonitrile and dichloromethane to remove any unreacted materials and dried *in vacuo*, giving 0.15 g (0.174 mmol) of the product (35% yield). Elemental analysis for C$_{25}$H$_{17}$N$_5$O$_2$Dy(NO$_3$)$_3$.2H$_2$O.4CH$_3$CN. 3CH$_2$Cl$_2$: Calcd. C, 35.36; H, 3.21; N, 13.74; Found C, 35.46; H, 2.74; N, 13.42. FT-IR (ATR, cm^{-1}): 1631(s, $\nu_{C=O}$), 1547 (m, $\nu_{C=N}$), 1491 (m, ν_{1N-O}) and 1276 (s, ν_{4N-O}).

Yb^{3+}-DQPDH$_2$ complex, [(Yb^{3+}-DQPDH$_2$)(NO$_3$)$_3$]: Synthesized using the same method as above for [(Dy-DQPDH$_2$)(NO$_3$)$_3$] from DQPDH$_2$ in dichloromethane (0.20 g; 0.5 mmol) and Yb(NO$_3$)$_3$.5H$_2$O in acetonitrile (0.70 g; 1.5 mmol) giving 0.18 g (0.2 mmol) of the product (41% yield). Elemental analysis for C$_{25}$H$_{17}$N$_5$O$_2$Yb(NO$_3$)$_3$.3H$_2$O.CH$_3$CN.CH$_2$Cl$_2$: Calcd. C, 35.09; H, 2.94; N, 13.15; Found C, 35.14; H, 2.72; N, 12.95 and FT-IR (ATR, cm^{-1}): 1631 (s, $\nu_{C=O}$), 1538 (m, $\nu_{C=N}$), 1486 (m, ν_{1N-O}) and 1290 (s, ν_{4N-O}).

Eu^{3+}-DQPDH$_2$ complex, [(Eu^{3+}-DQPDH$_2$)(NO$_3$)$_3$]: Synthesized by the same method as [(Dy-DQPDH$_2$)(NO$_3$)$_3$] from DQPDH$_2$ in dichloromethane (0.20 g; 0.5 mmol) and Eu(NO$_3$)$_3$.6H$_2$O in acetonitrile (0.70 g; 1.5 mmol) giving 0.14 g (0.16 mmol) of the product (28% yield). Elemental analysis for C$_{25}$H$_{17}$N$_5$O$_2$Eu.(NO$_3$)$_3$.H$_2$O.3CH$_3$CN.3CH$_2$Cl$_2$: Calcd.

C, 35.41; H, 2.97; N, 13.36; Found C, 35.73; H, 2.87; N, 13.31 and FT-IR (ATR, cm^{-1}):
1631(s, $\nu_{C=O}$), 1542 (m, $\nu_{C=N}$), 1449 (m, ν_{1N-O}) and 1272 (s, ν_{4N-O}).

Nd^{3+}-DQPDH$_2$ complex, [(Nd^{3+}-DQPDH$_2$)(NO$_3$)$_3$]: Synthesized by the same method as [(Dy-DQPDH$_2$)(NO$_3$)$_3$] from DQPDH$_2$ in dichloromethane (0.20 g; 0.5 mmol) and Nd(NO$_3$)$_3$.6H$_2$O in acetonitrile (0.70 g; 1.5 mmol) giving 0.16 g (0.19 mmol) of the product (38% yield) . Elemental analysis for C$_{25}$H$_{17}$N$_5$O$_2$Nd(NO$_3$)$_3$.4CH$_3$CN.4CH$_2$Cl$_2$: Caldc. C, 35.50; H, 2.98; N, 13.41; Found C, 35.90; H, 2.85; N, 13.48 and FT-IR was: 1626(s, $\nu_{C=O}$),1538 (m, $\nu_{C=N}$),1449 (m, ν_{1N-O}) and 1290(s, ν_{4N-O}).

Tb^{3+}-DQPDH$_2$ complex, [(Tb^{3+}-DQPDH$_2$)(NO$_3$)$_3$]: Synthesized by the same method as [(Dy-DQPDH$_2$)(NO$_3$)$_3$] from DQPDH$_2$ in dichloromethane (0.20 g; 0.5 mmol) and Tb(NO$_3$)$_3$.6H$_2$O in acetonitrile (0.70 g; 1.5 mmol) giving 0.19 g (0.19 mmol) of the product (38% yield) . Elemental analysis for C$_{25}$H$_{17}$N$_5$O$_2$Tb(NO$_3$)$_3$.3H$_2$O.CH$_3$CN.2CH$_2$Cl$_2$: Caldc. C, 33.84; H, 2.94; N, 12.25; Found C, 33.83; H, 2.56; N, 12.94 and FT-IR was: 1634(s, $\nu_{C=O}$),1548 (m, $\nu_{C=N}$),1487 (m, ν_{1N-O}) and 1279(s, ν_{4N-O}).

2.5.3. X-ray structures of DQPDH$_2$ and its Nd^{3+} complex

DQPDH$_2$ ligand in powder form (50 mg) was dissolved in 2 mL of dichloromethane and left for slow evaporation. The creamy yellow crystals were analyzed by X-ray crystallography. Crystals of the Nd^{3+}-DQPDH$_2$ complex were grown from a 1:1 reaction mixture of Nd(NO$_3$)$_3$.6H$_2$O and DQPDH$_2$, as follows: A solution of 50 mg of Nd(NO$_3$)$_3$.6H$_2$O in 2 mL of acetonitrile was added slowly to a solution of 50 mg of DQPDH$_2$ in 2 mL of dichloromethane allowing for slow mixing between the two solvents until yellow crystals formed. X-ray structure determination experimental details are

summarized in Tables 2.2 and 2.3. Data were collected on a Bruker D8 Quest single crystal X-ray diffractometer (PHOTON 100 CMOS detector for $DQPDH_2$ and PHOTON II detector for Nd^{3+}-$DQPDH_2$) with graphite monochromated Mo Kα radiation ($\lambda = 0.71073$ Å) by the ω-scan technique in the range of $6.3 \leq 2\theta \leq 49.2$ for $DQPDH_2$ and $5.6 \leq 2\theta \leq 50.8°$ for the complex. All data were corrected for Lorentz and polarization effects.[45] All the structures were solved with the aid of *SHELXT* program using intrinsic phasing.[46] The structures were then refined by a full-matrix least squares procedure on F by *SHELXL*.[47] All non-hydrogen atoms were refined anisotropically. Hydrogen atom positions were calculated geometrically and refined using the riding model. Multi-scan absorption corrections are applied using SADABS2. Calculations were performed using the OLEX2[48] and SHELXTL™[49] program packages.

Table 2.2. Experimental details for X-ray structure determination of DQPDH$_2$

Crystal data	
Chemical formula	C$_{25}$H$_{17}$N$_5$O$_2$
M_r	419.43
Crystal system, space group	Orthorhombic, $P2_12_12_1$
Temperature (K)	298
a, b, c (Å)	4.5206 (5), 16.9634 (17), 25.838 (3)
V (Å^3)	1981.4 (4)
Z	4
Radiation type	MoKa
μ (mm^{-1})	0.09
Crystal size (mm)	0.14 x 0.09 x 0.06
Data collection	
Diffractometer	Bruker D8 Quest PHOTON 100
Absorption correction	Multi-scan
T_{min}, T_{max}	0.682, 0.745
No. of measured, Independent and Observed [I>2σ(I)] reflections	
R_{int}	0.083
$(\sin \theta / \lambda)_{max}$ (Å^{-1})	0.587
Refinement	
$R[F^2>2\sigma(F^2)]$, $wR(F^2)$, S	0.045, 0.091, 1.05
No. of reflections	3344
No. of parameters	357
H-atom treatment	All H-atom parameters refined
$\Delta\rho_{max}$, $\Delta\rho_{min}$ (e Å^{-3})	0.14, -0.18

Table 2.3. Experimental details for X-ray structure determination of Nd^{3+}-DQPDH$_2$

Crystal data	
Chemical formula	$C_{25}H_{19}N_8NdO_{12}.H_2O$
Mr	785.74
Crystal system, space group	Monoclinic, C2/c
Temperature (K)	170
a, b, c (Å)	19.792 (3), 11.8523 (15), 27.051 (3)
β (°)	109.300 (2)
V (Å^3)	5989.1 (13)
Z	8
Radiation type	Mo$K\alpha$
μ (mm^{-1})	1.81
Crystal size (mm)	$0.30 \times 0.25 \times 0.15$
Data collection	
Diffractometer	Bruker D8 Quest PHOTON II
Absorption correction	Multi-scan SADABS 2016/2
T_{min}, T_{max}	0.659, 0.745
No. of measured, independent, and observed [$I>2\sigma(I)$]	33335, 5488, 5133
R_{int}	0.038
$(\sin \theta/\lambda)_{max}$ (Å^{-1})	0.602
Refinement	
R[$F^2 > 2\sigma(F^2)$], wR(F^2), S	0.048, 0.114, 1.18
No. of reflections	5488
No. of parameters	500
No. of restraints	3
H-atom treatment	H atoms treated by a mixture of independent and constraint refinement $w = 1/[\sigma^2(F_0^2) + (0.0341P)^2 + 77.1236P]$ where $P = (F_0^2 + 2F_c^2)/3$
$\Delta\rho_{max}$, $\Delta\rho_{min}$ (e Å^{-3})	2.25, -2.02

2.5.4. UV-Vis titrations

UV-Vis titrations were performed with solutions of DQPDH$_2$ in 1:4 CH_2Cl_2:CH_3CN titrated with solutions of Eu(NO$_3$)$_3$·6H$_2$O, Nd(NO$_3$)$_3$·6H$_2$O, Dy(NO$_3$)$_3$·5H$_2$O, Yb(NO$_3$)$_3$·5H$_2$O, or Tb(NO$_3$)$_3$·6H$_2$O at constant ligand concentration. In a typical experiment, a solution of DQPDH$_2$ (3.0×10^{-5} M) was titrated with a solution of

Ln(NO$_3$)$_3$·6H$_2$O or Ln(NO$_3$)$_3$.5H$_2$O (1.0 × 10^{-2} M) and DQPDH$_2$ (3.0 × 10^{-5} M), prepared by accurately weighing approximately 44.0 mg of Ln(NO$_3$)$_3$·6H$_2$O or Ln(NO$_3$)$_3$.5H$_2$O in a 10.0 mL volumetric flask and diluting with the solution of the ligand. For spectra collection, 2.20 mL of DQPDH$_2$ solution was added to the UV-Vis cuvette and the lanthanide solution was added in 10-200 μL increments until a total of ca 2 mL had been added.

2.5.5. Fluorescence titrations

Fluorescence titrations were performed using DQPDH$_2$ solutions in 1:4 CH$_2$Cl$_2$:CH$_3$CN titrated with solutions of Eu(NO$_3$)$_3$·6H$_2$O, Nd(NO$_3$)$_3$·6H$_2$O, Dy(NO$_3$)$_3$·5H$_2$O, Yb(NO$_3$)$_3$·5H$_2$O, or Tb(NO$_3$)$_3$·6H$_2$O at constant ligand concentration. The excitation wavelength at 270 nm produces an emission at 405 nm for the quinoline ligand. In a typical experiment, a solution of DQPDH$_2$ (5.0 × 10^{-5} M) in 1:4 CH$_2$Cl$_2$:CH$_3$CN was titrated with a solution of Ln(NO$_3$)$_3$.6H$_2$O or Ln(NO$_3$)$_3$.5H$_2$O (2.0 × 10^{-2} M) and DQPDH$_2$ (5.0 × 10^{-5} M), prepared by accurately weighing approximately 30.0 mg of Ln(NO$_3$)$_3$·6H$_2$O or Ln(NO$_3$)$_3$.5H$_2$O in 5 mL of volumetric flask diluting with the solution of the ligand. For spectra collection, 2.20 mL of the ligand solution was added to the cuvette and lanthanide solution was added in 10-200 μL increments until a total of 2 mL had been added.

2.5.6. Extraction experiments and analysis

The extraction experiments were carried out in 15 mL glass tubes at a 1:1 organic:aqueous phase volume ratio. The organic phases were solutions of DQPDH$_2$ (1 mM – 4 mM) in 95:5 CH$_2$Cl$_2$:Et$_2$O. The aqueous phases were Ln(NO$_3$)$_3$·6H$_2$O (0.04 mM) in sodium hydroxide at pH 11.0. For Eu^{3+}, 2.00 mL of the organic phase and 2.00 mL of aqueous

phase were mixed in a stoppered glass tube and rotated on a wheel (55 rpm, 20 h) at room temperature. For Sm^{3+}, 7.00 mL of the organic phase and 7.00 mL of aqueous phase were mixed in a stoppered glass tube and rotated on a wheel (55 rpm, 20 h) at room temperature. After contact for 20 hours at room temperature and 5 minutes centrifugation and separation, the concentration of metal ions in the aqueous phase before and after extraction was determined by the Arsenazo III spectrophotometric method.[25] All extraction experiments were conducted in duplicate. Eu^{3+} concentration analysis by UV-Vis was carried out by the procedure previously published by Xiong et al. (2009).[50] 1.50 mL of aqueous phase after extraction were obtained and mixed with 1.00 mL of 0.29 mM Arsenazo III and 2.00 mL of NaAc-HAc buffer. Then, 0.01 M HCl was used to dilute the solution to 10.0 mL. Sm^{3+} concentration analysis by UV-Vis followed the procedure previously published by Govor et al. (2020).[25] In this procedure, 5.00 mL of aqueous phase after extraction experiments were obtained and mixed with 1.00 mL of 1% ascorbic acid, 1.00 mL of 0.2 M formate buffer (pH 3.0) and 2.00 mL of 0.05% Arsenazo III solution. Then, HNO_3 was used to adjust the pH value to 2.6. DI water was used to dilute the solution to 25.0 mL. The extraction efficiency and distribution ratios were calculated using equation (1) and equation (2):

$$(1) \qquad E\% = \frac{[Ln^{3+}]_{(initial)} - [Ln^{3+}]_{(remaining\ in\ aqeous)}}{[Ln^{3+}]_{(initial)}}$$

$$(2) \qquad D = \frac{[Ln^{3+}]_{(org.)}}{[Ln^{3+}]_{(aq.)}} = \frac{[Ln^{3+}]_{(initial)} - [Ln^{3+}]_{(remaining\ in\ aqeous)}}{[Ln^{3+}]_{(remaining\ in\ aqeous)}}$$

Slope analysis was performed using 5% Et$_2$O and 95% CH$_2$Cl$_2$ as solvent. The concentration of ligand was varying from 1.00 mM to 4.00 mM, the concentration of metals was fixed at 0.04 mM in pH 11.0.

Acknowledgement

References

1. Gunnlaugsson, T.; Leonard, J. P.; Responsive lanthanide luminescent cyclen complexes: from switching/sensing to supramolecular architectures. *Chem. Commun.* **2005**, 3114–3131.

2. Lima, L. M. P.; Tripier, R.; Cyclen-Based Lanthanide Complexes as Luminescent Anion Receptors. *Curr. Inorg. Chem.* **2011**, *1*, 36-60.

3. Lima, L. M. P.; Lecointre, A.; Morfin, J-F; de Blas, A.; Visvikis, D.; Charbonniere, L. J.; Platas-Iglesis, C. and Tripier, R. Positively Charged Lanthanide Complexes with Cyclen-Based
Ligands: Synthesis, Solid-State and Solution Structure, and Fluoride Interaction. *Inorg. Chem.* **2011**, *50*, 12508−12521.

4. Surender, E. M.; Bradberry, S. J.; Bright, S. A.; McCoy, C. P.; Williams, D. C. and Gunnlaugsson, T. Luminescent Lanthanide Cyclen-Based Enzymatic Assay Capable of Diagnosing the Onset of Catheter-Associated Urinary Tract Infections,
Both in Solution and within Polymeric Hydrogels. *J. Am. Chem. Soc.* **2017**, *139*, 381−388.

5. Castro, G.; Bastida, R.; Macias, A.; Pérez-Lourido, P.; Platas-Iglesias, C. and Valencia, L. Lanthanide(III) Complexation with an Amide Derived Pyridinophane. *Inorg. Chem.* **2015**, *54*, 1671−1683.

6. Drahos, B. and Trávníček, Z. Synthesis of a Versatile Building Block Combining Cyclen-derivative DO3A with a Polyamine via a Rigid Spacer. *Molecules*, **2013**, *18*, 13940-13956.

7. Pope, S. J. A.; Kenwright, A. M.; Boote, V. A.; and Faulkner, S. Synthesis, and luminescence properties of dinuclear lanthanide complexes derived from covalently linked macrocyclic ligands. *DaltonTrans*. **2003**, 3780-3784.

8. Gao, B.; Zhang, L. and Zhang, D. Effects of structures of bidentate Schiff base type bonded-ligands derived from benzaldehyde on the photoluminescence performance of polymer–rare earth complexes. *Phys.Chem.Chem.Phys*. **2018**, *20*, 4373-4385.

9. Kitamura, Y.; Sumaoka, J. and Komiyama, M. Hydrolysis of DNA by Ce(IV)/EDTA complex. *Tetrahedron*, **2003**, *59*, 10403-10408.

10. Livramento, J. B.; Sour, A.; Borel, A.; Merbach, A. E. and Toth, E. A Starburst-Shaped Heterometallic Compound Incorporating Six Densely, Packed Gd^{3+} Ions. *Chem. Eur. J.* **2006**, *12*, 989 – 1003.

11. Caille, F.; Bonnet, C. S.; Buron, F.; Villette, S.; Helm, L.; Petoud, S.; Suzenet, F. and Toth, E. Isoquinoline-Based Lanthanide Complexes: Bright NIR Optical Probes and Efficient MRI Agents. *Inorg. Chem.* **2012**, *51*, 2522−2532.

12. Shavaleev, N. M.; Scopelliti, R.; Gumy, F. and Bunzli, J-C. G. Modulating the Near-Infrared Luminescence of Neodymium and Ytterbium Complexes with Tridentate Ligands Based on Benzoxazole-Substituted 8-Hydroxyquinolines. *Inorg. Chem,* **2009**, *48*, 2908-2918.

13. Andreiadis, E. S.; Gauthier, N.; Imbert, D.; Demadrille, R.; Pecaut, J. and Mazzanti, M. Lanthanide Complexes Based on β-Diketonates and a Tetradentate Chromophore Highly Luminescent as Powders and in Polymers. *Inorg. Chem*. **2013**, *52*, 14382−14390.

14. Caravan, P.; Ellison, J. J.; McMurry, T. J. and Lauffer, R. B. Gadollinium (III) Chelates as MRI Contrast Agents: Structure, Dynamics, and Applications. *Chem. Rev.* **1999**, *99*, 2293-2352.

15. Imbert, D.; Comby, S.; Chauvin, A-S. and Bunzli, J-C. G. Lanthanide 8-hydroxyquinoline-based podates with efficient emission in the NIR range. *Chem, Commun*, **2005**, 1432-1434.

16. Magennis, S. W.; Ferguson, A. J.; Bryden, T.; Jones, T. S.; Beeby, A. and Samuel, I. D. W. Time-dependence of erbium (III) tris (8-hydroxyquinolate) near-infrared photoluminescence: implications for organic light-emitting diode efficiency. *Synthetic Metals*, **2003**, *138*, 463-469.

17. (a) Sun, L-N.; Zhang, H-J.; Yu, J-B.; Yu, S-Y.; Peng, C-Y.; Dang, S.; Guo, X-M and Feng, J. Near-Infrared Emission Novel Tris (8-hydroxyquinolinate) lanthanide (III) complexes-Functionalized Mesoporous SBA-15. *Langmuir,* **2008**, *24*, 5500-5507. (b) Albrecht, M.; Osetska, O.; Klankermayer, J.; Frohlich, R.; Gumy, F. and Bunzli, J-C. G. Enhancement of near-IR emission by bromine substitution in lanthanide complexes with 2-carboxamide-8-hydroxyquinoline. *Chem. Commun*, **2007**, 1834-1836. (c) Deun, R. V.; Fias, P.; Driesen, K.; Binnemans, K. and Gorller-Walrand, C. Halogen substitution as an efficient tool to increase the near-infrared photoluminescence intensity of erbium(III) quinolinates in non-deutertaed DMSO. *Phys. Chem. Chem. Phys.*, **2003**, *5*, 2754-2757. (d) Curry, R.J. and Gillin, W. P. 1.54 μm electroluminescence from erbium (III) tris (8-hydroxyquinoline) (ERQ)-based organic light-emitting diodes. *Appl. Phys. Lett.* **1999**, *75*, 1380-1382.

18. Leoncini, A.; Huskens, J. and Verboom, W. Ligands for f-element extraction used in the nuclear fuel cycle. *Chem. Soc. Rev.,* **2017**, *46*, 7229-7265.

19. Gorden, A. E. V.; DeVore, M. A. and Maynard, B. A. Coordination Chemistry with f-Element Complexes for an Improved Understanding of Factors That Contribute to Extraction Selectivity. *Inorg. Chem.* **2013**, *52*, 3445−3458.

20. (a) Paulenova, A.; Alyapyshev, M. Y.; Babain, V. A.; Herbst, R. S and Law, J. D. Extraction of Lanthanides with Diamides of Dipicolinic Acid from Nitric Acid Solutions. I. *Separ. Sci. Tech.* **2008**, *43*, 2606-2618. (b) Alyapyshev, M. Y.; Babain, V. A.; Tkachenko, L. I.; Paulinova, A.; Popova, A. A. and Borisova, N. E. New Diamides of 2,2'-dipyridyl-6,6'-dicarboxylic Acid for Actinide-Lanthanide Separation. *Solvent Extr. Ion Exch.* **2014**, *32*, 138-152.

(c) Geist, A.; Mullich, U.; Magnusson, D.; Kaden, P.; Modolo, G.; Wilden, A. and Zevaco, T. Actinide (III)/Lanthanide (III) Separation Via Selective Aqeous Complexation of Actinides (III) using a Hydrophilic 2,6-Bis(1,2,4-Triazin-3-YL)-Pyridine in Nitric Acid. *Solvent Extr. Ion Exch.* **2012**, *30*, 433-444.

21. Hudson, M. J.; Harwood, L. M.; Laventine, D. M. and Lewis, F. W. Use of Soft Heterocyclic N-Donor Ligands to Separate Actinides and Lanthanides. *Inorg. Chem.* **2013**, *52*, 3414−3428.

22. Choppin, G. R. Comparative solution chemistry of the 4f and 5f elements. *J. Alloys. Compd.* **1995**, *223*, 174-179.

23. (a) Le Borgne, T.; Benech, J-M.; Floquet, S.; Bernardinelli, G.; Aliprandini, C.; Bettens, P. and Piguet, C. Monometallic lanthanide complexes with tridentate 2,6-dicarboxamidopyridine ligands. Influence of peripheral substitutions on steric congestion and antenna effect. *Dalton Trans.* **2003**, 3856–3868. (b) Kelley, M. P.; Su, J.; Urban, M.; Luckey, M.; Batista, E. R.; Yang, P. and Shafer, J. C. On the Origin of Covalent Bonding in Heavy Actinides, *J. Am. Chem. Soc.* **2017**, *139*, 9901−9908.

24. Lehman-Andino, I.; Su, J.; Papathanasiou, K.E.; Eaton, T.M.; Jian, J.; Dan, D.; Albrecht-Schmitt, T. E.; Dares, C. J.; Batista, E. R.; Yang, P.; Gibson, J. K. and Kavallieratos, K. Soft-donor dipicolinamide derivatives for selective actinide(III)/lanthanide(III) separation: the role of S- vs. O-donor sites. *Chem. Commun.,* **2019**, *55*, 2441.

25. Govor, E. V.; Morozov, A. N.; Rains, A. A.; Mebel, A. M. and Kavallieratos, K. Spectroscopic and Theoretical Insights into Surprisingly Effective Sm(III) Extraction from Alkaline Aqueous Media by *o*-Phenylenediamine-Derived Sulfonamides. *Inorg. Chem.* **2020**, *59*, 6884–6894.

26. Xu, L.; Pu, N.; Li, Y.; Wei, P.; Sun, T.; Xiao, C.; Chen, J. and Xu, C. Selective Separation and Complexation of Trivalent Actinide and Lanthanide by a Tetradentate Soft-Hard Donor Ligand: Solvent Extraction, Spectroscopy, and DFT Calculations. *Inorg. Chem.* **2019**, *58*, 4420-4430.

27. Ren, P; Wang, C-Z; Tao, W-Q; Yang, X-F; Yang, S-I; Yuan, L-Y; Chai, Z-F; and Shi, W-Q, Selective Separation and Coordination of Europium(III) and Americium(III) by Bisdiglycolamide Ligands: Solvent Extraction, Spectroscopy, and DFT Calculations. *Inorg. Chem.* **2020**, *59*, 14218-14228.

28. (a) Jarenmark, M.; Fredin, L. A.; Hedberg, J. H. J.; Doverbratt, I.; Persson, P. and Abrahamsson, M. A Homoleptic Trisbidentate Ru(II) Complex of a Novel Bidentate Biheteroaromatic Ligand Based on Quinoline and Pyrazole Groups: Structural, Electrochemical, Photophysical, and Computational Characterization. *Inorg. Chem.* **2014**, *53*, 12778−12790. (b) Zhao, Q.; Jiang, C-Y.; Shi, M.; Li, F-Y.; Yi, T.; Cao, Y. and Huang, C-H. Synthesis and Photophysical, Electrochemical, and Electrophosphorescent Properties of a Series of Iridium(III) Complexes based on Quinoline Derivatives and Different β-Diketone ligands. *Organometallics*, **2006**, *25*, 3631-3638. (c) Mandapati, P.; Braun, J. D.; Lozada, I. B.; Williams, J. A. G. and Herbert, D. E. Deep-Red Luminescence from Platinum Complexes of N^N- ^-Amido Ligands with Benzannulated N-Heterocyclic Donor Arms. *Inorg. Chem.* **2020**, *59*, 12504-12517.

29. Fredin, L. A.; Wallenstein, J.; Sundin, E.; Jarenmark, M.; Barbosa de Mattos, D. F.; Persson, P. and Abrahamsson, M. Excited State Dynamics of Bistridentate and Trisbidentate RuII Complexes of Quinoline-Pyrazole Ligands. *Inorg. Chem.* **2019**, *58*, 16354−16363.

30. (a) Majee, K.; Patel, J.; Das, B. and Padhi, S.K. μ-Pyridine-bridged copper complex with robust proton-reducing ability. *Dalton Trans.* **2017**, *46*, 14869-14879 (b) Majee, K.; Patel, J.; Rai, S.; Das, B.; Panda, B. and Padhi, S. K. Proton reduction by a nickel complex with an internal quinoline moiety for proton delay. *Phys.Chem.Chem.Phys.*, **2016**, *18*, 21640-21650.

31. Cross, J. M.; Villa, E. M.; Wang, S.; Diwu, J.; Polinski, M. J. and Albrecht-Schmitt, T. E. Synthesis, Structure, and Spectroscopic Properties of Plutonium and Americium Phosphites and the Redetermination of the Ionic Radii of Pu(III) and Am(III). *Inorg. Chem.* **2012**, *51*, 8419-8424.

32. Connors, K. A. Binding constants – the measurement of molecular complex stability. John Wiley & Sons, New York, Chichester, Brisbane, Toronto, Singapore 1987.

33. Comby, S.; Imbert, D.; Chauvin, A-S.; Bunzli, J-C. G.; Charbonniere, L. J. and Ziessel, R. F. Influence of Anionic Functions on the Coordination and Photophysical Properties of Lanthanide (III) Complexes with Tridentate Bipyridines. *Inorg. Chem.* **2004**, *43*, 7369-7379.

34. Shavaleev, N. M.; Scopelliti, R.; Gumy, F. and Bunzli, J-C. G. Near-Infrared Luminescence of Nine-Coordinate Neodymium Complexes with Benzimidazole-Substituted 8-Hydroxyquinolines. *Inorg. Chem.* **2008**, *47*, 9055-9068.

35. Chong, B. S. K. and Moore, E. G. Quantitative Sensitization Efficiencies in NIR-Emissive Homoleptic Ln(III) Complexes Using 2(5-Methylpyridin-2-yl)-8-Hydroxyquinoline. *Inorg. Chem.* **2018**, *57*, 14062−14072.

36. Shavaleev, N. M; Scopelliti, R.; Gumy, F.; Bunzli, J-C. G. Surprisingly Bright Near-Infrared Luminescence and Short Radiative Lifetimes of Ytterbium in Hetero-Binuclear Yb-Na Chelates. *Inorg. Chem.* **2009**, *48*, 7937–7946.

37. Araujo, P. Key aspects of analytical method validation and linearity evaluation. *J. Chromatogr. B.* **2009**, *877*, 2224-2234.

38. Cisse, L.; Djande, A.; Capo-Chichi, M.; Delattre, F.; Saba, A.; Brochon, J-C.; Sanouski, S,; Tine, A. and Aaron, J-J. Fluorescence Quenching of Two Coumarin 3-Carboxylic Acids by Trivalent Lanthanide Ions. *J. Fluoresc.* **2017**, *27*, 619-628.

39. Verma, P. Sawant, R. M. and Pal, H. Introguing multichannel photoinduced electron transfer in lanthanide(III)-diphenylamine systems. *Phys.Chem.Chem.Phys.* **2015**, *17*, 23214- 23225.

40. Tang, X-L.; Dou, W.; Chen, S-W.; Dang, F-F. and Liu, W-S. Synthesis, infrared and fluorescence spectra of lanthanide complexes with a new amide-based 1,3,4-oxadiazole derivative. *Spectrochimica Acta Part A.* **2007**, *68*, 349–353.

41. Świderski, G.; Kalinowska, J. M. and Lewandowski, M.W. Spectroscopic (IR, Raman, UV and fluorescence) study on lanthanide complexes of picolinic acid. *Vib. Spectrosc.* **2016**, *87*, 81-87.

42. Taha, Z. A.; Ajlouni, A. M.; Al-Hassan, K. A.; Hijazi, A. K. and Faiq, A. B. Syntheses, characterization, biological activity, and fluorescence properties of bis-(salicylaldehyde)-1,3-propylenediimine Schiff base ligand and its lanthanide complexes. *Spectrochimica Acta Part A.* **2011**, *81*, 317– 323.

43. Yue, B.; Sun, H-J.; Chen, Y-N.; Kong, K.; Chu, H-B. and Zhao, Y-L. DNA binding and antibacterial properties of ternary lanthanide complexes with salicylic acid and phenanthroline. *Appl. Organometal. Chem*. **2014**, *28*, 162-168.

44. Sonke, J. E. and Salters, V. J. M. Lanthanide-humic substances complexation. I. Experimental evidence for a lanthanide contraction effect. *Geochimica et Cosmochimica Acta*. **2006**, *70*, 1495-1506.

45. North, A. C. T.; Phillips, D. C.; Mathews, F. S. A Semi-empirical Method of Absorption Correction. *Acta Crystallogr. Sect. A*. **1968,** *24*, 351–359.

46. Sheldrick, G. M. Crystal Structure Refinement with SHELXL. *Acta Crystallogr. Sect. C Struct. Chem.* **2015**, *71*, 3–8.

47. Sheldrick, G. M. SHELXT - Integrated Space-Group and Crystal-Structure Determination. *Acta Crystallogr. Sect. A Found. Crystallogr.* **2015**, *71*, 3–8.

48. Dolomanov, O. V.; Bourhis, L. J.; Gildea, R. J.; Howard, J. A. K.; Puschmann, H. OLEX2: A Complete Structure Solution, Refinement and Analysis Program. *J. Appl. Crystallogr*. **2009**, *42,* 339–341.

49. Sheldrick, G. M. SHELXTL TM (V 6.14). Bruker Analytical X-ray Systems: Madison, WI 2000.

50. Liangping, X.; Zhonghua, F. and Tongzai, Y. Microanalysis of Europium in Solution by UV-Vis Spectrophotometry. *Chinese Journal of Rare Metals, 2009, 5,* 766-768.

<center>**Chapter 3**</center>

<center>**DM-nitrophen as a novel cage for Ln^{3+}: A thermodynamic, kinetic, and**</center>

<center>**spectroscopic study**</center>

Gangadhar Dhulipala, Setareh Sakhdari, Walter G. Gonzalez, Konstantinos Kavallieratos, and Jaroslava Miksovska*

*Corresponding author

3.1. Abstract

Caging has multitude of applications due to its potential for complexation and release of species with high temporal and spatial accuracy. DM-nitrophen is a popular calcium cage frequently used to investigate the role of Ca^{2+} in signaling processes *in vivo*. Lanthanides are popular Ca^{2+} biomimetics, as they exhibit several physical properties that are advantageous for the study of proteins. In this study, we show that lanthanides (Eu^{3+} and Nd^{3+}) bind strongly to DM-nitrophen and Tb^{3+} can be uncaged within 1 μs upon photolysis. Isothermal titration calorimetric measurements of Ca^{2+} displacement from DM-nitrophen by Ln^{3+} provide the equilibrium binding constants for Ln^{3+}DM-nitrophen complexation with K_{11} = 1.15 (± 0.71) × 10^{12} M^{-1} for Eu^{3+}, and 2.53 (± 1.71) × 10^{12} M^{-1} for Nd^{3+}. The kinetics and thermodynamics of Tb^{3+} release from DM-nitrophen were characterized using photoacoustic calorimetry (PAC). The photodissociation of DM-nitrophen cage was rapid and occurred within 2 μs upon cage photo-fragmentation and was associated with the similar reaction and enthalpy changes of -90 ± 40 kcal mol^{-1} for fast phase and -25 ± 21 kcal.mol^{-1} for slow phase for DM-nitrophen photodissociation. The corresponding volume changes were -13 ± 10 mL.mol^{-1} and 5.8 ± 5.0 mL.mol^{-1} respectively for fast and slow phases. The photodissociation of Tb^{3+}DM-nitrophen was also followed by enthalpy

changes of -36 ± 20 kcal mol^{-1} and -22 ± 10 kcal.mol^{-1} for fast and slow phases of Tb^{3+}DM-nitrophen photodissociation. Analogously, the volume changes associated to Tb^{3+}DM-nitrophen fragmentation were -5.5 ± 4.0 mL.mol^{-1} and 11 ±1 mL.mol^{-1} for fast and slow phases. The measured lifetime for photodissociation of Tb^{3+}DM-nitrophen was around 988 ns. These results demonstrate that DM-nitrophen can serve as an effective photolabile cage for oxophilic Ln^{3+}, which have similar coordination properties as Ca^{2+} and Mg^{2+}.

3.2. Introduction

The concept of "cage compound" has been proposed for caging biologically active species. These species are inert when they are trapped within a photo-removable cage and become activated upon exposure to light as they are released from the cage. These photolabile cage compounds are the precursors of active molecules which can be illuminated and release their active species.[1-3] Divalent cations having essential roles in physiological processes, such as Ca^{2+} and Mg^{2+}, can be caged by these compounds. The complexes can undergo photochemical processes that allow study of kinetics, and structural and regulatory mechanisms of biological species, which are associated with binding and release of these cations. Davies and Kaplan have reported synthesis of two caged calcium compounds, DM-nitrophen (dimethoxynitrophenyl-EDTA) and NP-EGTA that are frequently used to control intracellular Ca^{2+} concentrations and to probe the role of Ca^{2+} in regulating biological processes.[4-6] Both compounds employ a photosensitive 2-nitrophenyl group and EDTA or EGTA moiety, respectively, as a Ca^{2+} chelator. Excitation of the nitro-benzyl group leads to fast fragmentation of DM-nitrophen into two photoproducts, formation of a nitrosoacetophenone-substituted iminodiacetic acid and a concomitant increase in Ca^{2+} concentration. Despite the high affinity for Mg^{2+}, DM-nitrophen is most widely utilized to

cage Ca^{2+} to study Ca^{2+} signaling since DM-nitrophen exhibits a high affinity for Ca^{2+} (K_d 5-8 nM) that decreases upon illumination by a factor of 4×10^5 ($K_d \sim 3$ mM) with a relatively high quantum yield (0.18).[7,8]

Lanthanides (Ln^{3+}), commonly referred to as "rare earths", are trivalent metals with a broad range of biological and medical applications due to their magnetic and spectroscopic properties. Ln^{3+} are hard Lewis acids with high affinity to ligands with oxygen donor sites, such as multicarboxylate ligands. Oxygen atoms in these ligands have a chelating role and contribute to enhanced complex solubility and stability.[9-13] These metals can also be complexed by ligands containing oxygen and nitrogen atoms in their structures, such as tetra-substituted cyclen ligand, a 12-membered central tetraaza ring coordinated with four acetic acid groups (DOTA). The Ca^{2+} biomimetic properties of Ln^{3+} make them suitable for studying the Ca^{2+} binding proteins. Having similar ionic radii to Ca^{2+}, Tb^{3+} can inhibit cadherin-mediated cell adhesion, because of competitive binding with Ca^{2+}. As the Ca^{2+} binding sites in proteins, such as elastase, carp paralbumin, and troponin are juxtaposed to tryptophan, phenyl alanine, and tyrosine, the replacement of Ca^{2+} by Tb^{3+} in these proteins results in the enhancement of its emission.[14-16] Other cages include octadentate macrotricyclic Tb^{3+} luminescent chelators with four 2-hydroxyisophthalamide chelating units, in which the bicapped hydrogens topology creates a central cavity predisposed toward Ln^{3+} coordination.[17] Aryl-substituted 2,6-pyridinedicarboxamide derivatives have also been reported for Ln^{3+} complexation[18a] and caging[18b], with π-π stacking caused by cyclizing of the ring-closing olefin metathesis forming a trefoil knot, which enhances the stabilization of the 3:1 complex.[18b] As a polyaminocarboxylate entity, EDTA, mainly forms a 1:1 complex with both divalent and trivalent metal cations through its four carboxyl

atoms and two nitrogen atoms. EDTA binds to metals in a hexadentate, pentadendate, or tetradentate manner depending on the size of the coordinated metal ion. The stability of Ln^{3+}EDTA complexes is due to its large and positive entropy change during complex formation.[20] Previous measurements of Ln^{3+}EDTA binding constants using potentiometry indicate that binding constants vary across the lanthanide series, with La^{3+} and Lu^{3+} having the weakest and strongest affinities (10^{14} M^{-1} vs. 10^{19} M^{-1}) respectively.[19,20,21] DM-nitrophen, as an EDTA derivative, has also been investigated for Ln^{3+} complexation due to its favorable binding properties, ascribed to possible ligand field stabilization of the 4f electrons.

Characterization of the transient kinetics associated with the photo-uncaging of Ca^{2+} from DM-nitrophen by flash photolysis is challenging mainly due to the technical limitations associated with monitoring changes in Ca^{2+} concentration with Ca^{2+}-sensitive fluorescent probes.[8] Nonetheless, the kinetics for Ca^{2+} binding and photo-dissociation from DM-nitrophen have been characterized by several groups using flash photolysis techniques.[4,7,23] Ca^{2+} photo-release from DM-nitrophen has been previously determined to occur in less than 30 μs using a CaOrange-5N fluorescent indicator.[23] On the other hand, Faas et al. have reported a biphasic Ca^{2+} release with time constants of 15 μs and 2 ms by using an Oregon Green Bapta-5N probe.[3] In the presence of non-saturating Ca^{2+} concentrations, photo-released Ca^{2+} rebinds to unphotolysed DM-nitrophen with a bimolecular rate constant ranging from 3.0×10^7 $M^{-1}s^{-1}$ to 8×10^7 $M^{-1}s^{-1}$ leading to the detection of transient spikes in Ca^{2+} concentration. The rate constant for Ca^{2+} rebinding to the DM-nitrophen photoproduct has been reported to be identical to the rate constant for Ca^{2+} binding to the intact cage, $k_{on} \sim 3.0 \times 10^7$ $M^{-1}s^{-1}$. Due to the EDTA's high affinity for Mg^{2+}, DM-nitrophen

can also be employed as a Mg^{2+} cage, although the affinity of DM-nitrophen or its photoproduct for Mg^{2+} is significantly lower compared to Ca^{2+} ($K_d \sim 1.5$ -2.5 µM and K_d = 5.4 M, respectively).[3,25]

To determine time-resolved thermodynamic parameters associated with the photo-dissociation of the Tb^{3+}DM-nitrophen complex, we have employed the photoacoustic calorimetry (PAC) technique. PAC belongs to the family of photothermal methods that allow for the detection of time-resolved volume and enthalpy changes for fast photochemical and photobiological processes including reaction volume, activation enthalpy and entropy changes on nanosecond timescale. A typical PAC instrument consists of a sample holder that contains a solution of photoreactive species. As the light from the laser pulse is absorbed by the photoreactive materials, chemical reactions are initiated that cause the generation of heat and ultimately the expansion of the solution volume. This expansion results in the production of acoustic waves that are detected by an ultrasonic piezoelectric transducer and can be observed by the appearance of a signal in a digitizing oscilloscope.[27] We applied this technique to measure the kinetics and thermodynamics of photochemistry associated with Tb^{3+} photo-release from the DM-nitrophen on nano- to microsecond timescales. In addition to PAC, we have also studied the interaction of DM-nitrophen with Tb^{3+}, Eu^{3+} and Nd^{3+} by absorption spectroscopy and by isothermal titration calorimetry (ITC).

3.3. Results and discussion

To investigate Ln^{3+} binding to DM-nitrophen, we have monitored the change in absorbance of DM-nitrophen as a function of increasing Ln^{3+} concentration (Fig. 3.1).
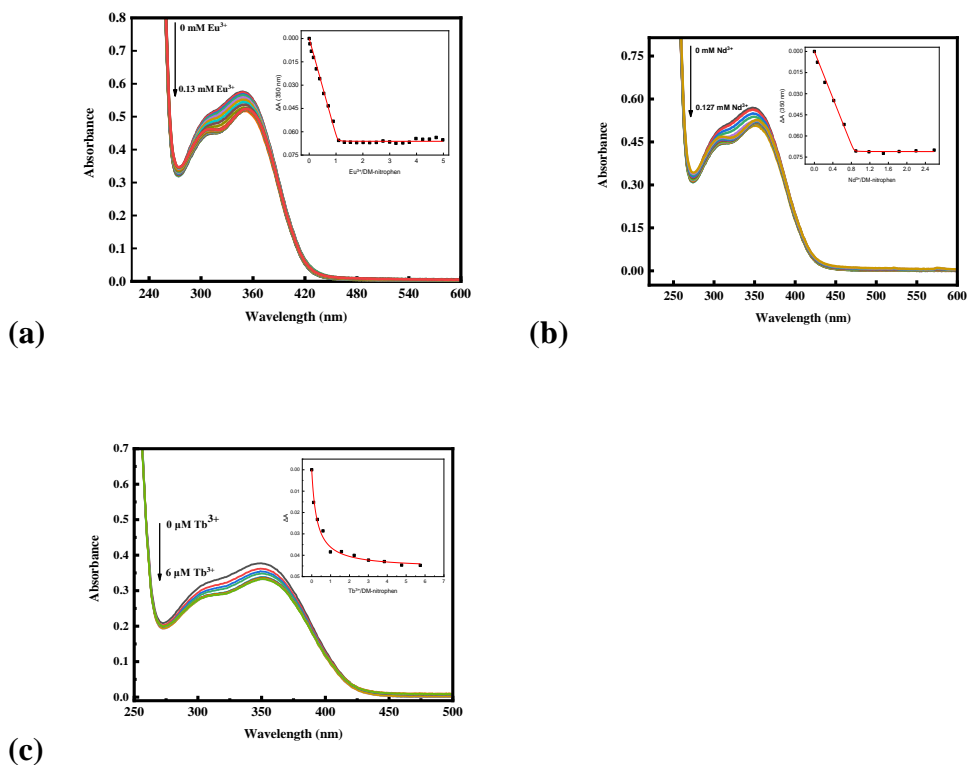
Figure 3.1. Absorption spectra of DM-nitrophen titrated with Eu^{3+} (a) Absorption spectra of DM-nitrophen titrated with Nd^{3+} (b). Absorption spectra of DM-nitrophen titrated with Tb^{3+} (c). Insets show Eu^{3+}, Nd^{3+} and Tb^{3+} binding curves to DM-nitrophen. The titrations were carried out in 20 mM MOPS pH 6.5 and 120 μM DM-nitrophen titrated with 1.4 mM Eu^{3+} and Nd^{3+}. For Tb^{3+} titrations 1 μM of DM-nitrophen was titrated with 10 μM Tb^{3+} in 20 mM MOPS pH 6.5 and 100 mM NaCl. The absorbance at 350 nm is plotted.

It has been shown previously that addition of Ca^{2+} or Mg^{2+} to DM-nitrophen leads to a decrease in the 350 nm absorption band.[2] In a similar way, addition of Ln^{3+} resulted in decrease of the absorption band at 350 nm. The plots of the absorbance change as a function of Ln^{3+} concentration show a steep transition between unbound and bound DM-nitrophen, indicating a strong Ln^{3+} affinity for DM-nitrophen. Analysis of such curves does not provide reliable affinity constants. However, the binding curves clearly indicates 1:1 ratio of Ln^{3+} to DM-nitrophen. A slightly lower ratio of 0.8:1 was observed for Nd^{3+} binding,

74

likely due to a small error in DM-nitrophen or Ln^{3+} solution concentration determination. When affinity constants are very large, (like in this case), they can be determined indirectly, using a displacement titration approach. The metal with higher affinity is added to the complex of ligand with bound metal of lower affinity. This method, however, cannot be used for absorption spectroscopy studies, for this case, because the absorption spectra of Ln^{3+}DM-nitrophen and Ca^{2+}DM-nitrophen complexes are nearly identical, preventing a clearly observed change in absorbance when displacement occurs. Therefore, to determine the affinity constants and thermodynamic parameters for Ln^{3+} binding to DM-nitrophen, we relied on ITC. Figure 3.2 shows the binding isotherms for Ln^{3+} displacement of Ca^{2+} from Ca^{2+}DM-nitrophen complex.

(a) (b)
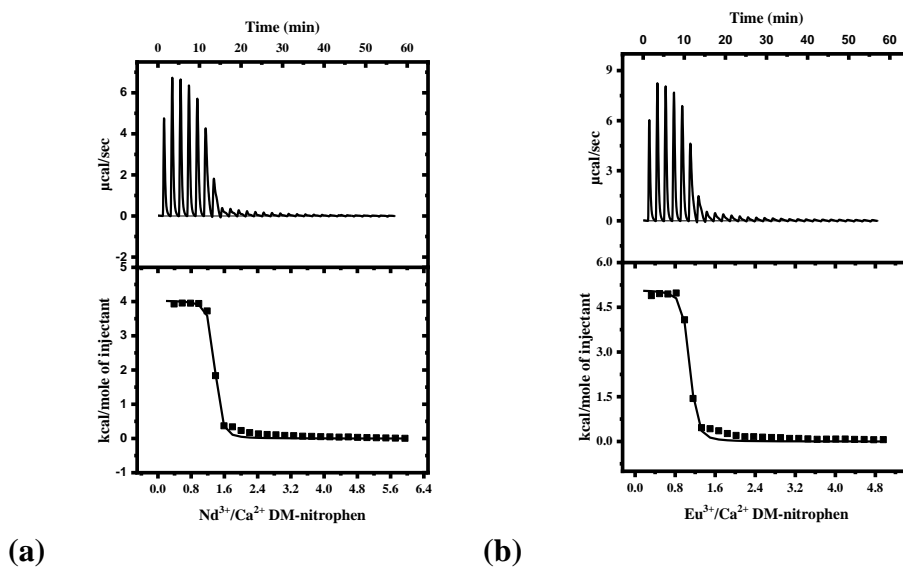
Figure 3.2. ITC isotherms for titration of Nd^{3+}(a), and Eu^{3+}(b), to Ca^{2+}DM-nitrophen.

The data were analyzed using a single binding site model to determine the apparent affinity constant and reaction enthalpy and entropy changes. Table 3.1 shows the affinity constants, enthalpy and entropy changes of Ln^{3+} binding to Ca^{2+}DM-nitrophen.

Table 3.1. ITC parameters recovered for Ln^{3+} displacement of Ca^{2+} from Ca^{2+}DM-nitrophen.

	N*	Ka (M^{-1})	ΔH (kcal.mol^{-1})	$T\Delta S$(kcal.mol^{-1})
Nd^{3+}DM-nitrophen	1.28	$(4.6 \pm 3.1) \times 10^6$	3.61 ± 0.06	12.4
Eu^{3+}DM-nitrophen	1.01	$(2.1 \pm 1.3) \times 10^6$	5.00 ± 0.12	13.4

*All experiments were carried out at 25 °C and reported errors correspond to standard deviations from three independent measurements. Enthalpy and entropy changes shown in kcal·mol^{-1}, association constants in M^{-1}. All experiments were carried out in triplicates.

The thermodynamic data clearly show that the displacement of Ca^{2+} bound to DM-nitrophen by Ln^{3+} is entropy driven. It is known that as the water molecules around Ca^{2+} are replaced by carboxylate groups of DM-nitrophen, the orientation of water molecules changes as they are released from binding with Ca^{2+}, making them more available for additional interaction with other solvent molecules. This phenomenon is responsible for positive reaction entropy. Regarding Ln^{3+}, it is noted that both Ca^{2+} and Ln^{3+} have high affinity to carboxylate groups because of similar ionic radii and coordination geometry preferences. The lanthanide contraction causes a decrease in ionic radii (Nd^{3+}>Eu^{3+}) with increasing atomic number for 6- and 8-coordinate complexes, which leads to greater charge density compared to that of Ca^{2+} ions. The higher charge density results in higher affinity of Ln^{3+} ions for Ca^{2+} sites. [28] The titration curve is associated with Ln^{3+} binding to Ca^{2+}DM-nitrophen.

Based on the apparent association constant for Eu^{3+} and Nd^{3+}, the displacement of Ca^{2+} together with the published equilibrium affinity constant of DM-nitrophen for Ca^{2+} ($K_{Ca}{}^{2+}=$

2×10^8 M^{-1}),[2] the affinity constant for Ln^{3+} ions binding to DM-nitrophen can be determined using Eq. 1:

$$K_{Ln^{3+}} = K_{app}(1 + K_{Ca^{2+}}[Ca^{2+}]) \qquad [1]$$

where $K_{Ca^{2+}}$ is the equilibrium association constant of Ca^{2+} binding to DM-nitrophen. [Ca^{2+}] is the concentration of Ca^{2+}, which is 2.75 mM for Eu^{3+} and Nd^{3+} displacement of Ca^{2+} DM-nitrophen. K_{app} is the apparent association constant for Ln^{3+} binding to Ca^{2+}DM-nitrophen. From this equation, the association constants for Eu^{3+} was calculated to be $K_{Eu^{3+}}$ = $(1.15 \pm 0.71) \times 10^{12}$ M^{-1} and for Nd^{3+} were calculated to be $K_{Nd^{3+}}$ = $(2.53 \pm 1.71) \times 10^{12}$ M^{-1}. The binding constant for Nd^{3+} binding to Ca^{2+}EDTA using ITC has been found to be $K_{Nd^{3+}}$ = $(4.22 \pm 2.31) \times 10^{12}$ (Table 3.1). The values of binding constants for Ln^{3+} binding to DM-nitrophen and the values of binding constant for Ln^{3+} binding to EDTA are relatively similar, indicating that the presence of nitrobenzyl moiety does not significantly change the affinity of the four carboxylate groups to Ln^{3+}. These results indicate that the published association constants for Eu^{3+}EDTA and Nd^{3+}EDTA (10^{16}M^{-1}) are higher than our results, which could be due to the different technique reported for the binding constant measurement (potentiometry) giving more accurate result about the strong binding.[19] The higher binding constant for Ln^{3+}DM-nitrophen compared to the one for Ca^{2+}DM-nitrophen shows that Ln^{3+} have higher affinity to DM-nitrophen, presumably because of their higher charge density.

3.3.1. Kinetics of DM-nitrophen complexes fragmentation

PAC traces for the photo-dissociation of DM-nitrophen and Tb^{3+}DM-nitrophen complexes are shown in Figure 3.3, together with corresponding reference traces. The PAC trace for Tb^{3+}DM-nitrophen photo-cleavage was measured at a [Tb^{3+}]:[DM-nitrophen]

ratio of 10:1 to ensure that the DM-nitrophen cage was fully saturated (Fig. 3.3). The appearance of the signal associated with the photolysis of DM-nitrophen appeared in lower frequency than the signal for the reference indicating that part of the laser energy was consumed for the photodissociation. The measured lifetime for the photodissociation of DM-nitrophen was around 2 μs while the measured lifetime for the photodissociation of Tb^{3+}DM-nitrophen was around 988 ns indicating that there is not significant difference between τ values for the photodissociation of DM-nitrophen and Tb^{3+}DM-nitrophen.

3.3.2. Thermodynamic profiles for DM-nitrophen fragmentation

The reaction volume and enthalpy changes associated with the photo-dissociation of DM-nitrophen can be determined from the acoustic waves generated from the PAC signal amplitude scaled to the amplitude of the reference signal. Plots of $\left(\dfrac{S}{R}\right) E_{h\vartheta}$ as a function of $\left[\dfrac{C_p\rho}{\beta}\right]$ for DM-nitrophen, and Tb^{3+}DM-nitrophen are shown in Figure 3.3 and values for the reaction enthalpy and volume change are listed in Table 3.2. The reaction volume change determined for the photo-dissociation of DM-nitrophen is -13 ± 10 mL mol^{-1}. DM-nitrophen fragmentation is coupled with a cleavage of two single covalent bonds and a formation of one single and one double bond (Scheme. 3.1). The negative volume change could be attributed to formation of the *aci*-nitro intermediate which causes a decrease in the volume while the positive volume change in the second phase of photodissociation could be as the result of the release of photoproducts that expand the volume. Analogously, the exothermic enthalpy changes of -90 ± 40 kcal mol^{-1} and -25 ± 21 kcal mol^{-1} observed for DM-nitrophen fragmentation can be associated with covalent bond reorganization subsequent to photo-excitation.[29,30]

78

(a)

(a')

(b)

(b')
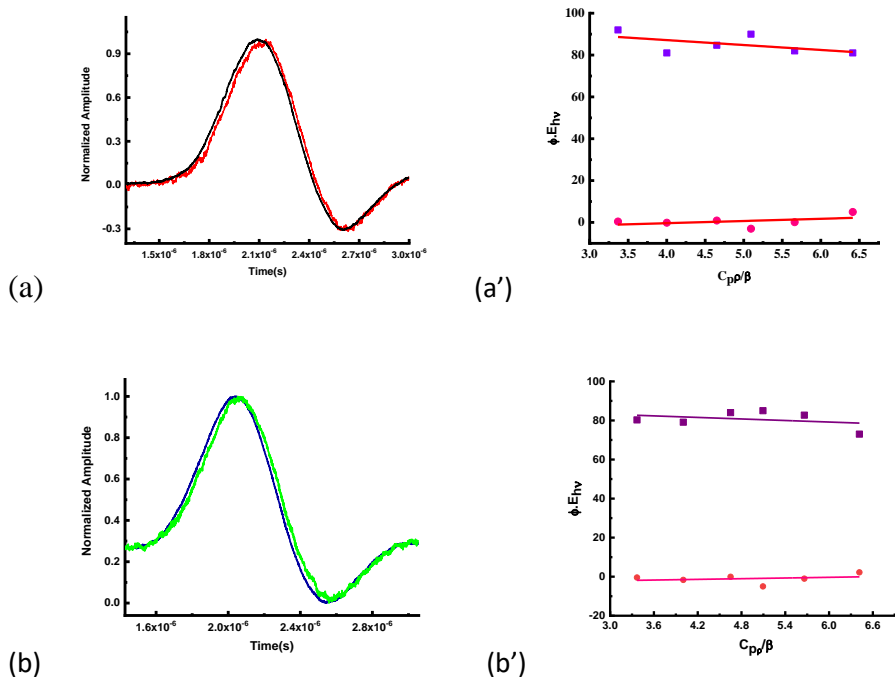
Figure 3.3. Overlay of PAC traces for the photolysis of DM-nitrophen (a) and Tb^{3+}:DM-nitrophen (b) with the reference compound. The amplitude for both traces were normalized to 1. Na_2CrO_4 was used as a reference compound. The absorption of the sample at 355 nm matched that of the reference compound ($A_{355} = 0.5$). Plot of $(\frac{S}{R})E_{h\vartheta}$ versus $\frac{C_{p}\rho}{\beta}$ for the photolysis of DM-nitrophen (a') and Tb^{3+}-DM-nitrophen (b').

Photo-dissociation of Tb^{3+}DM-nitrophen leads to two phases with an initial first/fast volume change followed by a second/slow volume change. The values are listed in Table 3.2. There is a small shift to the right in the PAC traces for the photocleavage of DM-nitrophen and Tb^{3+}DM-nitrophen compared to those of reference which indicates presence of a reaction intermediate with the time constant between 50 ns and ~ 5 μs. The negative volume determined for the first/fast phase could be attributed to the generation of the *aci*-nitro intermediate. The positive volume change associated with the second/slow phase is due to the production of the photoproducts and cleavage of two covalent bonds (Scheme 3.1).

Table 3.2. Volume and enthalpy changes associated with the photo-dissociation of DM-nitrophen, and Tb^{3+}:DM-nitrophen as determined from the plot of $(\frac{S}{R})E_{h\upsilon}$ versus $\frac{C_{p\rho}}{\beta}$ and scaled to $\Phi = 0.18$

	ΔV_1(ml mol^{-1})	ΔH_1(Kcal mol^{-1})	ΔV_2(ml mol^{-1})	ΔH_2(Kcal mol^{-1})
DM-nitrophen	-13 ± 10	-90 ± 40	5.8 ± 5.0	-25 ± 21
Tb^{3+}DM-nitrophen	-5.5 ± 4.0	-36 ± 20	11 ± 1	-22 ± 10

Scheme 3.1 demonstrates how bond rearrangement and cleavage are induced during the process of photodissociation of Tb^{3+}:DM-nitrophen.
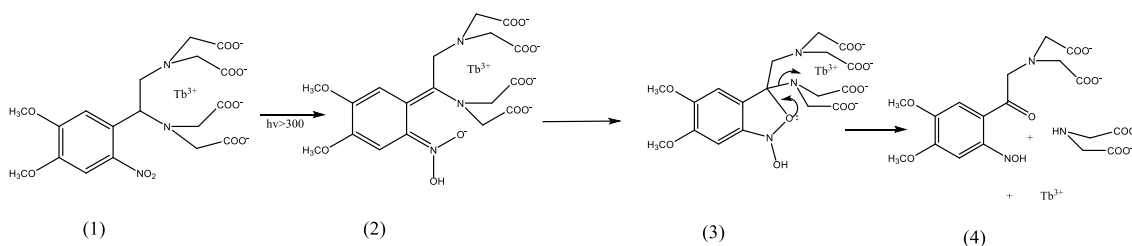
Scheme 3.1. The photodissociation of Tb^{3+}DM-nitrophen

3.4. Conclusion

The absorption spectra of Ln^{3+}DM-nitrophen titration shows that Ln^{3+} forms a complex with DM-nitrophen and both ions, Ln^{3+} and Ca^{2+}, have the same effect on the absorption spectra of DM-nitrophen. However, Ln^{3+} bind to DM-nitrophen with relatively higher binding constants compared to Ca^{2+}. Therefore, we carried out a displacement method using ITC to titrate Eu^{3+} and Nd^{3+} into Ca^{2+}DM-nitrophen and we measured equilibrium binding constants in the range of $\sim10^{12}$ M^{-1} for Ln^{3+} association to DM-nitrophen. The photo-dissociation of DM-nitrophen and Tb^{3+}DM-nitrophen occur within 1 μs. The volume and enthalpy changes of Tb^{3+}DM-nitrophen photofragmentation are comparable to those obtained from Ca^{2+}DM-nitrophen photofragmentation by PBD measurements showing that

Tb^{3+} could effectively mimic Ca^{2+} in studying the photocleavage of *o*-nitrobenzyl cage analogs. These results demonstrate that Ln^{3+} caging with DM-nitrophen is promising, and that the PAC technique in combination with caged compounds provides an attractive approach to monitor conformational changes in protein on sub-millisecond time-scale.

3.5. Experimental section:

3.5.1. Materials and methods

DM-nitrophen was purchased from Invitrogen Inc. and used as received. TbCl$_3$.6H$_2$O, Eu(NO$_3$)$_3$.6H$_2$O and Nd(NO$_3$)$_3$.6H$_2$O were purchased from Fisher Scientific. CaCl$_2$.2H$_2$O was purchased from Sigma-Aldrich. All chemicals were as received. Stock solutions of 1 mM DM-nitrophen samples were prepared by dissolving DM-nitrophen in 20 mM MOPS buffer pH 6.8. The stock solutions of Nd^{3+}, Eu^{3+} and Tb^{3+} were prepared by dissolving different concentrations of each Ln^{3+} in a DM-nitrophen solution with certain concentrations based on experimental procedure.

3.5.2. Steady-state absorption spectroscopy

Absorption spectra were recorded using a single beam UV-Vis spectrophotometer (Cary 50, Varian) and the DM-nitrophen concentration was determined from the absorbance at 350 nm ($\varepsilon_{350\ nm}$ = 4330 M^{-1}cm^{-1} for uncomplexed DM-nitrophen). 1.4 mM stock solutions of Eu^{3+} and Nd^{3+} were titrated into 120 μM DM-nitrophen solubilized in 20 mM MOPS buffer pH 6.8, under constant concentrations of DM-nitrophen. 0.1 μM of stock solutions of Tb^{3+} was titrated into 1.0 μM of DM-nitrophen in 20 mM MOPS buffer pH 6.8 and 100 mM NaCl.

3.5.3. Isothermal titration calorimetry

Thermodynamic parameters for lanthanide binding to DM-nitrophen and EDTA were determined using a VP-ITC titration calorimeter (Microcal Inc. Northampton, MA). For Ln^{3+}:DM-nitrophen experiments, the ITC buffer containing 20 mM MOPS pH 6.5 with 2.75 mM $CaCl_2$ for Nd^{3+}DM-nitrophen and Eu^{3+}DM-nitrophen experiments were prepared using ultrapure 18 MΩ water which was decalcified by filtering through a Chelex-100 resin (Bio-Rad). For the Ln^{3+}EDTA experiment, the ITC buffer contained 20 mM MOPS PH 6.5 with 1 mM $CaCl_2$ for Nd^{3+}EDTA experiments. The cell sample and injection syringe were extensively cleaned with decalcified water and then with ITC buffer. For Nd^{3+}DM-nitrophen and Eu^{3+}DM-nitrophen titrations, the reaction cell was loaded with 180 and 205 µM DM-nitrophen solution and the concentration of Nd^{3+} and Eu^{3+} in syringe were 5.0 and 4.75 mM. For Nd^{3+}EDTA titration, the reaction cell was loaded with 140 µM EDTA and the concentration of Nd^{3+} in syringe was 6 mM. Thirty injections (10 µL each) of Ln^{3+} were titrated into a ligand solution with 2 min intervals between injections. The temperature and the stirring speed were 25 °C and 307 rpm, respectively. All experiments were carried out in triplicates. The ITC results were analyzed using Origin 7 ITC data analysis software (OriginLab Corp. Northampton, MA).

3.5.4. PAC measurements

PAC measurements were performed in the laboratory based on the instrument designed for PAC. A laser pulse with the wavelength of 355 nm excites the sample which subsequently acoustic waves are produced. The laser pulse is generated from a frequency tripled Nd:YAG laser (5 ns pulse, 400 µJ pulse, Minilite II, Continuum, CA). DM-nitrophen

solution was prepared by dissolving the crystalline solid in a solvent of MOPS buffer. Before analyzing the photolysis of DM-nitrophen, a solution of sodium chromate as the reference was prepared in the MOPS buffer and placed in a cuvette with 1 cm × 0.5 cm size. The role of the reference for measuring the process of photodissoation of DM-nitrophen is to determine the enthalpy and volume changes based on the amplitudes of both reference and sample at different temperatures. After finalizing measurements for the reference, the analysis of DM-nitrophen solution started with the absorbance adjusted between 0.5-0.6 at 355 nm. The photolysis process was performed in different temperatures same to the reference solution (16°C-32°C).

Acknowledgement:

References

1. Adams, S. R.; Kao, J. P. Y.; Tsien, R. Y. Biologically Useful Chelators that take up Ca^{2+} upon illumination. *J. Am. Chem. Soc.* **1989,** *111,* 7957-7968.

2. Kaplan, J. H. and Ellis-Davies, G. C. R. Photolabile chelators for the rapid photorelease of divalent cations. *Proc. Nad. Acad. Sci.* **1988,** *85*, 6571-6575.

3. Faas, G. C.; Karacs, K.; Vergara, J. L. and Mody, I. Kinetic Properties of DM-Nitrophen Binding to Calcium and Magnesium. *Biophysical Journal,* **2005**, *88*, 4421–4433.

4. Zucker, R. S. Photorelease Techniques for Raising or Lowering Intracellular Ca^{2+} *Methods Cell Biol.* **1994**, *40*, 31-63.

5. Ellis-Davies, G. C. R. and Kaplan, J. H. A New Class of Photolabile Chelators for the Rapid Release of Divalent Cations: Generation of Caged Ca and Caged Mg. *J. Org. Chem.* **1988,** *53*, 1966-1969.

6. Ellis-Davies, G. C. and Kaplan, J. H. Nitrophenyl-EGTA, a photolabile chelator that selectively binds Ca^{2+} with high affinity and releases it rapidly upon photolysis. *Proc. Natl. Acad. Sci.* **1994,** *91*, 187-191.

7. Faas, G. C.; Karacs, K.; Vergara, J. L. and Mody, I. Measuring the kinetics of calcium binding proteins with flash photolysis. *Biochim. Biophys. Acta.* **2011**, *1820*, 1195-1204

8. Escobar, A. L.; Cifuentes, F. and Vergara, J. L. Detection of Ca^{2+}-transients elicited by flash photolysis of DM-nitrophen with a fast calcium indicator. *FEBS Lett.* **1995**, *364*, 335-338

9. Martinez-Gomez, N. C.; Vu, H. N. and Skovran, E. Lanthanide Chemistry: From Coordination in Chemical Complexes Shaping Our Technology to Coordination in Enzymes Shaping Bacterial Metabolism. *Inorg. Chem.* **2016**, *55*, 10083−10089.

10. Massi, M. and Ogden, M. Luminescent Lanthanoid Calixarene Complexes and Materials. *Materials,* **2017**, *10*, 1369-1378.

11. Da Souza, K. M. N.; Batista, H. J.; Belian, M. F.; Silva, W. E. and da Silva, J. A. B. A comparative study of the structure and luminescence of mono- and dinuclear crown-ether lanthanide complexes. *J. Lumin.* **2016**, *170*, 571–587.

12. Belian, M. F.; de Sa, G. F.; Alves, S. and Galembeck, A. Systematic study of luminescent properties of new lanthanide complexes using crown ethers as ligand. *J. Lumin.* **2011**,*131*, 856–860.

13. Sardar, P. S.; Samanta, S.; Roy.; M. B. and Ghosh, S. Dependence of photoinduced energy transfer on orientation of acceptor lanthanide ions with respect to π-plane of naphthalene in naphthalene linked six-member crown ethers. *Molecular Physics*, **2008**, *106*, 827-840.

14. Brittain, H. G.; Richardson, F. S. and Martin, R. B. Terbium (III) Emission as a Probe of Calcium (II) Binding Sites in Proteins. *Am. Chem. Soc.* **1976,** *98***,** 8255-8260.

15. Jersey, J. and Martin, R. B. Lanthanide Probes in Biological Systems: The Calcium Binding Site of Pancreatic Elastase as Studied by Terbium Luminescence. *Biochemistry,* **1980**, *19*, 1127-1132.

16. Brayshaw, L. L.; Smith, R. C. G.; Badaoui, M.; Irving, J. A. and Price, S. R. Lanthanides compete with calcium for binding to cadherins and inhibit cadherin-mediated cell adhesion. *Metallomics*, **2019**, *11*, 914-922.

17. Xu, J.; Corneillie, T. M.; Moore, E. G.; Law, G-L.; Butlin, N. G. and Raymond, K. N. Octadentate Cages of Tb(III) 2-Hydroxyisophthalamides: A New Standard for Luminescent Lanthanide Labels. *J. Am. Chem. Soc.* **2011**, *133*, 19900–19910.

18. (a) Lehman-Andino, I.; Su, J.; Papathanasiou, K. E.; Eaton, T. M.; Jian, J.; Dan, D.; Albrecht-Schmitt, T. E.; Dares, C. J.; Batista, E. R.; Yang, P.; Gibson, J. K.; Kavallieratos K. Soft-donor dipicolinamide derivatives for selective actinide(III)/lanthanide(III) separation: the role of S- vs. O-donor sites. *Chem. Commun*. **2019**, *55*, 2441-2444. (b). Ayme, J-F.; Gil-Ramirez, G.; Leigh, D. A.; Lemonnier, J-F.; Markevicius, A.; Muryn, C-A. and Zhang, G. Lanthanide Template Synthesis of a Molecular Trefoil Knot. *J. Am. Chem. Soc.* **2014**, *136*, 13142−13145.

19. Betts, R. and Dahlinger, O.F. The heat and entropy of association of the complex ions formed by EDTA with the lanthanide elements in aqueous solution. *Canadian Journal of Chemistry,* **1959**, *37*, 91-100.

20. Roughley, G. 2012, Lanthanide Ternary Complexes Relevant to the Nuclear Fuel Cycle, MS dissertation, University of Manchester, Manchester, England.

21. Mackey, J. L.; Powell, J. E. and Spedding, F. H. A Calorimetric Study of the Reaction of Rare-earth Ions with EDTA in Aqueous Solution, F.H. Spedding. *J. Am. Chem. Soc.* **1961**, *76*, 2047-2050.

22. Faas, G. C. and Mody, I. Measuring the kinetics of calcium binding proteins with flash photolysis. *Biochim. Biophys. Acta.* **2011,** *1820*, 1195-1204.

23. Escobar, A. L.; Velez, P.; Kim, A. M.; Cifuentes, F.; Fill, M. and Vergara, J. L. inetic properties of DM-nitrophen and calcium indicators: rapis transient response to flash photolysis. *Pflugers Arch.* **1997**, *434*, 615-631.

24. Ellis-Davies, G. C.; Kaplan, J. H.; Barsotti, R. J. Laser Photolysis of Caged Calcium: Rates of Calcium Release by Nitrophenyl-EGTA and DM-Nitrophen. *Biophys. J.* **1996**, *70*, 1006-1016.

25. Ayer, R. K.; Zucker, R. S. Magnesium binding to DM-nitrophen and its effect on the photorelease of calcium. *Biophys. J.* 1999, *77*, 3384-3393.

26. Borges dos Santos, R.M.; Lagoa, A. L. and Simoes, J. M. Photoacoustic calorimetry. An examination of a non-classical thermochemistry tool**.** *J. Chem. Thermodynamics*, **1999**, *31*, 1483–1510.

27. Larsen, R. W. and Mikšovská, J. Time resolved thermodynamics of ligand binding to heme proteins. *Coord. Chem. Rev.* **2007**, *251*, 1101-1127.

28. Gonzalez, W. G. 2016, Protein-Ligand Interactions and Allosteric Regulation of Activity in DREAM Protein, PhD Dissertation, Florida International University, Miami.

29. McCray, J. A.; Fidler-Lim, N.; Ellis-Davies, G. C. R. and Kaplan, J. H. Rate of release of calcium following laser photolysis of the DM-nitrophen-calcium complex. *Biochemistry*, 1992, *31*, 8856-8861.

30. Word, T.A. and Larsen, R. W. Photoacoustic calorimetry studies of CO photo-dissociation from chloramine-T modified horse heart cytochrome-c. *Arch. Biochem. Biophys.* **2016**, *612*, 17-21.

Chapter 4

Spectroscopic studies of Ln^{3+} binding to H_2cage

Setareh Sakhdari, Xinrui Zhang, Oluwaseun W. Adedoyin, Indranil Chakraborty,

Konstantinos Kavallieratos*

*Corresponding author

4.1. Abstract

Lanthanides can be used in biological studies because of their luminescence properties. Furthermore f-element binding and separation is of importance for treatment and recycling of used nuclear fuel and highly alkaline high-level waste. In this study, we used the known H_2cage ligand for Ln^{3+} complexation and extraction. The interaction of H_2cage with several Ln^{3+} was characterized by UV-Vis absorption. The 1:1 Ln^{3+}-H_2cage association constants were determined by non-linear regression analysis of UV-Vis titrations and fitting to the 1-1 binding isotherm and were found to be $K_{11} = 1900 \pm 130 \, M^{-1}$ for La^{3+}, $K_{11} = 1900 \pm 360 \, M^{-1}$ for Nd^{3+}, $K_{11} = 4900 \pm 725 \, M^{-1}$ for Sm^{3+}, $K_{11} = 2900 \pm 467 \, M^{-1}$ for Tb^{3+}, $K_{11} = 3200 \pm 690 \, M^{-1}$ for Dy^{3+}, and $K_{11} = 4900 \pm 1300 \, M^{-1}$ for Yb^{3+}. Distribution experiments in CH_2Cl_2/NaOH (pH = 11.5) and quantification of Ln^{3+} by ICP-MS in the aqueous phases demonstrated the ability of H_2cage to extract Ln^{3+}. The ICP-MS results of aqueous phases after contact with the H_2cage solution showed > 94% of La^{3+}, Nd^{3+}, Sm^{3+}, and Eu^{3+}, 82% of Tb^{3+}, 84% of Dy^{3+} and 99% of Yb^{3+}. Overall, this study demonstrates potential applicability of H_2cage ligand and its analogs for f-element binding and separation, which can be influential in nuclear separations.

4.2. Introduction

Lanthanides have many applications in scientific and technological fields due to their unique photophysical properties and their useful applications in the areas like cell imaging, optical amplification, light-emitting diodes, and luminescent probes.[1] Furthermore, Ln^{3+} separation by solvent extraction is critically important for nuclear applications, as many Ln^{3+} are fission products and Ln^{3+} are surrogates for important minor actinides, such as Am^{3+} and Cm^{3+}, which are of critical separation interest for nuclear technology.[1,2] Separation of Ln^{3+} from alkaline high-level waste is an area of increasing research interest, as Ln^{3+} are used as surrogates for actinides, for such applications.[3,4] Lewis et al. (2011) synthesized a phenanthroline-derived quadridentate bis-triazine ligand that could separate An^{3+} from Ln^{3+} from nitric acid solutions.[5] Grimes et al. (2014) used a modified TALSPEAK extraction method by using different amino acid buffers which demonstrated improved trivalent Ln^{3+}/An^{3+} separation.[6] Demir et al. (2016) employed an aqueous mixture containing porous carboxylic acid aromatic framework to separate Nd^{3+} from a mixture of trivalent actinides and transition metals.[7] Patil et al. (2014) showed that the synergistic mixture of N,N'-diethyl-N,N'-di(para) fluorophenyl-2,6-dipicolinamide and hydrogen dicarbollylcobaltate ligands can be employed to extract An^{3+}/Ln^{3+} with a decrease in extraction efficiency as a result of increased aqueous phase acidities.[8] Patterson et al. (2018) employed four tripodal carbamoyl methylphosphine oxide (CMPO)-based ligands for selective Ln^{3+} coordination and extraction and found that increasing hydrophobic groups result in low extraction efficiency of Ln^{3+} except for Gd^{3+} and Tb^{3+}.[9] Ln^{3+} are hard Lewis acids so they prefer hard donor atoms like oxygen. Therefore, the presence of oxygen in the ligand structure could enhance the stability of the Ln^{3+} complex,

such as in carboxylate-type ligands.[10-15] Several Ln^{3+} complexes have been reported that also contain nitrogen atoms in addition to oxygen in their structures, with nitrogen atoms typically being part of aromatic heterocyclic frameworks. Gao et al. (2018) employed a benzoic acid-functionalized polysulfone polymer for Ln^{3+} sensitization. By using a phenanthroline framework, they were able to enhance the luminescence in the Ln^{3+} complex.[15] Zhang et al. (2019) designed a Ln^{3+} complex containing 8-hydroxyquinoline moiety which exhibits red-shift in the C=N stretching frequency with concurrent disappearance of the OH stretching band in FT-IR, with both oxygen and nitrogen atoms coordinated to Ln^{3+}. The UV-Vis spectra for the Ln^{3+} complex also showed a band at 385 nm, which is indicative of enhanced spin-orbit coupling (π-π*) and spin-forbidden LMCT transitions.[10] Xu et al. (2011) synthesized a Ln^{3+} cage that incorporates the 2-hydroxyisophthalamide (IAM) moiety as both antenna chromophore and a chelating group displaying good thermodynamic stability in aqueous solution.[16] Metlin et al. (2017) employed a pyrazole/β-diketone-diketonate/unit phenanthroline ligand that can transfer energy to Ln^{3+}.[17] Tang et al. (2006) reported an aromatic 1,3,4-oxadiazole which shows red-shift for the C=O stretch in the FT-IR upon Ln^{3+} addition.[18] Fu et al. (2008) reported an aromatic carboxylic acid ligand, tethered to a phenanthroline or bi-pyridine moiety that shows enhanced luminescence upon Ln^{3+} binding.[19] Juan et al. (2006) synthesized Tb^{3+} and Eu^{3+} complexes containing carbazolyl-benzoic acid moiety which showed an enhanced luminescence that could be used in OLEDS with high luminescence efficiency.[20] Luo et al. (2009) employed a β-diketone ligand carrying heterocyclic aromatic rings that shows increased luminescence when combined with phenanthroline for Ln^{3+} complexation.[21] Lehman-Andino et al. (2019) synthesized a dipicolinamide ligand for Ln^{3+} complexation,

and compared the dithio vs the dioxo dipicolinamide derivatives for their ability to separate Am^{3+} from Ln^{3+}. According to the reported crystal structure, binding occurs via the amide C=O groups and the nitrogen of the central pyridine. Complexation was shown to be 1:1 in solution in the presence of nitrate, while a 3:1 ligand:Ln^{3+} ratio was observed in the presence of the more weakly coordinating iodide counteranion. Absorption spectra also showed an increase with a red shift of the absorbance at 282 nm upon Ln^{3+} addition.[22]

One of the benefits of the use of Ln^{3+} complexes is their use for sensing several ions that have biological or environmental roles, such as Fe^{2+},[23] Cu^{2+}[24] and phosphate.[25] The sensing occurs through change into the energy transfer from the chromophore to Ln^{3+} as a result of interaction with another molecule or ion that could effect on the whole structure of the complex. Rina et al. (2020) used a La^{3+}-based N,N-dimethylbenzylamine complex ($La(DMBA)_3$) as a precatalyst to synthesize biologically important organophosphorous compounds.[26] Ln^{3+} ions are also known as Ca^{2+} biomimetics and can be used to study the Ca^{2+} binding macromolecules such as EF-hand proteins.[27] Ca^{2+} does not have unpaired electrons and electronic transitions involving f-orbitals, making it difficult to be used in spectroscopic studies[28] while Ln^{3+} particularly Eu^{3+}[29] and Tb^{3+}[30] ions are often used for spectroscopic studies. In addition, the coordination numbers for Ca^{2+} and Ln^{3+} are often similar.[28] Some well-known cages that are used for studying structure and function of macromolecules are the ortho-nitrobenzyl cages.[31] These cages are photolyzable which is advantageous in that they can release their trapped species in a timely resolved process. DM-nitrophen, an EDTA-derivative nitrobenzyl cage, is a typical Ca^{2+} and Mg^{2+} cage that has been under study for analyzing the caging/uncaging of these divalent cations. H_2cage is another ortho-nitrobenzyl cage that is used by Ciesienski et al. (2008) to bind Cu^{2+}.[32]

Cu^{2+} has many roles such as having pro-oxidant activity that could be used for cancer therapy. In this chapter, we report the X-ray crystal structure of the H_2cage ligand, as well as its interaction with Ln^{3+} using absorption spectroscopy and extraction studies followed by quantification of Ln^{3+} in the aqueous phases by Inductively-Coupled Plasma Mass Spectrometry (ICP-MS). ICP-MS is a technique typically used to detect very small amounts of elements and is very practical for studying distribution in extraction for samples containing mixtures of metals. ICP-MS has been used to detect Ln^{3+}-tagged oligonucleotides,[33] and Ln amounts in biological tissues[34] or in environmental samples.[35,36] In this work, we used ICP-MS to quantify Ln^{3+} in the aqueous phase after extraction experiments and to determine extraction efficiencies for various Ln from alkaline solutions after contact with solutions of H_2cage. The remarkably high extraction efficiencies observed demonstrate the potential of H_2cage ligands and analogs for separation applications for f-elements including Ln^{3+} and potentially minor actinides.

4.3. Results and discussion

4.3.1 X-ray crystal structure of H₂cage

The crystal structure of the H_2cage obtained after slow evaporation of a methanol solution is shown in Figure 4.1. Inside the cage, there is a water molecule which exhibits a relatively weak non classical H-bonding interaction with one of the N-H groups ((D---A, 3.002(4) Å) and a moderately strong H-bonding interaction with one of the pyridine N atoms (D---A, 2.825(4) Å) with a bond angle of 170(2) Å.
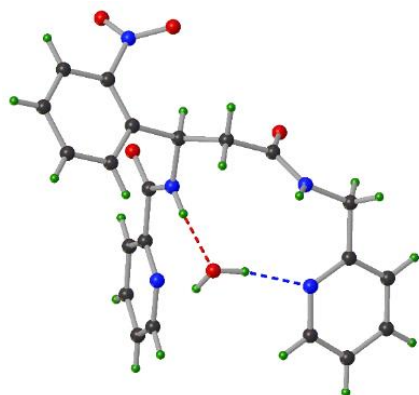
Figure 4.1. The crystal structure of H$_2$cage showing a water molecule H-bonded to an amide N-H and a pyridine N atom.

4.3.2 UV-Vis titrations

UV-Vis titrations of H$_2$cage with Ln(NO$_3$)$_3$.xH$_2$O (x = 5 or 6, depending on Ln) in CH$_3$CN provided evidence of complex formation with an observed increase in absorbance at 266 nm. The concentration of H$_2$cage was kept constant throughout the titration experiments, and only the concentration of Ln^{3+} salts varied. To ensure that the increase in absorbance was not due simply to spectroscopic changes resulting from addition of Ln^{3+} in CH$_3$CN, control experiments were carried out under identical conditions, in which Ln^{3+} salts were added to a solution that contained all components, except the H$_2$cage and the resulting spectra for the control experiments were subtracted to calculate the spectroscopic change resulting directly from interaction of Ln^{3+} with H$_2$cage. Figures 4.2 - 4.4 show the UV-Vis spectra upon titration of H$_2$cage with La(NO$_3$)$_3$.6H$_2$O, Yb(NO$_3$)$_3$.6H$_2$O, Dy(NO$_3$)$_3$.5H$_2$O, Tb(NO$_3$)$_3$.5H$_2$O, Nd(NO$_3$)$_3$.6H$_2$O and Sm(NO$_3$)$_3$.6H$_2$O under constant H$_2$cage concentration (3.0 × 10^{-5} M) and after baseline correction for the control titrations. All

binding constants were determined by non-linear regression analysis of the absorbance increase at 266 nm, and fitting to the 1-1 binding isotherm.[3,37]

(a)   (b)
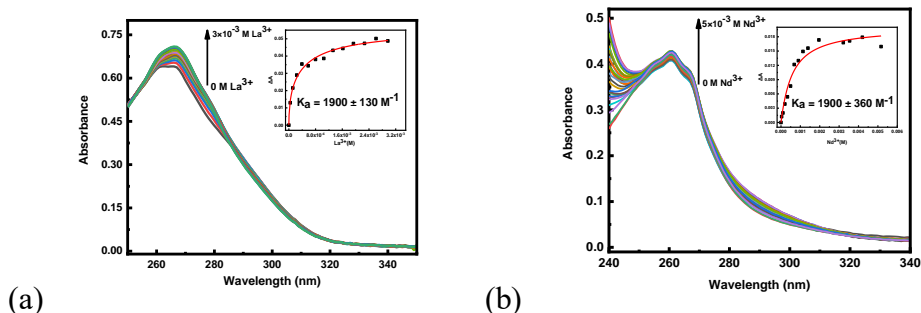
Figure 4.2. Titration of H_2cage (3.0×10^{-5} M) with La(NO$_3$)$_3$.6H$_2$O (a) in acetonitrile and Nd(NO$_3$)$_3$.6H$_2$O (b) in methanol. Binding constants shown were determined by non-linear regression analysis of the 1:1 binding isotherm.

(a)   (b)
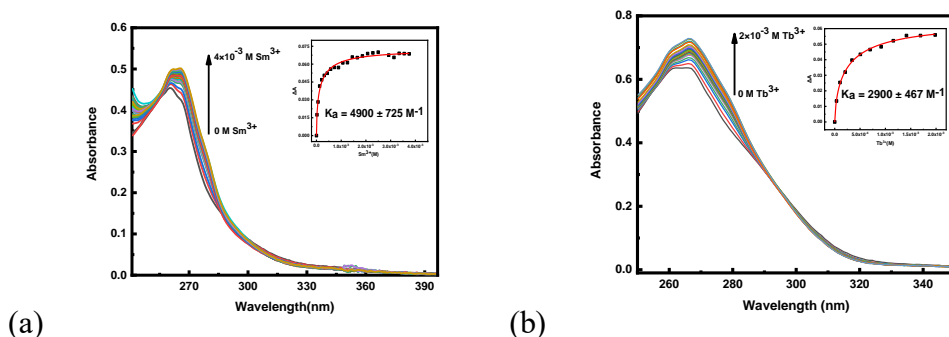
Figure 4.3. Titration of H_2cage (3.0×10^{-5} M) with Sm(NO$_3$)$_3$.6H$_2$O (a) and Tb(NO$_3$)$_3$.6H$_2$O (b) in acetonitrile. Binding constants shown were determined by non-linear regression analysis of the 1:1 binding isotherm.

(a)   (b)
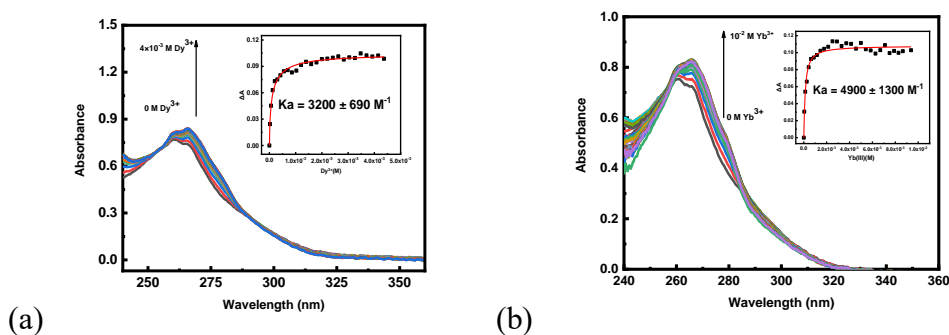
Figure 4.4. Titration of H_2cage (3.0×10^{-5} M) with Dy(NO$_3$)$_3$.5H$_2$O (a) and Yb(NO$_3$)$_3$.5H$_2$O (b) in acetonitrile. Binding constants shown were determined by non-linear regression analysis of the 1:1 binding isotherm.

93

The UV-Vis spectroscopic titrations of H_2cage with the six Ln^{3+} salts show only a slight trend of increasing binding constant across the Ln^{3+} series, with a notable exception for Sm^{3+} (Table 4.1). For other Ln^{3+}-binding ligands, it has been reported that binding constants generally increase, when moving from La^{3+} to Lu^{3+} across the Ln^{3+} series.[38,39] In our case, we did not observe any clear trend, yet the early lanthanides La^{3+} and Nd^{3+} show weaker binding constants compared to the later ones Dy^{3+} and Yb^{3+}.

Table 4.1. Binding constants for Ln^{3+}-H_2cage complex formation

	La^{3+}	Nd^{3+}	Sm^{3+}	Tb^{3+}	Dy^{3+}	Yb^{3+}
$K(M^{-1})$	1900 ± 130	1900 ± 360	4900 ± 725	2900 ± 467	3200 ± 690	4900 ± 1300

4.3.3. Extraction study

The extraction of Ln^{3+} from alkaline aqueous solutions (NaOH, pH = 11.5) into organic phases (H_2cage dissolved in CH_2Cl_2) was carried out. 0.2 mM aqueous solutions of seven Ln^{3+}: Eu^{3+}, Sm^{3+}, Nd^{3+}, La^{3+}, Dy^{3+}, Yb^{3+} and Tb^{3+} were contacted with 2 mM H_2cage solutions in CH_2Cl_2, both with and without the presence of triethylamine (4 mM). After 20 hours of contact the phases were separated, and the aqueous phases were subsampled and analyzed by ICP-MS for Ln^{3+} content both before and after contact with the organic phase.

As shown in Table 4.2, > 94% of La^{3+}, Nd^{3+}, Sm^{3+}, and Eu^{3+}, 82% of Tb^{3+}, 84% of Dy^{3+} and 99% of Yb^{3+} were extracted into the organic phase by H_2cage while the presence of organic base did not seem to have a significant effect. Figure 4.5 shows a graphic representation of Ln^{3+} extraction efficiencies both with and without the presence of Et_3N. These results are consistent with prior work from our group[3] and demonstrate the potential of the H_2cage family of compounds for f-element separation from alkaline solutions.

Table 4.2. Ln^{3+} % Extraction for each Ln^{3+} by H_2cage (2 mM)

Extraction percentage %		
	With Et$_3$N (4 mM)	Without Et$_3$N
La	96.0	95.4
Nd	98.1 ± 1.7	97.5 ± 2.1
Sm	97.2 ± 2.7	97.0 ± 2.4
Eu	95.7	96.0
Tb	86.0	82.2
Dy	84.5 ± 15.4	88.0 ± 12.0
Yb	99.5 ± 0.3	99.5 ± 0.3
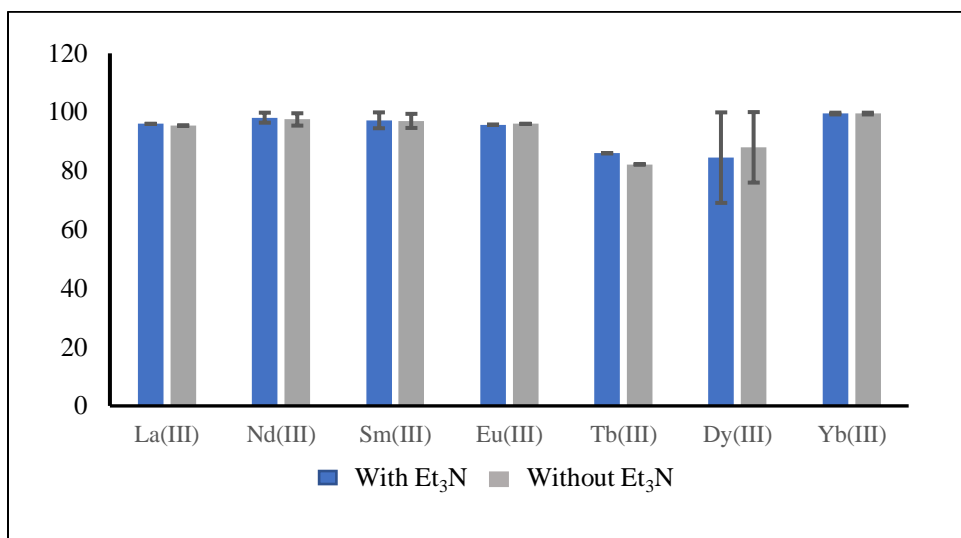
Figure 4.5. Graphic representation of % Ln^{3+} extraction by H_2cage (2 mM) with base (Et$_3$N - 4 mM) and without base.

4.4. Conclusions

The H_2cage ligand has shown remarkably high extraction efficiencies for several Ln^{3+} in modestly alkaline conditions, which compare favorably with prior results with sulfonamide ligands by Govor et al.[3] and present possible applicability of this type of ligands for separation of f-elements from alkaline high-level waste. UV-Vis spectroscopic titrations in acetonitrile displayed relatively modest binding affinities for H_2cage to Ln^{3+} and 1:1 complexation. As we did not use alkaline environment for deprotonation of amide groups

during the titrations in acetonitrile, it is presumed that binding to Ln^{3+} in CH_3CN involves mainly the C=O functional groups and the pyridine N and does not involve deprotonation of the N-H groups. These results are consistent with previous results from Lehman et al. (2018) and our work with dipicolinamides (See Chapter 2), which show that Ln^{3+} mainly binds to the amide C=O, as well as the pyridine nitrogen.[32]

4.5. Experimental section

4.5.1 Materials and methods

$Ln(NO_3)_3.6H_2O$ and $Ln(NO_3)_3.5H_2O$ salts were obtained from Fisher Scientific (> 99.9% purity). Spectroscopic grade high-purity (>99.8%) solvents, including acetonitrile was used for UV-Vis titrations. UV-Vis spectra were recorded on a Varian Cary 100 Bio UV-Visible spectrometer. ^{1}H- and ^{13}C-NMR spectra were recorded on a 400 MHz Bruker NMR spectrometer and were referenced using the residual solvent resonances. All chemical shifts, δ, are reported in ppm. The ligand H_2cage is obtained in a one-pot, two-step synthesis according to previously published literature and was found spectroscopically identical to the reported compound.[32]

4.5.2. Synthesis and X-ray crystallography of pyridine-2-carboxylic acid {1-(2-nitro-phenyl)-2-[(pyridine-2-ylmethyl)-carbamoyl]-ethyl}-amide (H2cage).

The H_2cage ligand was synthesized according to the previously reported procedure starting from 3-amino-3-(2-nitrophenyl) propionic acid.[32] For X-ray crystallography the H_2cage ligand (30 mg) was dissolved in methanol (1 mL) and the yellowish crystals were obtained through slow evaporation of the solvent. X-ray structure determination details are summarized in Table 4.3. Data were collected on a Bruker D8 Quest single crystal X-

ray diffractometer (PHOTON 100 CMOS detector) with graphite monochromated Mo Kα radiation (λ = 0.71073 Å) by the ω-scan technique in the range 6.2≤ 2θ ≤ 50.5 for H_2cage. All data were corrected for Lorentz and polarization effects.[40] All the structures were solved with the aid of *SHELXT* program using intrinsic phasing.[41] The structures were then refined by a full-matrix least squares procedure on F by *SHELXL*.[42] All non-hydrogen atoms were refined anisotropically. Hydrogen atom positions were calculated geometrically and refined using the riding model. Multi-scan absorption corrections are applied using SADABS2. Calculations were performed using the OLEX2[43] and SHELXTL™[44] program packages.

Table 4.3. Experimental details for X-ray structure determination.

Crystal Data	
Chemical formula	$H_2O.C_{21}H_{19}N_5O_4$
Mr	423.43
Crystal system, space group	Triclinic, $P1$
Temperature (K)	296
A, b, c (Å)	7.4175 (3), 10.5727 (5), 13.9830 (6)
α, β, γ (°)	101.727 (1), 103.576 (1), 94.547 (1)
V (Å^3)	1034.37 (8)
Z	2
Radiation type	Mo Kα
μ (mm^{-1})	0.10
Crystal size (mm)	$0.15 \times 0.10 \times 0.06$
Data collection	
Diffractometer	Bruker D8 Quest CMOS
Absorption correction	Multi scan SADABS 2016/2
T_{min}, T_{max}	0.711, 0.745
No. of measured, independent and observed [I>2σ(I)] reflections	19586, 4164, 2817
R_{int}	0.030
$(\sin \theta/\lambda)_{max}$ (Å^{-1})	0.626
Refinement	
R[$F^2 > 2\sigma(F^2)$], wR(F^2), S0.049, 0.125, 1.03	
No. of reflections	4164
No. of parameters	288
H-atom treatment	H atoms treated by a mixture of independent and constrained refinement
$\Delta\rho_{max}$, $\Delta\rho_{min}$ (e Å^{-3})	0.26, -0.22

4.5.3. UV-Vis titrations

UV-Vis titrations were performed with solutions of H_2cage in acetonitrile titrated with solutions of $Eu(NO_3)_3 \cdot 6H_2O$, $Nd(NO_3)_3 \cdot 6H_2O$, $Dy(NO_3)_3 \cdot 5H_2O$, $Yb(NO_3)_3 \cdot 5H_2O$, $Tb(NO_3)_3 \cdot 6H_2O$ and $Sm(NO_3)_3.6H_2O$ at constant ligand concentration. In a typical experiment, a solution of H_2cage $(3.0 \times 10^{-5}$ M) was titrated with a solution of $Ln(NO_3)_3 \cdot 6H_2O$ or $Ln(NO_3)_3.5H_2O$ $(1.0 \times 10^{-2}$ M) and H_2cage $(3.0 \times 10^{-5}$ M), prepared by accurately weighing approximately 44 mg of $Ln(NO_3)_3 \cdot xH_2O$ (x = 5 or 6) in a 10.0 mL volumetric flask and diluting with the solution of the ligand. For spectra collection, 2.20 mL of H_2cage solution was added to the UV-Vis cuvette and the lanthanide solution was added in 10-200 µL increments until a total of 2.0 mL had been added.

4.5.4. Extraction experiments and analysis

The extraction experiments were carried out in 15 mL glass tubes at a 1:1 organic:aqueous phase volume ratio. The organic phase in one set of tubes contained a solution of 2.0 mM H_2cage in CH_2Cl_2 while in the second set of tubes, it contained a solution of 2.0 mM H_2cage and 4.0 mM Et_3N. The aqueous phases were $Ln(NO_3)_3 \cdot xH_2O$ (0.2 mM) (x = 5 or 6) in sodium hydroxide at pH 11.5. The solutions were put inside seven stoppered glass tubes each containing 2.0 mL of aqueous phase of each of the seven Ln^{3+} ion with 2.0 mL of the organic phase containing the ligand with or without Et_3N. The solutions were mixed in the glass tube and rotated on a wheel (55 rpm, 20 h) at room temperature. The extraction efficiency was calculated based on equation 1:

$$E\% = \frac{[Ln]_{(initial)} - [Ln]_{(after\ extraction)}}{[Ln]_{(initial)}} \times 100 \qquad \text{Eq. 1}$$

Acknowledgements

References

1. Leoncini, A.; Huskens, J. and Verboom, W. Ligands for f-element extraction used in the nuclear fuel cycle. *Chem. Soc. Rev*. **2017**, *46*, 7229-7273.

2. Gorden, A. E. V.; DeVore , I, M. A. and Maynard, B. A. Coordination Chemistry with f-element Complexes for an Improved Understanding of Factors That Contribute to Extraction Selectivity. *Inorg. Chem*. **2013**, *52*, 3445-3458.

3. Govor, E. V.; Morozov, A. N.; Rains, A. A.; Mebel, A. M. and Kavallieratos, K. Spectroscopic and Theoretical Insights into Surprisingly Effective Sm(III) Extraction from Alkaline Aqueous Media by *o*-Phenylenediamine-Derived Sulfonamides, *Inorg. Chem*. **2020**, *59*, 6884-6894.

4. Morozov, A. N.; Govor, E. V.; Anagnostopoulos, V. A.; Kavallieratos, K. and Mebel, A. M. 1,3,5-Tris-(4-(iso-propyl)-phenylsulfamoylmethyl)benzene as a potential Am(III) extractant: experimental and theoretical study of Sm(III) complexation and extraction and theoretical correlation with Am(III). *Mol. Phys*. **2018**, *116*, 2719-2727.

5. Lewis, F. W.; Harwood, L. M.; Hudson, M.; Drew, M. G. B.; Desreux, J. F.; Vidick, G.; Bouslimani, N.; Modolo, G.; Wilden, A.; Sypula, M.; Vu, T-H. and Simonin, J-P. Highly Efficient Separation of Actinides from Lanthanides by a Phenanthroline-Derived Bis-triazine Ligand. *J. Am. Chem. Soc*. **2011**, *133*, 13093-13102.

6. Grimes, T. S.; Tillotson, R. D. and Martin, L. R. Trivalent Lanthanide/Actinide Separation using aqueous-modified TALSPEAK chemistry. *Solvent Extraction and Ion Exchange*, **2014**, *32*, 378-390.

7. Demir, S.; Brune, N. K.; Van Humbeck, J. F.; Mason, J. A.; Plakhova, T. V.; Wang, S.; Tian, G.; Minasian, S. G.; Tyliszczak, T.; Yaita, T.; Kobayashi, T.; Kalmykov, S. N.; Shiwaku, H.; Shuh, D. K. and Long, J. R. Extraction of Lanthanide Using a Carboxylic Acid-Functionalized Porous Aromatic Framework. *ACS Cent. Sci*. **2016**, *2*, 253-265.

8. Patil, A.B.; Pathak, P.; Shinde, V. S.; Alyapyshev. M. Y.; Babain, V. A. and Mohapatra, P. K. A novel dipicolinamide-dicarbollide synergistic solvent system for actinide extraction. *Radiochim. Acta.* **2014**, *102*, 481-487.

9. Patterson, M. G.; Mulville, A. K.; Connor, E. K.; Henry, A. T.; Hudson, M. L.; Tissue, K.; Biros, S. M. and Werner, E. J. Lanthanide extraction selectivity of a tripodal carbamoylmethylphosphine oxide ligand system. *Dalton Trans*. **2018**, *47*, 14318-14325.

10. Zhang, Q.; Yang, X.; Deng, R.; Zhou, L.; Yu, Y. and Li, Y. Synthesis and Near Infrared Luminescence Properties of a Series of Lanthanide Complexes with POSS Modified Ligands. *Molecules,* **2019**, *24*, 1253-1261.

11. Kolokolov, F. A.; Kulyasov, A. N.; Magomadova, M. A.; Shapieva, Kh. K.; Mikhailov, I. E.; G. A. Dushenko, G. A. and Panyushkin*,* V. A. Synthesis and Luminescent Properties of Coordination Compounds of Europium(III), Gadolinium(III), and Terbium(III) with *para*-Alkyloxybenzoic Acids. *Russ. J. Gen. Chem.* **2016**, *86*, 1209-1211.

12. Naiqun Sun, N.; Li, L.; Yang, Y.; Zhang, A.; Jia, H.; Liu, X. and Xu, B. Synthesis, Characteristics and Luminescent Properties of a New Tb(III) Ternary Complex Applied in Near UV-based LED. *Optical Materials,* **2015**, *49*, 39-45.

13. Zhu, Y.; Shu, G.; Yang, Y.; Dong, Q. and Zou, L. Synthesis and electrochemiluminescence properties of a new ternary terbium complex and its application for the determination of norfloxacin. *J. Electroanal. Chem.* **2014**, *727*, 113-119.

14. Dai, M.; Xiao, H.; Ye, C.; Shu, D.; Shi, L. and Guo, D. Synthesis and Luminescence Properties of Terbium Complexes Based on 4- acyl Pyrazolone Derivatives. *J. Lumin.* **2017.** *188*, 223- 229.

15. Gao, B.; Chen, L. and Chen, T. Effect of Electron-Donating Substituent Groups on Aromatic Ring on Photoluminescence Properties of Complexes of Benzoic Acid-Functionalized Polysulfone with Eu(III) Ions. *Phys.Chem.Chem.Phys.,* **2015**, *17*, 25322-25332.

16. Xu, J.; Todd, M.; Corneillie, E. G.; Moore, G-L L.; G. Butlin, N. G and Raymond, K. N. Octadentate Cages of Tb(III) 2-Hydroxyisophthalamides: A New Standard for Luminescent Lanthanide Labels. *J. Am. Chem. Soc.* **2011**, *133*, 19900–19910.

17. Metlin, M. T.; Ambrozevicha, S. A.; Metlina, D.A.; Vitukhnovsky, A.G. and Taydakov, I.V. Luminescence of Pyrazolic 1,3-diketone Pr^{3+} Complex with 1,10-Phenanthroline. *J. Lumin.* **2017**, *188*, 365-370.

18. Tang, X-L.; Dou, W.; Chen, S-W.; Dang, F-F. and Liu, W-S. Synthesis, Infrared and Fluorescence Spectra of Lanthanide Complexes with a New Amide-Based 1,3,4-Oxadiazole Derivative. *Spectrochim. Acta A*. **2007**, *68*, 349-353.

19. Fu, Y.; Zhang, J.; Huang, Z.; Wang, X.; Lu, Y. and Cao, W. Study of the Effect of Ligands on the Fluorescence Properties of Terbium Ternary Complexes. *J. Photochem. Photobio. A*. **2008**, *197*, 329-334.

20. Juan, P.; Xiaotian, G.; Jianbo, Y.; Yanhui, Z.; Ying, Z.; Yunyou, W. and Boa, S. Synthesis and Fluorescence Studies on Novel Complexes of Tb(III) and Eu(III) with 4-(9*H*-carbazol-9-yl) Benzoic acid. *J. Alloys Compd*. **2006**, *426*, 363-367.

21. Luo, Y-M.; Li, J.; Xiao, L-X.; Tang, R-R. and Tang, X-C. Synthesis, Characterization and Fluorescence Properties of Eu(III) and Tb(III) Complexes with Novel Mono-Substituted β-diketone Ligands and 1,10-phenanthroline. *Spectrochim. Act. A*. **2009**, *72*, 703-708.

22. Lehman-Andino, I.; Su, J.; Papathanasiou, K. E.; Eaton, T. M.; Jian, J.; Dan, D.; Albrecht-Schmitt, T. E.; Dares, C. J.; Batista, E. R.; Yang, P.; Gibson, J. K. and Kavallieratos, K. Soft-donor dipicolinamide derivatives for selective actinide(III)/lanthanide(III) separation: the role of S- vs. O-donor sites. *Chem. Commun.* **2019**, *55*, 2441-2444.

23. Song, X-Z.; Wang, Y-X.; Yan, J-W.; Chen, X.; Meng, Y-L. and Tan, Z. Enhancing the Fe^{3+} Sensing Sensitivity by Energy Transfer and Phase Transformation in a Bimetallic Lanthanide Metal-Organic Framework. *ChemistrySelect*, **2018**, *3,* 9564-9570.

24. McMahon, B. K. and Gunnlaugsson, T. Lanthanide Luminescence Sensing of Copper and Mercury Ions Using an Iminodiacetate-based Tb(III)-Cyclen Chemosensor. *Tetrahedron Lett.* **2010**, *51*, 5406-5410.

25. Andonilina, C. M. and Morrow, J. R. Luminescence Resonance Energy Transfer in Heterodinuclear LnIII Complexes for Sensing Biologically Relevant Anions. *Eur. J. Inorg. Chem.* **2011**, 154–164.

26. Rina, Y. A. and Schmidt, J. A. R. Double Hydrophosphorylation of Nitriles Catalyzed by Rare-Earth-Metal Lanthanum. *J. Org. Chem.* **2020**, *85*, 14720-14729.

27. Drobot, B.; Schmidt, M.; Mochizuki, Y.; Abe, T.; Okuwaki, K.; Brulfert, F.; Falke, S.; Samsonov, S.A.; Komeiji, Y.; Betzel, C.; Stumpf, T.; Raff, J. and Tsushima, S. Cm^{3+}/Eu^{3+} induced structural, mechanistic and functional implications for calmodulin. *Phys.Chem.Chem.Phys.,* **2019**, *21*, 21213-21222.

28. Brittain, H. G.; Richardson, F. S. and Martin, R. B. Terbium(III) Emission as a Probe of Calcium(II) Binding Sites in Proteins. *J. Am. Chem. Soc.* **1976**, 8255-8260.

29. Hofmann, T.; Eng, S.; Lilja, H.; Drakenberg, T.; Vogel, H. J. and Forsen, S. Site-site interactions in EF-hand calcium-binding proteins. *Eur. J. Biochem.* **1988**, *172*, 307-313.

30. de Jersey, J. and Martin, R. B. Lanthanide Probes in Biological Systems: The Calcium Binding Site of Pancreatic Elastase As Studied by Terbium Luminescence. *Biochemistry*, **1980**, *19*, 1127-1132.

31. Kaplan, J. H. and Ellis-Davies, G. C. R. Photolabile chelators for the rapid photorelease of divalent cations. *Proc. Nad. Acad. Sci.* **1988**, *85*, 6571-6575.

32. Ciesienski, K. L.; Haas, K. L. Dickens, M. G.; Tesema, Y. T. and Franz, K. J. A Photolabile Ligand for Light-Activated Release of Caged Copper. *J. Am. Chem. Soc.* **2008**, *130*, 12246–12247.

33. Brükner, K.; Schwarz, K.; Beck, S. and Linscheid, M. W. DNA Quantification via ICP-MS Using Lanthanide-Labeled Probes and Ligation-Mediated Amplification. *Anal. Chem.* **2014**, *86*, 585-591.

34. Malik, A. K.; Pozebon, D.; Dressler, V. L.; Zority, M. and Becker, J. S. Methodologies for the Determination of Low Concentrations of Lanthanides in Biological Samples by ICP-MS. *At. Spectrosc.* **2007**, *28*, 123-128.

35. de Bang, T. and Husted, S. Lanthanide elements as labels for multiplexed and targeted analysis of proteins, DNA and RNA using inductively-coupled plasma mass spectrometry. *Trends Analyt. Chem.* **2015**, *72*, 45-52.

36. Bentlin, F. R. S. and Pozebon, D. Direct Determination of Lanthanides in Environmental Samples using Ultrasonic Nebulization and ICP OES. *J. Braz. Chem. Soc.* **2010**, *21*, 627-634.

37. Connors, K. A. Binding constants – the measurement of molecular complex stability. John Wiley & Sons, New York, Chichester, Brisbane, Toronto, Singapore 1987.

38. Hatanaka, T.; Kikkawa, N.; Matsugami, A.; Hosokawa, Y.; Hayashi, F. and Ishida, N. The origins of binding specificity of a lanthanide ion binding peptide, *Scientific Reports*, **2020**, *10*, 1-10.

39. Tircsó, G.; Kovács, Z. and Sherry, D. Equilibrium and Formation/Dissociation Kinetics of some Lanthanide(III)-PCTA complexes. *Inorg. Chem.* **2006**, *45*, 9269-9280.

40. North, A. C. T.; Phillips, D. C.; Mathews, F. S. A Semi-empirical Method of Absorption Correction. *Acta Crystallogr. Sect. A*. **1968,** *24*, 351–359.

41. Sheldrick, G. M. Crystal Structure Refinement with SHELXL. *Acta Crystallogr. Sect. C Struct. Chem.* **2015**, *71*, 3–8.

42. Sheldrick, G. M. SHELXT - Integrated Space-Group and Crystal-Structure Determination. *Acta Crystallogr. Sect. A*. **2015,** *71*, 3–8.

43. Dolomanov, O. V.; Bourhis, L. J.; Gildea, R. J.; Howard, J. A. K.; Puschmann, H. OLEX2: A Complete Structure Solution, Refinement and Analysis Program. *J. Appl. Crystallogr.* **2009**, *42*, 339–341.

44. Sheldrick, G. M. SHELXTL TM (V 6.14). Bruker Analytical X-ray Systems: Madison, WI 2000.

<div align="center">

Chapter 5.

Characterizing Ln^{3+}DREAM interaction using fluorescence spectroscopy and lifetime measurements

</div>

<div align="center">

Setareh Sakhdari, Maria Santiago, Jaroslava Miksovska*

</div>

*Corresponding author

5.1. Abstract

The Downstream Regulatory Antagonist Modulator (DREAM) is an EF-hand Ca^{2+}-binding protein that is expressed in brain and belongs to neuronal Ca^{2+} binding proteins. This multifunctional protein has been implicated in memory, learning and pain sensing as well as severe neuropathologies including Alzheimer and Huntington diseases. DREAM interactions with intracellular partners are regulated by Ca^{2+} binding of the EF-hands located in the C-terminal domain of the protein. Recently, it has been shown that EF-hands in DREAM are not Ca^{2+} specific and can bind other cations with an affinity that exceeds the affinity for its physiological ligand. In this study, we address interactions of EF-hands in DREAM with several Ln^{3+}. Since Ca^{2+} does not possess enhanced spectroscopic properties, Ln^{3+} have been used previously as Ca^{2+} biomimetics to study the Ca^{2+} binding protein. Here, we used fluorescence emission and lifetime measurements to study Ln^{3+} binding to DREAM and DREAM C- terminal domain and determine the impact of Ln^{3+} association on DREAM conformation. Values for the dissociation constants for Ln^{3+} binding to DREAM(Δ64) from Trp quenching were experimentally measured to be 119 ± 2 nM for Eu^{3+}, 202 ± 3 nM for Nd^{3+}, 468 ± 1 nM for Er^{3+}, 348 ± 40 nM for Dy^{3+}, 890 ± 20 nM for Sm^{3+}. Values for the dissociation constants for Ln^{3+} binding to DREAM(Δ160) from Trp quenching were determined to be 176 ± 3 nM for Eu^{3+}, 192 ± 4 nM for Nd^{3+}, 225

± 4 nM for Er^{3+}, 1126 ± 40 nM for Dy^{3+} and 790 ± 53 nM for Sm^{3+}. Lifetime measurements for Ln^{3+} binding to CaM using first-order exponential decay were determined as τ_1 of 155 ± 0.3 μs for Eu^{3+}CaM; τ_1 of 133 ± 0.8 μs for Nd^{3+}CaM; τ_1 of 101 ± 0.5 μs for Er^{3+}CaM; τ_1 of 132 ± 0.4 μs for Dy^{3+}CaM and τ_1 of 141 ± 0.3 μs for Sm^{3+}CaM. Lifetime measurements for Ln^{3+} binding to DREAM(Δ64) were determined as τ_1 of 178 ± 2 μs for Eu^{3+}DREAM(Δ64); τ_1 of 135 ± 0.1 μs for Nd^{3+}DREAM(Δ64); τ_1 of 139 ± 0.3 μs for Er^{3+}DREAM(Δ64); τ_1 of 138 ± 0.1 μs for Dy^{3+}DREAM(Δ64) and τ_1 of 112 ± 0.5 μs for Sm^{3+}DREAM(Δ64). Lifetime measurements for Ln^{3+} binding to DREAM(Δ160) were determined as τ_1 of 170 ± 0.5 μs for Eu^{3+}DREAM(Δ160); τ_1 of 149 ± 0.3 μs for Nd^{3+}DREAM(Δ160); τ_1 of 166 ± 0.9 μs for Er^{3+}DREAM (Δ160); τ_1 of 168 ± 0.7 μs for Dy^{3+}DREAM(Δ160) and τ_1 of 237 ± 1 μs for Sm^{3+}DREAM(Δ160). The luminescence decay of Trp in Eu^{3+}DREAM(Δ64) shows that Trp quenches faster in the presence of Eu^{3+} than in the presence of Ca^{2+}. Luminescence decay of 1,8-ANS:DREAM(Δ64) in the presence of Eu^{3+}, Er^{3+} and Yb^{3+} showed a reduced lifetime in the presence of Yb^{3+}. Far UV circular dichroism for analysis of the secondary structure showed that Eu^{3+} binding causes the structural changes of DREAM similar to Ca^{2+} binding and the titration experiments using hydrophobic probe 1,8-ANS show that these Ln^{3+} cause the rearrangement of the protein and ultimately the exposure of the hydrophobic surface of the protein, similar to Ca^{2+}, that controls the ligand binding. All these data confirm that these five Ln^{3+} could bring structural changes to DREAM.

5.2. Introduction

DREAM (downstream regulatory element antagonist modulator), also known as KChIP-3 (K^+ channel interacting protein-3) and calsenilin, is a member of structurally and

functionally related protein family known as neuronal calcium sensors that belong to EF-hand protein superfamily. As other NCS, DREAM is predominantly expressed in brain and is responsible for Ca^{2+} sensing. DREAM acts as a Ca^{2+}-dependent transcriptional receptor and transcription factor interacting with DNA at downstream regulatory element (DRE) sequences.[1] DREAM also interacts with Kv_4 potassium channels and binds to presenilin, blocks the release of Ca^{2+} from endoplasmic reticulum and causes the apoptosis of presenilin mutants associated with Alzheimer's disease.[2,3]

DREAM association to carboxyl-terminal portion of presenilin 1 and 2 was proposed to modulate presenilin enzymatic activity. DREAM is also an integral subunit component of Kv4 channels and its presence is necessary for Kv4 channel transport into the membrane as well as regulation of Kv4 channel kinetics.[4] As other NCS proteins, DREAM has four EF-hand motifs of which EF-hand 3 and EF-hand 4 have high affinity to Ca^{2+} with K_d in the range of 10^{-6} to 10^{-7} M while EF-hand 1 and possibly EF-hand 2 have poor affinity for Ca^{2+}. DREAM also binds to Mg^{2+} at EF-hand 2.

Ln^{3+}, also known as rare earth metals have paramagnetic properties that make them suitable probes for NMR studies. Due to their photo-physical properties including long fluorescence lifetimes (micro to millisecond timescale), Ln^{3+} are suitable external probes for fluorescent studies. Similar ionic radii, and comparable coordination chemistry between Ca^{2+} and Ln^{3+}, and the preference of Ln^{3+} (being hard Lewis acids) for oxygen coordination sites, make Ln^{3+} excellent biomimetics for Ca^{2+}.[5]

Several studies have investigated the interaction of Ln^{3+} with Ca^{2+} binding proteins.[6-10] Pidcock et al. (2001) found similarity of Ca^{2+} coordination number to Ln^{3+} and reported that any variation in coordination numbers, such as hydrogen bonding could be as the result

of additional positive charge density in Ln^{3+}.[8] The Tb^{3+} displacement of Ca^{2+} has been shown by Snyder et al. (1989) on the substitution of Ca^{2+} by Tb^{3+} in Ca^{2+} binding sites of *E. coli* receptors for simple sugars, which are both structurally related to the eukaryotic EF-hand Ca^{2+} sites, facilitating the use of Tb^{3+} phosphorescence assay for structural and functional studies of Ca^{2+} binding sites.[9] Furie et al. (1976) also found that Gd(III) displaces and mimics Ca^{2+} in thrombin generation.[10] Brayshaw et al. (2019) found that Tb^{3+} binds cadherin and replaces Ca^{2+} at Ca^{2+}-binding sites that could be observed with an increase in Tb^{3+} emission at 542 nm.[11] Edington et al. (2017) found that binding of Ln^{3+} to calmodulin (CaM) considerably changes the conformation of CaM binding sites and results in more compact configuration of Ln^{3+}CaM complex.[12] Drobot et al. (2019) found Eu^{3+}CaM has higher stability compared to Ca^{2+}CaM and can interfere with natural function of CaM.[13] Chaudhuri et al. (1997) found longer fluorescence lifetime of Tb^{3+} and Eu^{3+} in the presence of EF-hand protein S100β and the two Ln^{3+} show higher affinity constants for EF-hand II of the protein.[14] Gonzalez et al. (2016) carried out experiments on CaM and DREAM and found that the tyrosine fluorescence emission in CaM increases in the presence of both Ca^{2+} and Tb^{3+} while the tryptophan fluorescence in DREAM decreases in the presence of both Ca^{2+} and Tb^{3+} suggesting that Tb^{3+} induces structural changes in the EF-hand loop that are similar to those in the presence of Ca^{2+}. In addition, it was found that Tb^{3+} emission was enhanced in the presence of CaM and DREAM. Herein, we continued the previous study by Gonzalez et al. (2016) by characterizing interactions of DREAM with other Ln^{3+} (Eu^{3+}, Nd^{3+}, Er^{3+}, Dy^{3+}, Sm^{3+} and Yb^{3+}) to determine the affinity of DREAM for various Ln^{3+} ions as well as impact of the Ln^{3+} binding on protein structure and conformation. The results presented here will provide a better understanding of EF-hand protein interactions

with Ln^{3+}, as well as the impact of Ln^{3+} association on structural and functional properties of DREAM and neuronal calcium sensors in general.

5.3. Results

The biomimetic behavior of Ln^{3+} provides the opportunity to characterize the metal binding to Ca^{2+}-binding EF-hand proteins due to the excellent spectroscopic properties of Ln^{3+} protein complex. A previous study has shown that Tb^{3+} binds DREAM and NCS1.[1,20] Herein, we examined five Ln^{3+} in terms of binding to two EF-hand DREAM constructs: DREAM ($\Delta64$) and DREAM($\Delta160$), as well as CaM and their impact on the protein structure. DREAM($\Delta64$) constructs include residues 55 to 256 and carry all four EF hands whereas DREAM (160) construct represents the C- terminal domain of this protein with two Ca^{2+} binding EF-hands, EF-hand 3 and EF-hand 4. We also, analyzed the binding affinity of Ln^{3+} to DREAM constructs in the presence of hydrophobic probe 1,8-ANS. Figure 5.1 shows the structures of DREAM($\Delta64$)/($\Delta160$), CaM and the possible DREAM binding sites for 1,8-ANS.
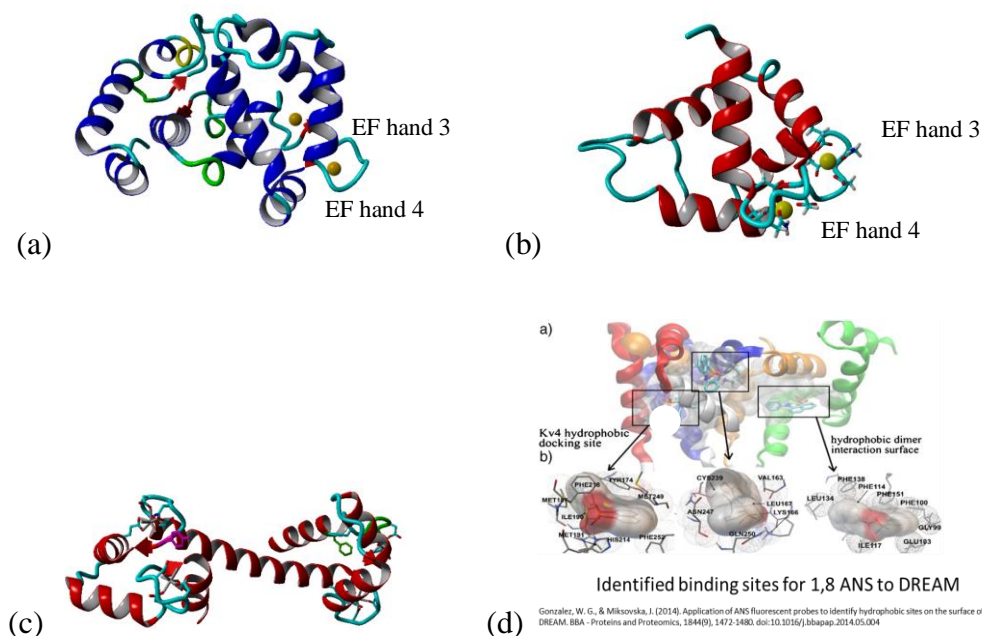
Figure 5.1. (a) DREAM(Δ64) (b) DREAM(Δ160) (c) CaM (d) Identified binding sites for 1,8-ANS to DREAM[22]

5.3.1. Quenching of tryptophan emission from Ln^{3+} binding to DREAM

The association of physiological ligands Ca^{2+} and Mg^{2+} to EF hand proteins is commonly associated with the modification of photo-physical properties of intrinsic fluorescent probes such as tyrosine (Tyr) and tryptophan (Trp) residues due to the structural reorganization of the protein. For example, Ca^{2+} association to CaM leads to the increase in the Tyr fluorescence quantum yield whereas Ca^{2+} association to DREAM results into more efficient quenching of the Trp residue. The impact of Ln^{3+} binding to EF-hands is more complex as in addition to the conformational changes in protein structure that modulate emission intensity of the protein, Ln^{3+} binding to DREAM may also result in Förster resonance energy transfer (FRET) from nearby aromatic residues to Ln^{3+}, resulting in efficient quenching of the internal fluorophore emission. The emission spectra of

DREAM(Δ64) and DREAM(Δ160) in the presence of EDTA, Ca^{2+} and Ln^{3+} are shown in Figure 5.2. The association of the physiological ligand, Ca^{2+} to both proteins leads to a more efficient quenching of Trp 169 emission as evident from the decrease in the emission intensity at 330 nm for Ca^{2+} bound samples. Addition of Ln^{3+} ions studied here leads to a more efficient quenching in Trp emission in both DREAM constructs. Interestingly, more efficient quenching observed here for Eu^{3+}DREAM(Δ160) indicates distinct conformation of Eu^{3+}DREAM(Δ160) compared to Ca^{2+}DREAM(Δ160) or the decrease in the Trp emission can be associated with the more efficient energy transfer between excited Trp residues and Eu^{3+} bound to the protein EF-hands. Interestingly, the association of Nd^{3+}, Er^{3+}, Dy^{3+} and Sm^{3+} to DREAM lead to a decrease in the Trp emission intensity compared to the apoprotein. However, the Trp emission quenching is somewhat less efficient than in the case of Eu^{3+} bound DREAM but more efficient than in the case of Ca^{2+} bound DREAM. This can be attributed either to absence of the structural transition upon Nd^{3+}, Er^{3+}, Dy^{3+} and Sm^{3+} binding to the protein or to the less efficient energy transfer between the Trp side chains and the Ln^{3+}. The more efficient emission enhancement of 1,8-ANS:DREAM in the presence of Eu^{3+} compared to other Ln^{3+} and Ca^{2+}, also confirms structural changes and higher quenching of Trp 169 in the presence of Eu^{3+}. In addition, we observed the higher increase in the emission of 1,8-ANS:DREAM complex in the presence of Nd^{3+}, Er^{3+}, Dy^{3+} and Sm^{3+} compared to that in the presence of Ca^{2+}.
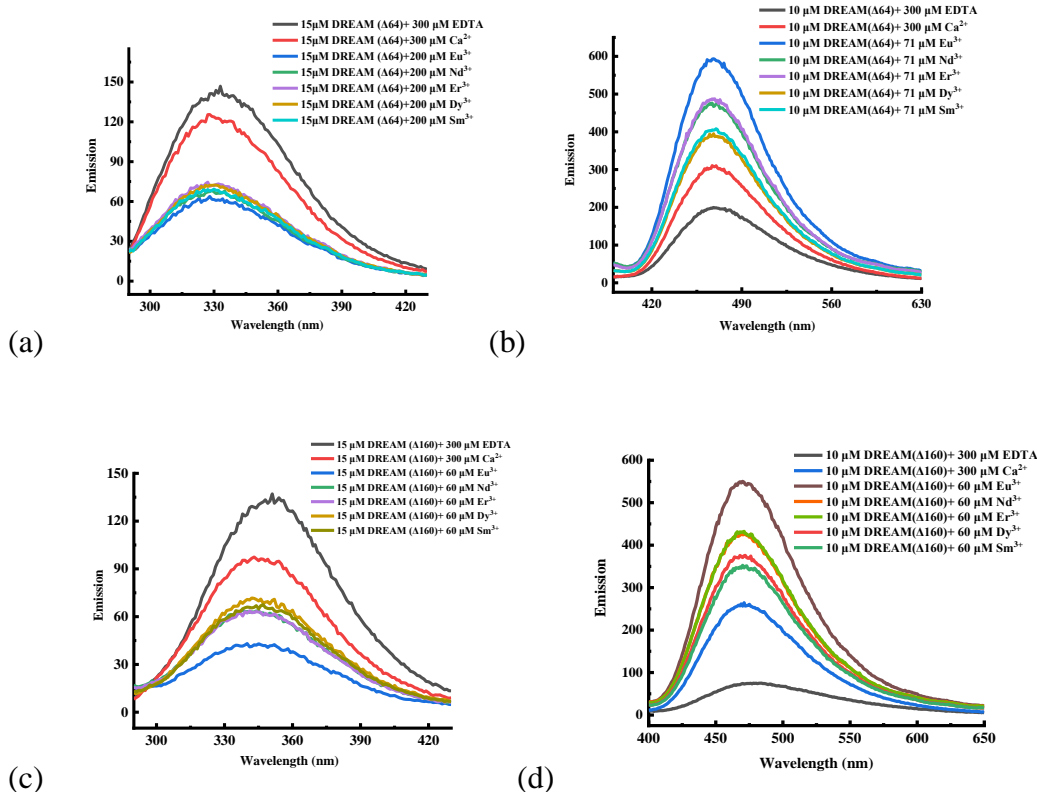
Figure 5.2. (a) Intrinsic emission of Trp 169 in DREAM(Δ64) in presence of 300 μM EDTA and/or presence of 300 μM Ca^{2+} and/or 200 μM Ln^{3+}(λ_{exc} = 280 nm). (b) Extrinsic 1,8-ANS: DREAM(Δ64) emission in the presence of 300 μM EDTA and/or presence of 300 μM Ca^{2+} and/or 71 μM Ln^{3+}(λ_{exc} = 350 nm). (c) Intrinsic emission of Trp 169 in DREAM(Δ160) in presence of 300 μM EDTA and/or presence of 300 μM Ca^{2+} and/or 60 μM Ln^{3+}(λ_{exc} = 280 nm). (d) Extrinsic 1,8-ANS: DREAM(Δ160) emission in the presence of 300 μM EDTA and/or presence of 300 μM Ca^{2+} and/or 60 μM Ln^{3+}(λ_{exc} = 350 nm).

5.3.2. Affinity of Ln^{3+} for DREAM

As both the Trp emission spectra and the emission 1,8-ANS:DREAM complexes are modulated by Ln^{3+} binding to DREAM, we have monitored changes in intrinsic Trp and 1,8-ANS:DREAM complex emission as a function of increasing concentration of Ln^{3+} in order to determine the affinity constant for Ln^{3+} binding to DREAM constructs. The titration curves of Ln^{3+} titration to Ca^{2+}-bound DREAM and Ca^{2+}-bound 1,8-

ANS:DREAM complexes are shown in Figures 5.3 to 5.6. The titration curves for the association of Ln^{3+} to 1,8-ANS:DREAM complexes were analyzed using the single binding site model and the binding constants are summarized in Table 5.1. The titration curves for the association of Ln^{3+} to DREAM were analyzed using the two binding sites model and summarized in Table 5.1. In addition to a high affinity binding, additional increase in 1,8-ANS emission was observed at increased concentrations of Ln^{3+} (more than 100 µM). The binding of Ln^{3+} to a high affinity sites can be attributed to (Ln^{3+} association to EF –hands, whereas the low affinity binding can be attributed to Ln^{3+} interactions with non-specific binding sites.

The overall higher binding affinities obtained from 1,8-ANS:DREAM complex emission changes compared to those obtained from Trp quenching indicate that 1,8-ANS binding to DREAM could result in conformational changes within the protein structure that could lead to higher affinity of Ln^{3+} to binding sites on DREAM. The binding curves obtained from Trp quenching indicate two binding sites; however, we only determined the first binding constant as we were not able to resolve the second binding constant.

(a) (a')

112

(b)

(b')
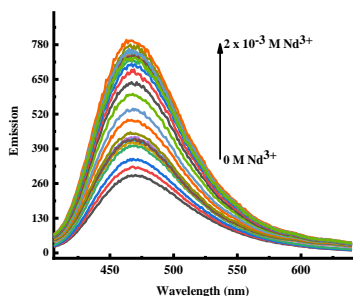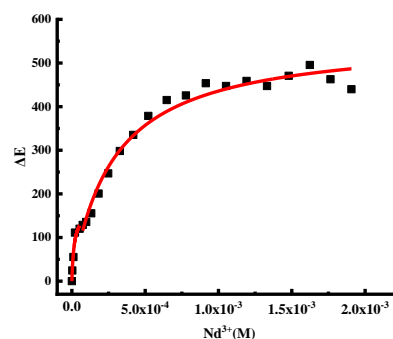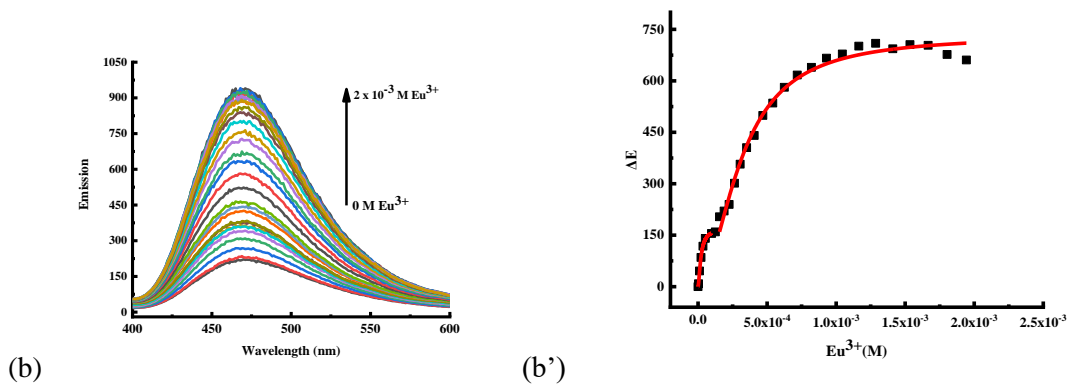
Figure 5.3. Emision data and titration curves from Ln^{3+} binding to 1,8-ANS: DREAM(Δ64) complex. The solid line corresponds to the fitting of experimental data using single binding site. Titration of 10 μM DREAM(Δ64) with 5 mM Nd^{3+}(a) and 5 mM Eu^{3+}(b), in the presence of 30 μM 1,8-ANS and 300 μM Ca^{2+}. Conditions: 20 mM Tris, pH = 7.4, λ_{exc} = 350 nm.

(a)

(a')

(b)

(b')

(c)

(c')
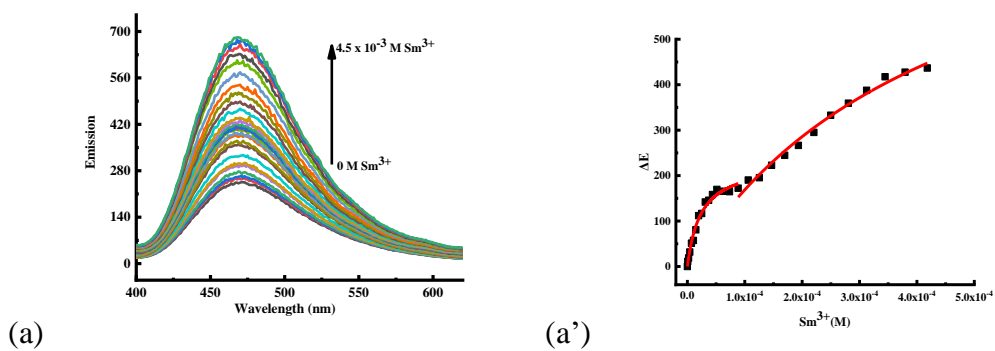
Figure 5.4. Emision data and titration curves from Ln^{3+} binding to 1,8-ANS: DREAM($\Delta64$) complex. The solid line corresponds to the fitting of experimental data using single binding site. Titration of 10 µM DREAM($\Delta64$) with 5 mM Sm^{3+} (a), 1 mM Dy^{3+} (b) and 1 mM Er^{3+} (c) in the presence of 30 µM 1,8-ANS and 300 µM Ca^{2+}. Conditions: 20 mM Tris, pH = 7.4, λ_{exc} = 350 nm.

(a)

(a')

Figure 5.5. Emision data and titration curves from Ln^{3+} binding to 1,8-ANS: DREAM(Δ160) complex. The solid line corresponds to the fitting of experimental data using single binding site. Titration of 10 µM DREAM(Δ160) with 5 mM Nd^{3+} (a), 5 mM Eu^{3+}(b) and 5 mM Er^{3+} (c) in the presence of 30 µM 1,8-ANS and 300 µM Ca^{2+}. Conditions: 20 mM Tris, pH = 7.4, λ_{exc} = 350 nm.

(b)   (b')

Figure 5.6. Emision data and titration curves from Ln^{3+} binding to 1,8-ANS: DREAM(Δ160) complex. The solid line corresponds to the fitting of experimental data using single binding site. Titration of 10 μM DREAM(Δ160) with 1 mM Dy^{3+} (a) and 1 mM Sm^{3+} (b) in the presence of 30 μM 1,8-ANS and 300 μM Ca^{2+}. Conditions: 20 mM Tris, pH = 7.4, λ_{exc} = 350 nm.

From measuring binding affinity of Ln^{3+} to the DREAM constructs, we obtained a lower binding affinity of Ln^{3+} to DREAM(Δ160) compared to that of Ln^{3+} to DREAM(Δ64) indicating that the binding to the high affinity sites is impacted by the missing N- terminal domain in DREAM(Δ160) construct. Figures 5.7 to 5.10 show the Trp emission quenching of DREAM(Δ64)/(Δ160) by addition of Ln^{3+}.
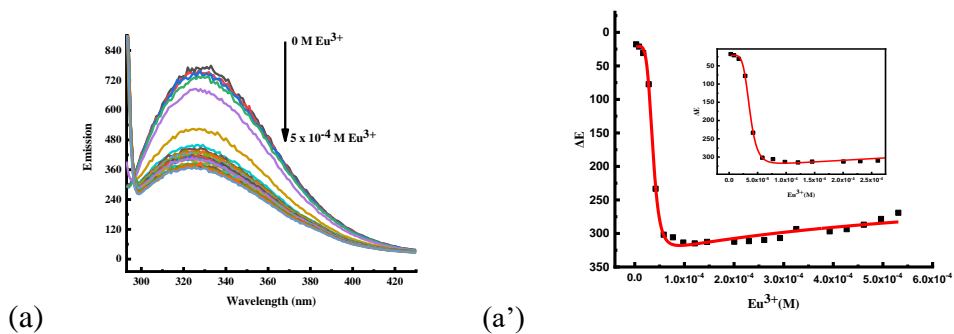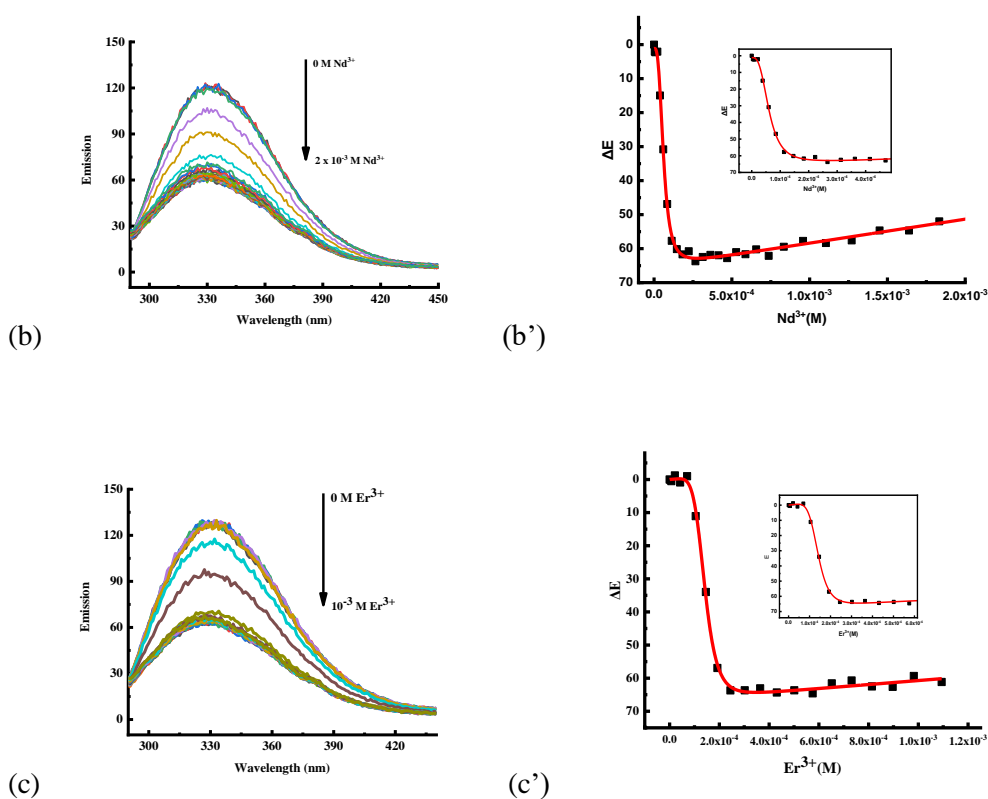
(a)   (a')

116

(b)

(b')

(c)

(c')

Figure 5.7. Emision data of Trp 169 and titration curves from Ln^{3+} binding to DREAM(Δ64). The solid line corresponds to the fitting of experimental data using two binding site model. Titration of 15 μM DREAM(Δ64) with 5 mM Eu^{3+}(a), 5 mM Nd^{3+}(b) and 5 mM Er^{3+} (c) in the presence of 300 μM Ca^{2+}. Conditions: 20 mM Tris, pH = 7.4, λ_{exc} = 280 nm. "the binding curve used to obtain the binding constant is showing in the inset"

(a)

(a')

(b)

(b')

(c)

(c')
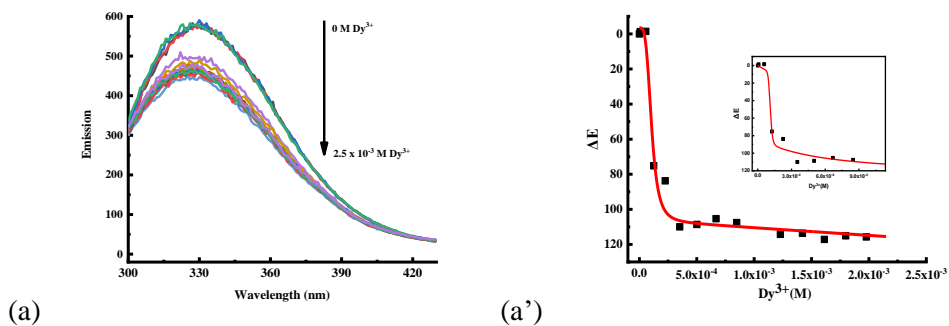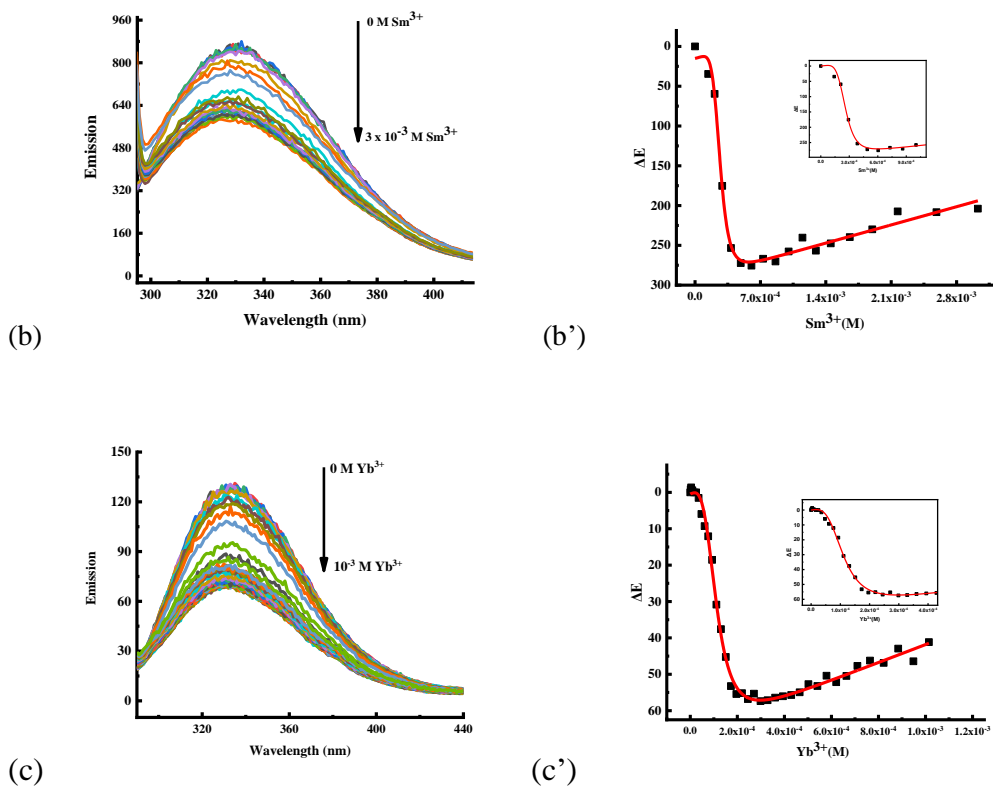
Figure 5.8. Emision data of Trp 169 and titration curves from Ln^{3+} binding to DREAM(Δ64). The solid line corresponds to the fitting of experimental data using double binding site. Titration of 15 μM DREAM(Δ64) with 1 mM Dy^{3+} (a) 1 mM Sm^{3+} (b) and 1 mM Yb^{3+} (c) in the presence of 300 μM Ca^{2+}. Conditions: 20 mM Tris, pH = 7.4, λ_{exc} = 280 nm. "the binding curve used to obtain the binding constant is showing in the inset"
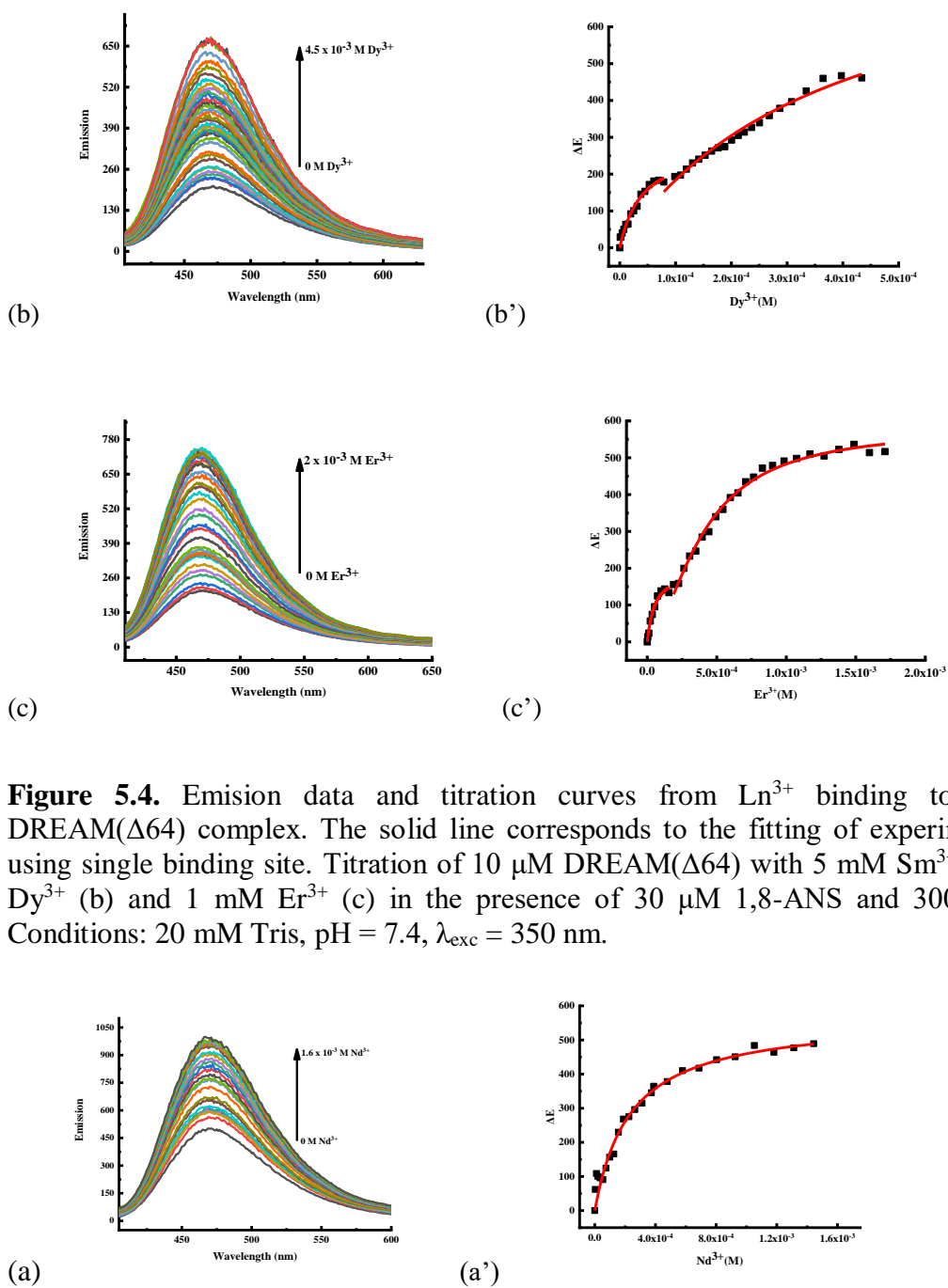

(a)

a')

(b)

(b')

(c)

(c')

Figure 5.9. Emission data of Trp and titration curves from Ln^{3+} binding to DREAM($\Delta160$). The solid line corresponds to the fitting of experimental data using double binding site. Titration of 15 μM DREAM($\Delta160$) with 5 mM Eu^{3+} (a), 5 mM Nd^{3+} (b) and 5 mM Er^{3+} (c) in the presence of 300 μM Ca^{2+}. Conditions: 20 mM Tris, pH = 7.4, λ_{exc} = 280 nm.
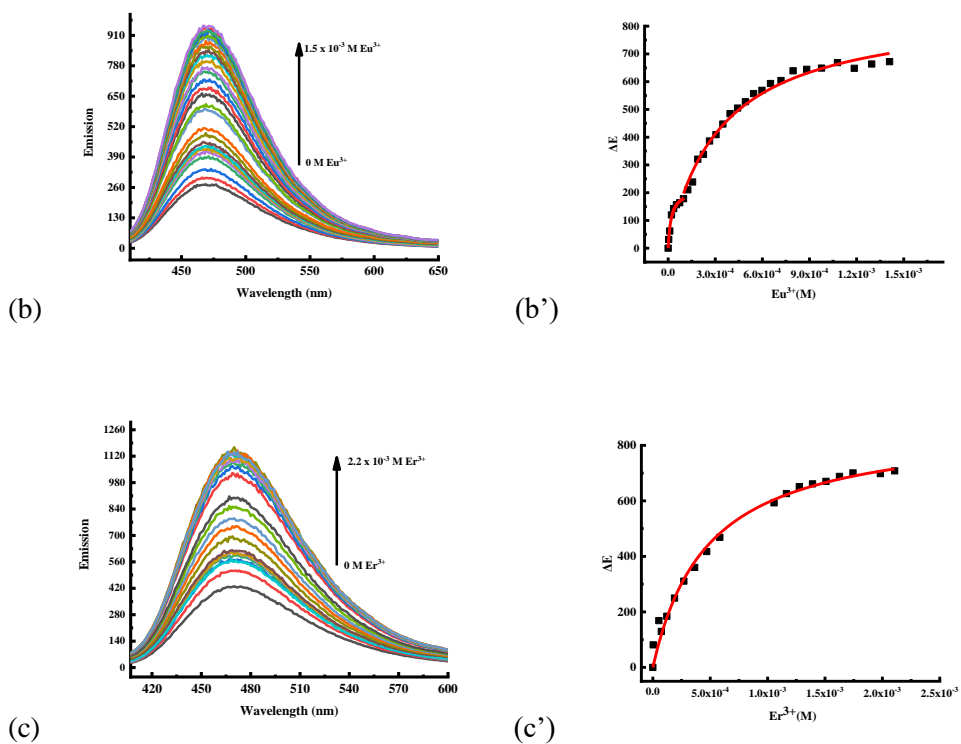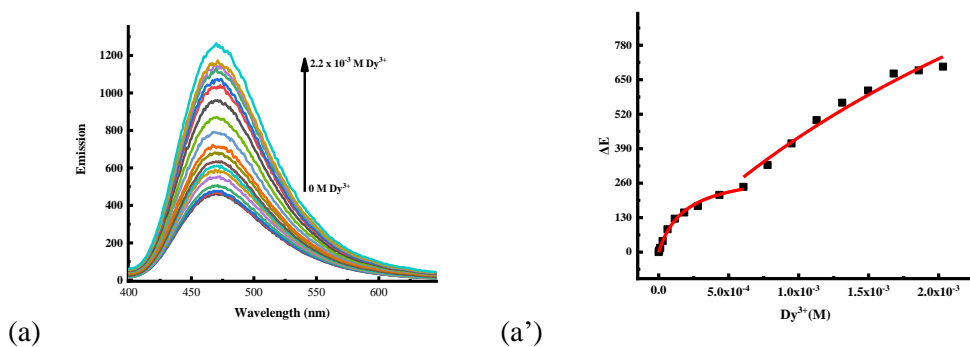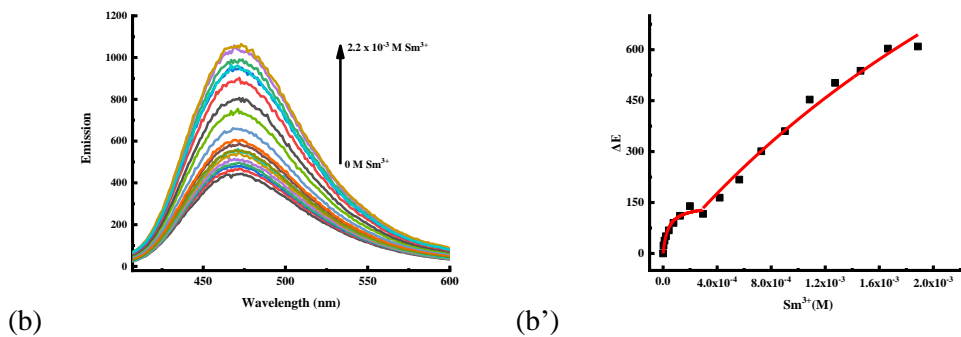

(a)

(a')

(b)

(b')

(c)

(c')
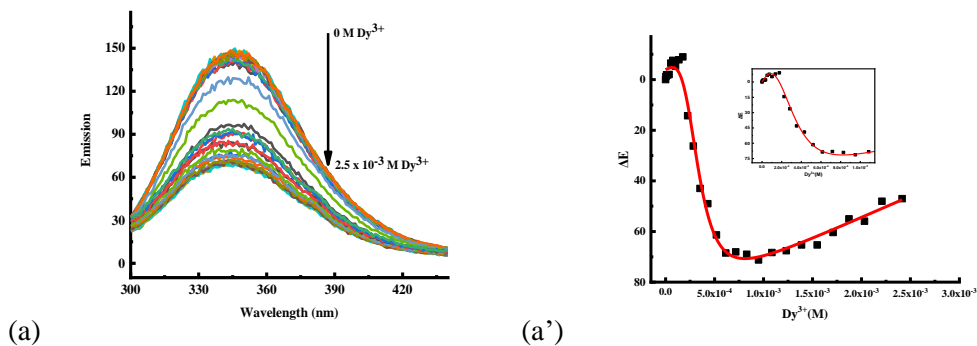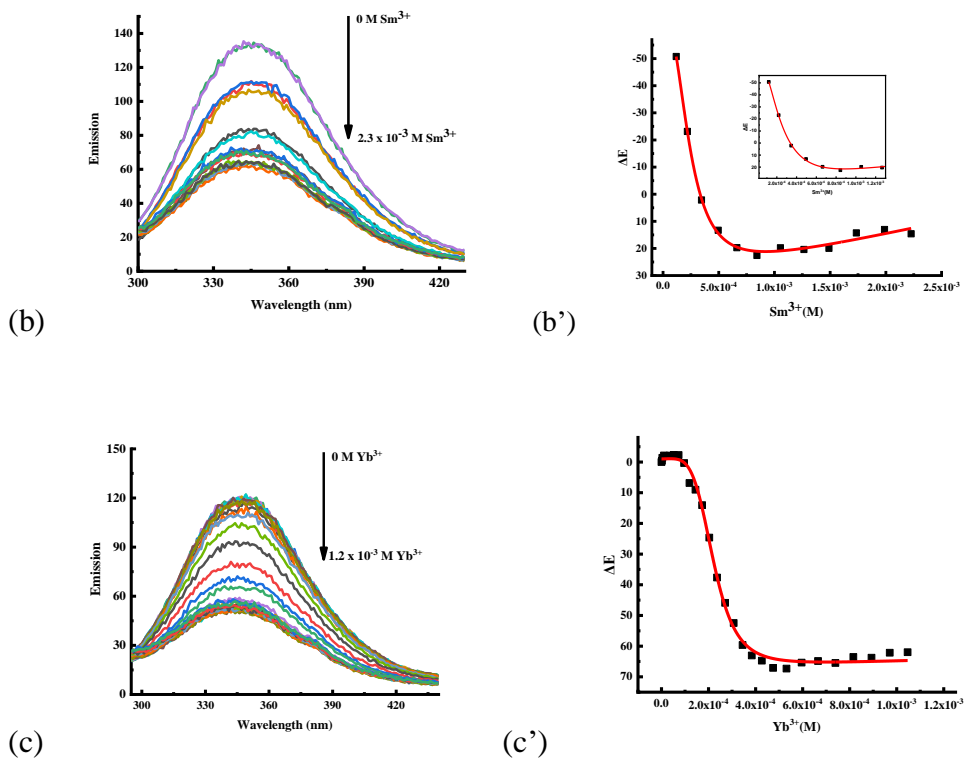
Figure 5.10. Emission data of Trp and titration curves from Ln^{3+} binding to DREAM($\Delta160$). The solid line corresponds to the fitting of experimental data using double binding site. Titration of 15 μM DREAM($\Delta160$) with 1 mM Dy^{3+} (a) 1 mM Sm^{3+} (b) and 1 mM Yb^{3+} (c) in the presence of 300 μM Ca^{2+}. Conditions: 20 mM Tris, pH = 7.4, λ_{exc} = 280 nm. "the binding curve used to obtain the binding constant is showing in the inset"

To further investigate Eu^{3+} interactions with EF-hand proteins, we have characterized quenching of Tyr 99 and phenylalanine (Phe) emission upon addition of Eu^{3+} to CaM. CaM is a model system for Ca^{2+} and other ions interactions with EF-hands. This protein has two domains, C- and N- terminal domain and each domain carries two EF hands. More importantly, as rat CaM lacks Trp residue, the ligand association to individual domain can be characterized in the intact protein by observing changess in Phe and Tyr emission. Since Tyr 99 residue is located in the N- terminal domain, its emission provides information

about metal interactions with EF-hand 3 and EF-hand 4. On the other hand, metal binding to N- terminal domain can be assessed based on changes in Phe 16 emission. Based on the measured binding constant, CaM shows lower affinity to Eu^{3+} compared to that to both DREAM constructs (Fig. 5.11). To monitor the effect of Eu^{3+} on the emission of phenylalanine and tyrosine, two different excitation wavelengths were used. Excitation at 250 nm for phenylalanine and excitation at 277 nm for tyrosine, show emission quenching for both residues in the presence of Eu^{3+}. Table 5.1 lists binding constants for Ln^{3+} complexation to CaM and DREAM($\Delta64$)/($\Delta160$) in the presence of Ca^{2+} from Tyr/Trp quenching.

(a) (a')

121

(b)   (b')
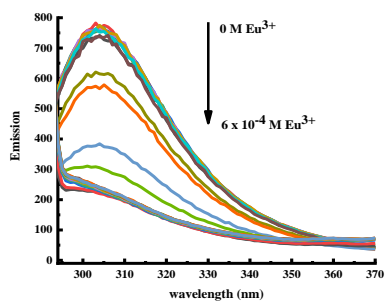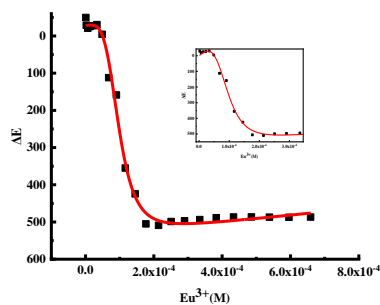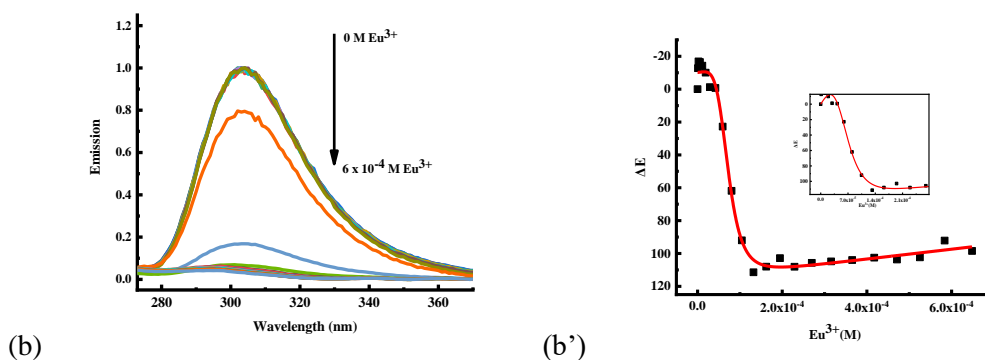
Figure 5.11. Emision data of Tyr 99 (panel a) and of Phe 16 (panel b) as a function of increasing concentration of Eu^{3+}. Titration curves for Eu^{3+} binding to the N- terminal domain (panel a') and C- terminal domain (panel b') of CaM. The solid line corresponds to the fitting of experimental data using double binding site model. Titration of 20 μM CaM with 2 mM Eu^{3+} in the presence of 300 μM Ca^{2+}. Conditions: (a) 20 mM Tris, pH = 7.4, λ_{exc} = 277 nm. (b) 20 mM Tris, pH = 7.4, λ_{exc} = 250 nm.

5.3.3. Binding Ln^{3+} to CaM and DREAM results in enhanced emission of Ln^{3+}

Figure 5.12 shows the Eu^{3+} emission spectra in the absence and presence of CaM, DREAM(Δ64) and DREAM(Δ160). The increase in the emission of Eu^{3+} upon excitation at 280 nm indicates efficient energy transfer between intrinsic Trp 169 residues in DREAM- and Tyr 99 residue in CaM Eu^{3+}. Dy^{3+} emission at 580 nm also increased in the presence of DREAM(Δ160) (Fig 5.12(d)). This observation is consistent with the previous study by Gonzalez et al. (2016) in which Tb^{3+} emission was enhanced upon addition of DREAM(Δ64)[1] as well as with their studies that show enhancement of Ln^{3+} emission when binding to other EF-hand proteins.[1, 13, 14, 21]
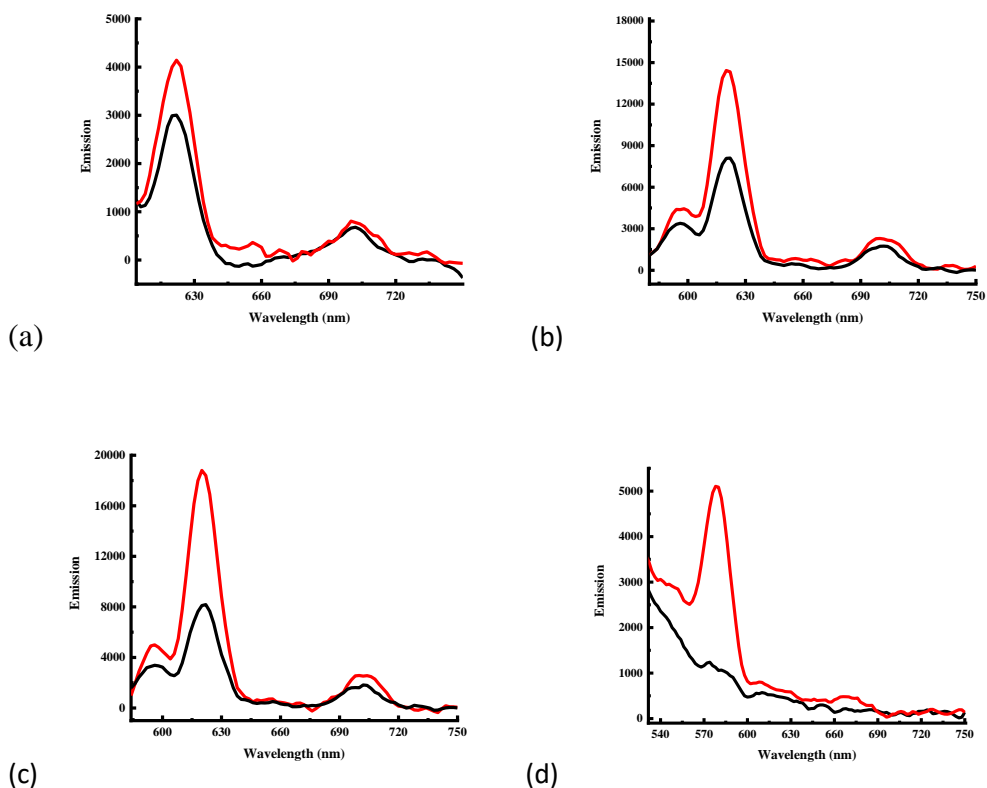
Figure 5.12. (a-c) Emission of 100-110 µM Eu^{3+} (in black) and 20 µM Eu^{3+} in the presence of 10 µM CaM, DREAM($\Delta64$) and DREAM($\Delta160$) (in red). (d) Emission of 200 µM Dy^{3+} (in black) and 20 µM Dy^{3+} in the presence of 10 µM DREAM($\Delta160$) (in red). Conditions: 20 mM Tris, pH 7.4 and $\lambda_{exc} = 280$ nm.

Interestingly, we noticed an increase at 595 nm for Eu^{3+} emission in addition to increase of emission at 620 nm and 700 nm in the presence of DREAM($\Delta64$)/($\Delta160$), while in the presence of CaM we only observed increase in the Eu^{3+} emission at 620 nm and 700 nm which is consistent with the previous study by Drobot et al (2019), that reported absence of the 592 nm emission increase in the presence of CaM.[13]

5.3.4. Circular dichroism study: Structural changes upon binding of Ln^{3+} to DREAM

As we noticed quenching of Trp emission by adding Ln^{3+} to EF-hand 3 and 4, we decided to analyze whether Ln^{3+} binding to DREAM will result in structural changes similar to the ones occurred by the presence of Ca^{2+}. Secondary structural analysis in DREAM ($\Delta 64$) interaction with Eu^{3+} using circular dichroism (CD) showed structural transitions analogous to those occurred with Ca^{2+} and Tb^{3+}.[1] The CD spectra of apoDREAM($\Delta 64$), Ca^{2+}DREAM($\Delta 64$) and Eu^{3+}DREAM ($\Delta 64$) is shown in Figure 5.13. We noticed that addition of Eu^{3+} to the DREAM($\Delta 64$) leads to a CD spectrum similar to the one observed upon addition of Ca^{2+}. Specifically, Ln^{3+} addition results in more negative CD signal at 208 and 220 nm, which can be attributed to the increase in the protein α-helical content and/or reorganization of α-helices. In the presence of Eu^{3+}, a distinctive CD spectrum can be observed which shows an intermediate structure between apo and Ca^{2+}-bound (Fig. 5.13).
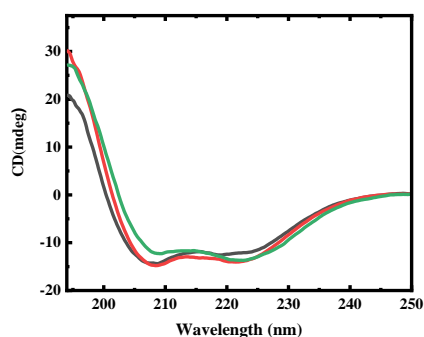
Figure 5.13. CD spectra of DREAM($\Delta 64$) in the presence/ absence of Ca^{2+} and/or Eu^{3+}. 10 µM DREAM($\Delta 64$) and 500 µM EDTA (in black). 10 µM DREAM($\Delta 64$) and 500 µM Ca^{2+} (in red). 10 µM DREAM($\Delta 64$) and 50 µM Eu^{3+} (in green)

5.3.5. Luminescence decay of Ln^{3+}-bound CaM and DREAM

In addition to characterizing steady state emission properties of Ln^{3+}-bound DREAM, we also characterized the lifetimes of Ln^{3+} binding to CaM and the DREAM constructs. The lifetime measurements were carried out in the time domain and the lifetime traces for Eu^{3+} bound to CaM/DREAM in the absence of EDTA are shown in Figure 5.14. Both Ln^{3+}-protein complexes were excited using the 355 nm line of a Nd:YAG pulsed laser. The traces were analyzed using a mono exponential decay model. The lifetime values of Ln^{3+} bound to CaM/DREAM in the presence/absence of EDTA were presented in table 5.2. Based on the data, DREAM(Δ160) showed an overall of longer lifetime compared to DREAM(Δ64) and CaM indicating the Ln^{3+} bound to DREAM(Δ160) are less solvent exposed and have less water molecules coordinating to Ln^{3+} which could result in longer lifetime.
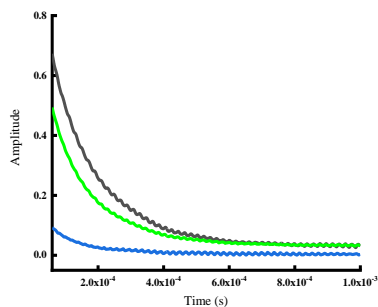
Figure 5.14. Time resolved emission data for Eu^{3+} bound to CAM and DREAM constructs. Solution of 110 μM Eu^{3+} and 41 μM CaM (in blue). Solution of 10 μM Eu^{3+} and 10 μM DREAM(Δ64) (in green). Solution of 10 μM Eu^{3+} and 10 μM DREAM(Δ160) (in black). Conditions: 20 mM Tris, pH = 7.4 and λ_{exc} = 355 nm

Table 5.1. Dissociation constants of Ln^{3+} binding to apoCaM and apoDREAM

K_d(nM)	N	K_d(nM)(from Trp/Tyr quenching)	K_d(nM)(1,8-ANS:DREAM)
$Eu^{3+}CaM$	4.1 ± 0.4	Tyr: 322 ± 6 Phe: 295 ± 7	N/A
$Eu^{3+}DREAM(\Delta64)$	5.5 ± 0.3	119 ± 2	$66 \pm 3 (1023 \pm 33)*$
$Nd^{3+}DREAM(\Delta64)$	3.0 ± 0.1	202 ± 3	$53 \pm 23 (936 \pm 83)$
$Er^{3+}DREAM(\Delta64)$	5.7 ± 0.4	468 ± 1	$179 \pm 36 (1302 \pm 46)$
$Dy^{3+}DREAM(\Delta64)$	3.7 ± 1.5	348 ± 40	$129 \pm 23 (1269 \pm 129)$
$Sm^{3+}DREAM(\Delta64)$	5.8 ± 0.7	890 ± 20	$76 \pm 7 (1500 \pm 171)$
$Yb^{3+}DREAM(\Delta64)$	3.4 ± 0.2	368 ± 7	N/A
$Eu^{3+}DREAM(\Delta160)$	2.8 ± 0.1	176 ± 3	$70 \pm 6 (1106 \pm 66)$
$Nd^{3+}DREAM(\Delta160)$	2.8 ± 0.2	192 ± 4	115 ± 4
$Er^{3+}DREAM(\Delta160)$	3.9 ± 0.2	225 ± 4	255 ± 73
$Dy^{3+}DREAM(\Delta160)$	3.5 ± 0.3	1126 ± 40	614 ± 63
$Sm^{3+}DREAM(\Delta160)$	2.4 ± 0.3	790 ± 53	126 ± 33
$Yb^{3+}DREAM(\Delta160)$	4.6 ± 0.2	734 ± 10	N/A

*: Weak binding affinity

Table 5.2. Lifetime values for Ln^{3+} binding to CaM

	τ_1 (µs)
$Eu^{3+}CaM$	155 ± 0.3
$Eu^{3+}CaM$ + EDTA	149 ± 0.5
$Nd^{3+}CaM$	133 ± 0.8
$Nd^{3+}CaM$ + EDTA	133 ± 0.7
$Er^{3+}CaM$	101 ± 0.5
$Er^{3+}CaM$ + EDTA	137 ± 24
$Dy^{3+}CaM$	132 ± 0.4
$Dy^{3+}CaM$ + EDTA	110 ± 0.4
$Sm^{3+}CaM$	141 ± 0.3
$Sm^{3+}CaM$ + EDTA	136 ± 0.4

Table 5.3. Lifetime values for Ln^{3+} binding to DREAM($\Delta64$)

	τ_1 (μs)
Eu^{3+}DREAM($\Delta64$)	178 ± 2
Eu^{3+}DREAM($\Delta64$) + EDTA	125 ± 0.3
Nd^{3+}DREAM($\Delta64$)	135 ± 0.1
Nd^{3+}DREAM($\Delta64$) + EDTA	127 ± 0.2
Er^{3+}DREAM($\Delta64$)	139 ± 0.3
Er^{3+}DREAM($\Delta64$) + EDTA	139 ± 0.2
Dy^{3+}DREAM($\Delta64$)	138 ± 0.1
Dy^{3+}DREAM($\Delta64$) + EDTA	133 ± 0.1
Sm^{3+}DREAM($\Delta64$)	112 ± 0.5
Sm^{3+}DREAM($\Delta64$) + EDTA	122 ± 0.5

Table 5.4. Lifetime values for Ln^{3+} binding to DREAM($\Delta160$)

	τ_1 (μs)
Eu^{3+}DREAM($\Delta160$)	170 ± 0.5
Eu^{3+}DREAM($\Delta160$) + EDTA	144 ± 0.1
Nd^{3+}DREAM($\Delta160$)	149 ± 0.3
Nd^{3+}DREAM($\Delta160$) + EDTA	137 ± 0.4
Er^{3+}DREAM($\Delta160$)	166 ± 0.9
Er^{3+}DREAM($\Delta160$) + EDTA	143 ± 0.8
Dy^{3+}DREAM($\Delta160$)	168 ± 0.7
Dy^{3+}DREAM($\Delta160$) + EDTA	129 ± 0.3
Sm^{3+}DREAM($\Delta160$)	237 ± 1
Sm^{3+}DREAM($\Delta160$) + EDTA	136 ± 0.2

5.3.6. Frequency-domain luminescence decay for Ln^{3+}DREAM($\Delta64$)

To provide information about the impact of Ln^{3+} association on EF-hands on the dynamic properties of Trp 169 residue in DREAM, the fluorescence lifetime of Trp residue was characterized in the frequency domain (Fig. 5.15). A sample solution of 10 μM DREAM($\Delta64$) was prepared in 20 mM Tris, pH 7.4 and Eu^{3+} was added to the solution to the final concentration of 10 μM. The lifetime values, fractional intensities and pre-exponentional factors for Eu^{3+}DREAM are presented in table 5.5. Lifetime values show

faster fluorescence decay of Trp in Eu^{3+}DREAM compared to the values obtained for apoprotein and Ca^{2+} bound protein. This could be explained by more efficient energy transfer from Trp 169 residue to Eu^{3+}.

To observe luminescence decay of 1,8-ANS:DREAM complex in the presence of Ln^{3+}, three sample solutions of 3:1 1,8-ANS:DREAM(Δ64) were prepared in 20 mM Tris, pH 7.4 and lanthanides Eu^{3+}, Er^{3+} and Yb^{3+} were added to the solution to a final concentration of 10 μM. Among Ln^{3+}, Yb^{3+} results in fastest decay of 1,8-ANS:DREAM complex with an overall of reduced lifetime in the presence of Ln^{3+} compared to those in the form of apo-protein and in the presence of Ca^{2+}. Figure 5.16 and table 5.6 show the decay based on phase delay and modulation ratio.
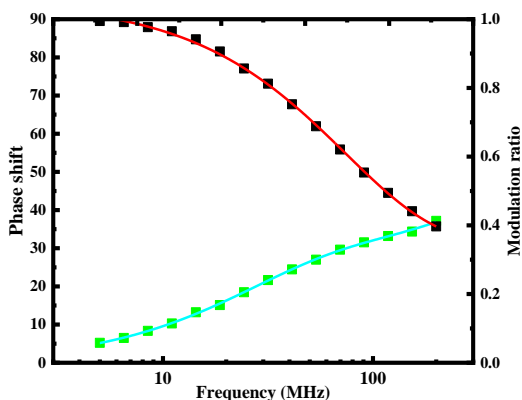
Figure 5.15. The frequency-related fluorescence decay of DREAM(Δ64) in the presence of 10 μM Eu^{3+}. λ_{exc} = 280 nm

Table 5.5. Fluorescence decay values of DREAM(Δ64) in the form of apoDREAM(Δ64) and in the presence of Ca^{2+} and Eu^{3+}

	$\tau_1(ns)$	$\tau_2(ns)$	$\tau_3(ns)$	$f_1(\%)$	$f_2(\%)$	$f_3(\%)$	$\alpha_1(\%)$	$\alpha_2(\%)$	$\alpha_3(\%)$	$\langle\tau\rangle(ns)$	x^2
apoDREAM(Δ64)	0.24 ± 0.03	2.5 ± 0.1	7.1 ± 0.3	17.3 ± 0.8	45.4 ± 3.0	37.3 ± 0.3	75.1	19.2	5.9	3.8	1.5
Ca^{2+}DREAM(Δ64)	0.16 ± 0.02	1.9 ± 0.1	6.3 ± 0.2	22.0 ± 0.9	37.5 ± 2.0	40.5 ± 2.0	84.5	12.1	3.3	3.1	0.9
Eu^{3+}DREAM(Δ64)	N/A	1.09 ± 0.04	5.07 ± 0.09	18.6 ± 0.5	34.8 ± 0.8	46.4 ± 0.9	N/A	32.0	9.16	2.73	5.2
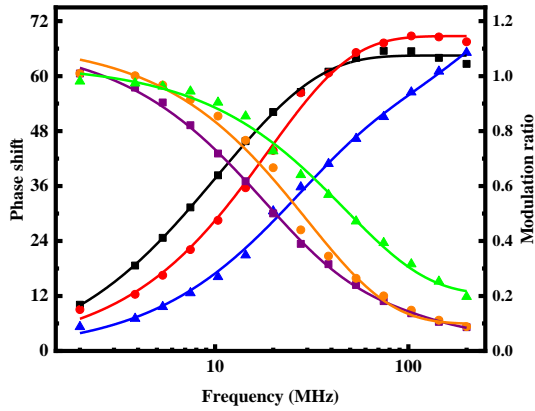
Figure 5.16. The frequency-related fluorescence decay of 1,8-ANS:DREAM(Δ64) in the presence of 10 μM Ln^{3+}. λ_{exc} = 300 nm

Table 5.6. Fluorescence decay values of 1,8-ANS:DREAM(Δ64) in the form of apoDREAM(Δ64) and in the presence of Ca^{2+}, Eu^{3+}, Er^{3+}, and Yb^{3+}. *The lifetime value for 1,8-ANS was fixed at 0.28 ns

1,8-ANS	$\tau_1(ns)$ *	$\tau_2(ns)$	$\tau_3(ns)$	$f_1(\%)$	$f_2(\%)$	$f_3(\%)$	$\alpha_1(\%)$	$\alpha_2(\%)$	$\alpha_3(\%)$	$\langle\tau\rangle(ns)$	χ^2
apoDREAM(Δ64)[19]	028F	4.1 ± 0.1	16.9 ± 0.2	1.6 ± 0.1	15.4 ± 0.9	83.0 ± 1.0	62.6	21.9	15.5		0.9
Ca^{2+}DREAM(Δ64)[19]	0.28F	4.3 ± 0.2	18.0 ± 0.1	1.4 ± 0.1	9.7 ± 0.6	88.9 ± 0.5	40.3	16.9	42.7		0.9
Eu^{3+}DREAM(Δ64)	0.28F	5.1 ± 0.2	16.8 ± 0.2	3.8 ± 0.0	17.5 ± 1.0	81 ± 1	62.5	15.5	21.9	14.5	1.8
Er^{3+}DREAM(Δ64)	0.28F	4.8 ± 0.2	14.6 ± 0.2	3.0 ± 0.0	18.4 ± 1.0	80.5 ± 1.0	53.8	18.9	27.2	12.6	2.4
Yb^{3+}DREAM(Δ64)	0.28F	2.4 ± 0.0	10.7 ± 0.2	4.7 ± 0.0	42.5 ± 0.0	51.2 ± 0.0	43.0	44.6	12.3	6.55	6.4

5.4. Discussion

In this chapter, we showed that Eu^{3+}, Nd^{3+}, Er^{3+}, Dy^{3+}, Sm^{3+} and Yb^{3+} mimic Ca^{2+} association in terms of triggered changes in the protein structure. All studied Ln^{3+} show an affinity that is superior to the affinity of the physiological ligand, Ca^{2+}, for DREAM. The K_d of CaM titration with Eu^{3+} indicates a lower binding affinity compared to the two DREAM constructs which can also be explained for the slightly lower affinity of Ca^{2+} to CaM compared to that to the DREAM.[23-25] Overall, DREAM($\Delta 160$) shows a lower affinity to Ln^{3+} compared to DREAM($\Delta 64$) affinity to Ln^{3+}. Dy^{3+} and Sm^{3+} show lower affinity than other Ln^{3+} to the two DREAM constructs, which could be also evidenced by less pronounced quenching of the Trp emission and weaker increase in the emission of 1,8-ANS:DREAM complexes. This may be attributed to "less conformational changes" occurred in DREAM constructs in the presence of these Ln^{3+}. The CD signal of DREAM in the presence of Eu^{3+} shows a small deviation near 208 nm, which is sensitive to the presence of β-sheets. DREAM is primarily α-helical and antiparallel β-sheets are formed between the metal binding loops of each EF-hand pair, therefore these five Ln^{3+} ions induced the same structural changes as Tb^{3+}, namely the loss of short β-sheet regions. Structural changes can also be confirmed by observing the increase in the emission of 1,8-ANS:DREAM complex. The increase in the lifetime of Ln^{3+}protein complex is attibuted to the shielding effect from protein to the Ln^{3+} ion from surrounding water, since in the presence of EDTA the Ln^{3+} becomes more available for water molecules resulting in faster fluorescence decay of Ln^{3+}. The increase in the lifetime for some Ln^{3+}DREAM complexes in the presence of EDTA could be the result of experimental error in measuring. Aromatic amino acids can transfer energy to the bound Ln^{3+}, which has been observed by Trp

emission quenching and fluorescence lifetime measurements. The faster luminescence decay of DREAM(Δ64) in the presence of Eu^{3+} showed more efficient energy transfer of nearby Trp to Eu^{3+}. Luminescence decay for of 1,8-ANS:DREAM(Δ64) in the presence of Ln^{3+} showed shorter lifetime in the presence of Ln^{3+} indicating that the 1,8-ANS binding sites on DREAM are more solvent exposed. In conclusion, it has been shown that the five studied Ln^{3+} could be suitable candidates for spectroscopic studies of EF-hand proteins.

5.5. Materials and methods

Recombinant mouse DREAM(Δ64) and DREAM(Δ160) were expressed in E. coli and isolated and purified as described previously.[15,16] DREAM(Δ64) is a truncated version of the protein that misses first 64 amino acid residues. The absence of the N- terminal of the protein prevents formation of inclusion bodies but the core protein is fully functional in terms of metal binding.[15,17,18] DREAM(Δ160) construct contains residues 161 to 256 of the native protein that form C- terminal domain with active EF hand 3 and 4. Protein concentrations were measured by UV-Vis spectroscopy using $\varepsilon_{280nm} = 19000$ M^{-1} for DREAM(Δ64) and $\varepsilon_{280nm} = 11000$ M^{-1} for DREAM(Δ160). 8-anilino-1-naphthalenesulfonic acid (1,8-ANS) was purchased from Cayman Chemicals Inc. Concentrated stock solution of hydrophobic probe 1,8-ANS was prepared in ultrapure water and the final concentration of the probe was determined using an ε_{350} of $4995M^{-1}cm^{-1}$.[18] $EuCl_3.6H_2O$, $Er(NO_3)_3.6H_2O$, $Nd(NO_3)_3.6H_2O$, $Sm(NO_3)_3.6H_2O$, and $Dy(NO_3)_3.5H_2O$ were obtained from Fisher scientific lab equipment and supplies and were used as received. $CaCl_2.2H_2O$ and ethylenediaminetetraacetic acid (EDTA) were obtained from Sigma-Aldrich and were used as received. Stock solutions of each Ln^{3+} salts in concentration range from 1 mM to 10 mM were prepared and the protein samples for fluorescence and CD

measurements were prepared by diluting the 107.8 μM and 818 μM of each of DREAM constructs in 20 mM Tris (pH 7.4) to a final concentration of 10 or 20 μM DREAM. To prepare apoDREAM(Δ64) or apoDREAM (Δ160) samples, 1.0 mM EDTA was added to the solution, whereas Ca^{2+} bound DREAM samples were prepared by addition of 300 μM $CaCl_2$. To determine Ln^{3+} association to DREAM by probing emission of 1,8-ANS DREAM complexes, aliquots of Ln^{3+} stock were added to 10 μM DREAM in the presence 30 μM of 1,8-ANS in 20 mM Tris (pH 7.4).

5.5.1. Photophysical characterization of the Ln^{3+}DREAM complexes

Fluorescence emission experiments were carried out on a Cary Eclipse fluorescence spectrophotometer (Agilent). For fluorescence titrations, the sample was placed in a 5 mm × 10 mm quartz cuvette and excited along the 10 mm path. For Trp emission, excitation wavelength of 280 nm was used and to determine the equilibrium dissociation constant, 15μM of each of the protein was titrated with 1-5 mM of Ln^{3+} salts in 300 μM Ca^{2+} in 20 mM Tris (pH 7.4). To observe 1,8-ANS emission spectra changes, excitation wavelength of 350 nm was used and to determine the corresponding equilibrium dissociation constants, 10 μM DREAM was titrated with 1-5 mM of Ln^{3+} in 300 μM $CaCl_2$ in 20 mM Tris, pH 7.4. Equilibrium dissociation constant for Ln^{3+} binding to Ca^{2+}1,8-ANS:DREAM and Ca^{2+}DREAM were determined using equation 1 and 2:

$$\Delta E_{1,8-\text{ANS:DREAM}} = \frac{B_{max}[Ln^{3+}]}{K_d + [Ln^{3+}]} \qquad \text{Eq. 1}$$

Where:

$\Delta E_{1,8-ANS:DREAM}$: Emission changes of the 1,8-ANS:DREAM complex upon addition of Ln^{3+}

B_{max} : Maximum specific binding corresponding to the highest concentration of Ln^{3+}

K_d: Equilibrium dissociation constant obtained from the binding curve of emission changes as the function of Ln^{3+} concentration

$$\Delta E_{Trp} = B_{max1} \frac{[Ln^{3+}]^n}{K_{d1}^n + [Ln^{3+}]^n} + B_{max2} \frac{[Ln^{3+}]}{K_{d2} + [Ln^{3+}]} \qquad \text{Eq. 2}$$

Where:

ΔE_{Trp}: Emission changes of Trp upon addition of Ln^{3+}

B_{max}: Maximum specific binding relating to the highest concentration of Ln^{3+}

K_d: Equilibrium dissociation constant obtained from the binding curve of emission changes as the function of Ln^{3+} concentration

n: The number of binding sites

The overall equilibrium dissociation constants (K_d) for Ln^{3+} binding to apo-DREAM were calculated from the overall apparent dissociation constant using equation 3.[18]

$$K_d = \frac{K_{app}K_{dCa^{2+}}}{(K_dCa^{2+} + [Ca^{2+}]_T)} \qquad \text{Eq. 3}$$

K_{app} represent the dissociation constant of Ln^{3+} to DREAM in the presence of Ca^{2+}, $K_{dCa^{2+}}$ represents the equilibrium dissociation constant for Ca^{2+} binding to apoDREAM, which

was previously determined to be 1 μM,[15] $[Ca^{2+}]_T$ is the total concentration of Ca^{2+}, which is 300 μM.

Circular dichroism measurements were performed in a Jasco J-815 CD spectrometer through the 1 mm path of a quartz cuvette (model J-815, Jasco, Easton, MD). Three separate samples for CD were prepared in three Eppendorf tubes. All samples contained 10 μM DREAM (Δ64) in 20mM Tris buffer PH 7.4. To the first sample 500 μM EDTA was added to ensure that we get the spectra of apoprotein. To the second 500 μM Ca^{2+} was added and to the third 30 μM of Eu^{3+}.

5.5.2. Time resolved fluorescent studies

Lifetime measurements of $Ln^{3+}CaM$ and $Ln^{3+}DREAM(Δ64)/(Δ160)$ were carried out using home-build instrument. The samples were excited through a 355 nm output from a Nd:YAG laser (5ns, pulse Minilite II, Continuum). The emission was detected through 400 nm long pass filter (Andover Corp) using an amplified photo-diode PDA100A (Thorlabs Inc., Newton, New Jersey). A 400 MHz oscilloscope (Textronics) was used to digitize and store the signal. The data were analyzed using an exponential decay model in Origin data analyzing software (OriginLab) (eq. 4).

$$I = \sum_i \alpha_i e^{-\frac{t}{\tau i}} \qquad \qquad \text{Eq. 4}$$

where α_i are the pre-exponential factors and τ_i are the lifetimes for each process which is 1 in our experiments.

5.5.3. Frequency-domain lifetime measurements

Lifetime measurements as a function of frequency were performed at room temperature using Chronos spectrofluorometer (ISS, Champaign IL). Three solutions of 3:1 1,8-ANS/DREAM(Δ64) each containing 10 μM of three Ln^{3+} ions (Eu^{3+}, Er^{3+}, Yb^{3+}) were excited using a 300 nm laser diode through a 305 nm band pass filter. For Trp excitation, a laser diode with an output of 280 nm was used.

References

1. Gonzalez, W. G.; Ramos, V.; Diaz, M.; Garabedian, A.; Molano-Arevalo, J. C.; Fernandez-Lima, F. and Miksovska, J. Characterization of the Photophysical, Thermodynamic, and Structural Properties of the Terbium (III)-DREAM Complex. *Biochemistry*, **2016**, *55*, 1873-1886.

2. Fontán-Lozano, A.; Capilla-Gonzalez, V.; Aguilera, Y.; Mellado, N.; Carrión, A.M.; Soria, B. and Hmadcha, A. Impact of Transient Down-Regulation of DREAM in Human Embryonic Stem Cell Pluripotency. *Stem Cell Res*. **2016**, *16*, 568-578.

3. Rivas, M.; Mellström, B.; Torres, B.; Cali, G.; Ferrara, A.M.; Terracciano, D.; Zannini, M.; Morreale de Escobar, G. and Naranjo, J.R. The DREAM Protein is Associated with Thyroid Enlargement and Nobular Development. *Mol. Endocrinol*. **2009**, *23*, 862-870.

4. Craig, T. A; Benson, L. M.; Venyaminor, S. Y.; Klimtchuk, E. S.; Bajzert, Z.; Prendergast, F. G.; Naylor, S. and Kumar, R. The Metal-Binding Properties of DREAM. *J. Bio. Chem*. **2002**, *277*, 10955-10966.

5. Brittain, H. G.; Richardson, F. S. and Martin, R. B. Terbium (III) Emission as a Probe of Calcium(II) Binding Sites in Proteins. *J. Am. Chem. Soc*. **1976,** *98*, 8255-8260.

6. de Jersy, J. and Martin, R. B. Lanthanide Probes in Biological Systems: The Calcium Binding Site of Pancreatic Elastase as Studied by Terbium Luminescence. *Biochemistry*, **1980**, *19*, 1127-1132.

7. Hungerford, G.; Hussain, F.; Patzke, G. R. and Green, M. The Photophysics of Europium and Terbium Polyoxometalates and their Interaction with Serum Albumin: A Time-Resolved Luminescence Study. *Phys. Chem. Chem. Phys*. **2010**, *12*, 7266-7275.

8. Pidcock, E. and Morre, G.R. Structural characteristics of protein binding sites for calcium and lanthanide ions. *J. Biol. Inorg. Chem*. **2001**, *6*, 479-489.

9. Snyder, E. E.; Buoscio, B. W. and Falke, J. J. Calcium(II) Site Specificity: Effect of Size and Charge on Metal Ion Binding to an EF-Hand-Like Site. *Biochemistry*, **1990**, *29*, 3937-3943.

10. Furie, B. C.; Mann, K. G. and Furie, B. Substition of Lanthanide Ions for Calcium Ions in the Activation of Bovine Prothrombin by Activated Factor X. *J. Biol. Chem*. **1976**, *251*, 3235-3241.

11. Bayshaw, L. L.; Smith, R. S. G.; Badaoui, M.; Irving, J. A. and Price, S. R. Lanthanides Compete with Calcium for Binding to Cadherins and Inhibit Cadherin-Mediated Cell Adhesion. *Metallomics,* **2019**, *11*, 914-924.

12. Edington, S. C.; Gonzalez, A.; Middendorf, T. R.; Halling, B.; Aldrich, R. W. and Baiz, C. R. Coordination to Lanthanide Ions Distorts Binding Site Conformation in Calmodulin. *Proc. Natl. Acad. Sci.* **2017**, *115*, 3126-3134.

13. Drobot, B.; Schmidt, M.; Mochizuki, Y.; Abe, T.; Okuwaki, K.; Brulfert, F.; Falke, S.; Samsonov, S.A.; Komeiji, Y.; Betzel, C.; Stumpf, T.; Raff, J. and Tsushima, S. Cm^{3+}/Eu^{3+} Induced Structural, Mechanistic and Functional Implications for Calmodulin. *Phys. Chem. Chem. Phys.* **2019**, *21*, 21213- 21222.

14. Chaudhuri, D. and Horrocks, Jr. W. DeW. Characterization of Lanthanide Ion Binding to the EF-Hand Protein S100β by Luminescence Spectroscopy. *Biochemistry*, **1997**, *36*, 9674-9680.

15. Osawa, M.; Tong, K. I.; Lilliehook, C.; Wasco, W.; Buxbaum, J. D.; Mary Cheng, H.Y.; Penninger, J. M.; Ikura, M. and Ames, J.B. Calcium-regulated DNA Binding and Oligomerization of the Neuronal Calcium-sensing Protein, Calsenilin/DREAM/KChIP3. *J. Biol. Chem.* **2001**, *276*, 41005-41013.

16. Gonzalez, W. G.; Pham, K. and Miksovska, J. Modulation of the Voltage-gated Potassium Channel (Kv4.3) and the Auxiliary Protein (KChIP3) Interactions by the Current Activator NS5806. *J. Biol. Chem*. **2014**, *289*, 32201-32213.

17. Pham, K. and Miksovska, J. Molecular insight of DREAM and presenilin 1 C-terminal fragment interactions. *FEBS Lett*. **2016,** *590*, 1114-1122.

18. Azam, S. and Miksovska, J. Pb^{2+} Binds to Downstream Regulatory Element Antagonist Modulator (DREAM) and Modulates Its Interactions with Binding Partners: A Link between Neuronal Calcium Sensors and Pb^{2+} Neurotoxicity. *ACS Chem. Neurosci*. ***2019,*** *10*, 1263-1272.

19. Azam, S; Louis, G. and Miksovska, J. Cadmium association with DREAM promotes DREAM interactions with intracellular partners in a similar manner to its physiological ligand, calcium. *Metallomics,* **2019**, *11*, 1115-1127.

20. Fisher, J. R.; Sharma, Y.; Luliano, S.; Piccioti, R. A.; Krylov, D.; Hurely, J.; Order, J. and Jeromin, A. Purification od Myristolated and Nonmyristolated Neuronal Calcium Sensor-1 Using Single-Step Hydrophobic Interaction Chromatography. *Protein Expression and Purification*, **2000**, *20*, 66-72.

21. Gross, M. D.; Gosnell, M.; Tsarbopoulos, A. and Hunziker, W. A Functional and Degenerate Pair of EF Hands Contains the Very High Affinity Calcium-binding Site of Calbindin-D$_{28k}$, *The Journal of Biological Chemistry*, **1993**, *268*, 20917-20922.

22. Gonzalez, W.G. and Miksovska, J. Application of ANS fluorescent probes to identify hydrophobic sites on the surface of DREAM. *Biochimica et Biophysica Acta*. **2014**, *1844*, 1472-1480.

23. Beccia, M. R.; Sauge-Merle, S.; Lemaire, D.; Brémond, N.; Pardoux, R.; Blangy, S.; Guilpaud, P. and Berthomieu, C. Thermodynamics of Calcium binding to Calmodulin N-terminal domain to evaluate site-specific affinity constants and cooperativity. *J. Biol. Inorg. Chem*. **2015**, *20*, 905-919.

24. Ogawa, Y. and Tanokura, M. Calcium Binding to Calmodulin: Effects of Ionic Strength, Mg^{2+}, pH and temperature. *J. Biochem*. **1984**, *95*, 19-28.

25. Valeyev, N. V.; Bates, D. G.; Heslop-Harrison, P.; Postlethwaite, I. and Kotov, N. V. Elucidating the mechanisms of cooperative calcium-calmodulin interaction: a structural systems biology approach. *BMC Systems Biology*, **2008**, *2*, 1-17.

Chapter 6: Conclusion

In this work, we studied the complexation of Ln^{3+} with several ligands and characterized the interaction and complexation mainly by spectroscopic and/or calorimetric measurements. We were also able in some cases to isolate the complexes and fully characterize them by elemental analysis and in one case by X-ray crystallography. First, in Chapter 1, we provided a review of prior literature examples of ligands that bind Ln^{3+} in comparison with other cations, anions, and biological macromolecules. In addition, the importance of studying Ln^{3+} coordination to Ca^{2+} binding EF-hand proteins was explained, as it can be used for fluorescent studies and further structural analysis of those proteins. The recuring common feature of these ligands is the presence of oxygen mainly in the form of C=O that can bind Ln^{3+}, as Ln^{3+} are considered hard Lewis acids. The presence of aromatic rings in many of those ligands is presumed to increase energy transfer; ultimately enhancing the luminescence of Ln^{3+}. In Chapter 2, we have provided a complete Ln^{3+} binding study of a fluorescent bis(quinoline) derivative of the dipicolinamide family of ligands that have been previously used for Ln^{3+}/An^{3+} separation, including the X-ray structure of the Nd^{3+} complex, which strongly corroborates our prior findings that Ln^{3+} complex 1:1 with these ligands when strongly coordinating nitrate counteranions are present. Specifically, the complexation of bis-quinoline dipicolinamide ligand: N^2,N^6-di(quinolin-8-yl)pyridine-2,6-dicarboxamide, (DQPDH$_2$), with Ln^{3+} was characterized using UV-Vis and fluorescence spectroscopy. We observed red-shift in UV-Vis spectra and fluorescence quenching of DQPDH$_2$ upon addition of Ln^{3+}. Solvent extraction followed by spectrophotometric determination of Ln^{3+}, showed substantial Ln^{3+} extraction. We also measured the FT-IR of Ln^{3+} complexes of DQPDH$_2$ and compared them with the

IR of DQPDH$_2$ and noticed that the C=O bond red shifted to lower wavenumbers in Ln^{3+} complexes which is indicative of Ln^{3+} coordination. The 1:1 Ln^{3+}:DQPDH$_2$ complexation stoichiometry was confirmed by elemental analysis of the isolated Ln^{3+}-DQPDH$_2$ complexes and the X-ray structure of the Nd^{3+}-DQPDH$_2$ complex which showed one DQPDH$_2$ molecule and a 10-coordinate Nd^{3+}. In Chapter 3, we discussed the Ln^{3+} binding properties of the ortho-nitrobenzyl cage, DM-nitrophen and measured binding affinities with Ln^{3+} to DM-nitrophen using ITC. The high binding affinity of Ln^{3+} to DM-nitrophen is consistent with prior results obtained with EDTA. We also analyzed the kinetics and thermodynamics of Tb^{3+} binding to DM-nitrophen using PAC which showed two phases of enthalpy and volume changes associated with the two-step photolysis of Tb^{3+}:DM-nitrophen. In Chapter 4, we studied the Ln^{3+} coordination of another ortho-nitrobenzyl cage: Pyridine-2-carboxylic acid {1-(2-nitro-phenyl)-2-[(pyridine-2-ylmethyl)-carbamoyl]-ethyl}-amide (H$_2$cage) using UV-Vis spectroscopy. In addition, we studied the extraction of Ln^{3+} by H$_2$cage from alkaline aqueous phases and noticed that the ligand was able to extract Ln^{3+} very strongly. In Chapter 5, we characterized Ln^{3+}:DREAM interaction using fluorescence and lifetime measurements. Higher affinity of Ln^{3+} to DREAM was observed compared to the affinity of Ca^{2+} to DREAM by observing an increase in the emission of 1,8-ANS:DREAM and Trp quenching upon Ln^{3+} addition. Increase in the emission of Eu^{3+} in the presence of DREAM and CaM also confirms the binding of Ln^{3+} and possible energy transfer from nearby aromatic residues to central Ln^{3+}. Increase in the fluorescence decay lifetime of Ln^{3+}:protein complexes was observed while a decrease in the presence of EDTA indicates that Ln^{3+} has more affinity to EDTA.

Overall, our study of Ln^{3+} complexation with organic ligands and biological macromolecules paves the way for future applications in industrial and environmental separations of f-elements, as well as biological studies.

CURRICULUM VITAE

SETAREH SAKHDARI

EDUCATION

2004-2008   B.A., Chemistry
                     Payam Noor University
                     Mashhad, Iran

2010-2013   M.S., Dietetics and Nutrition
                     Florida International University
                     Miami, Florida

2015-2021   Doctoral Candidate, Chemistry
                     Florida International University
                     Miami, Florida

2016-2021   NRC-HQ-84-14-G-0040 and
                      NRC-HQ-84-15-G-0038/ 0038B

PRESENTATIONS

Sakhdari, S., and Miksovska, J. (2017). *Determining the Thermodynamic and Kinetic Parameters of Photodissociation of DM-nitrophen-Tb^{3+} Complex*. Poster presentation at Florida Annual Meeting & Expo (FAME), Tampa, Florida.

Sakhdari, S., Chakraborty, I., Miksovska, J., and Kavallieratos, K. (2018). *Caging lanthanides with photolyzable ligands: A spectroscopic study of interaction of the nitrophenyl diamide H$_2$-cage and DM-nitrophen with Tb(III)*. Poster presentation at Florida Inorganic and Material Symposium (FIMS), Gainesville, Florida.

Sakhdari, S., Chakraborty, I., Miksovska, J., and Kavallieratos, K. (2019). *Ortho-nitrobenzyl photolyzable ligands as cages for Tb(III) and other lanthanides*. Oral presentation at American Chemical Society National Meeting & Expo. Orlando, Florida.